Fall 12-2009

SATELLITE-BASED ESTIMATION OF CHLOROPHYLL-a CONCENTRATION IN TURBID PRODUCTIVE WATERS

Wesley Moses
University of Nebraska at Lincoln, wmoses.unl@gmail.com

SATELLITE-BASED ESTIMATION OF CHLOROPHYLL-*a* CONCENTRATION IN TURBID PRODUCTIVE WATERS

by

Wesley Jeremiah Moses

A DISSERTATION

Presented to the Faculty of

The Graduate College at the University of Nebraska

In Partial Fulfillment of Requirements

For the Degree of Doctor of Philosophy

Major: Natural Resource Sciences

Under the Supervision of Professor Anatoly A. Gitelson

Lincoln, Nebraska

December 2009

SATELLITE-BASED ESTIMATION OF CHLOROPHYLL-*a* CONCENTRATION IN TURBID PRODUCTIVE WATERS

Wesley Jeremiah Moses, Ph.D.

University of Nebraska, 2009

Advisor: Anatoly A. Gitelson

Inland, coastal, and estuarine waters, which are often turbid and biologically productive, play a crucial role in maintaining global bio-diversity and are of immense value to aquatic life as well as human-beings. Concentration of chlorophyll-*a* (chl-*a*) is a key indicator of the trophic status of these waters, which should be regularly monitored to ensure that their ecological balance is not disturbed. Remote sensing is a powerful tool for this.

Due to the optical complexity of turbid productive waters, standard algorithms that use blue and green reflectances are unreliable for estimating chl-*a* concentration. Algorithms based on red and near-infrared (NIR) reflectances are preferable. Three-band and two-band NIR-red models based on the spectral channels of MODIS and MERIS satellites have been tested for numerous datasets collected with field spectrometers from inland, coastal, and estuarine waters. The NIR-red models, especially the two-band model with MERIS wavebands, gave consistently highly accurate estimates of chl-*a* concentration in waters from different geographic locations with widely varying biophysical characteristics, without the need to re-parameterize the algorithms for each different water body. The MODIS NIR-red model can be used to estimate moderate-to-high chl-*a* concentrations.

The NIR-red models were applied to airborne AISA data acquired over several lakes in Nebraska on different days with non-uniform atmospheric conditions. Without atmospheric correction, the NIR-red models showed a close correlation with chl-*a* concentration for each image. With an effective relative correction for the non-uniform atmospheric effects on the multi-temporal images, the NIR-red models were shown to have a close correlation with chl-*a* concentration, with uniform slope and offset, for the whole dataset.

The models were also applied to MODIS and MERIS images. Reliable results were obtained from the MERIS NIR-red models. Calibrated MERIS NIR-red algorithms were validated using data from the Taganrog Bay and Azov Sea (Russia) and lakes in Nebraska. The calibrated NIR-red algorithms have the potential for universal application to estimate chl-*a* concentration from satellite data routinely acquired over turbid and productive waters from around the globe.

Dedicated with love and affection to

my beautiful wife,

Barbara Joy Moses,

and our dear baby,

whose arrival we eagerly anticipate.

ACKNOWLEDGMENTS

This research was made possible through help and collaborative effort from various individuals. Financial support came through two grants from the National Aeronautics and Space Administration (NASA), namely, NNG06GA92G and NNG06GG17G, and a grant from the U.S. Environmental Protection Agency (EPA), R-828634501.

I express my deep gratitude to my faculty advisor and Chairman of my Supervisory Committee, Prof. Anatoly A. Gitelson. I enjoyed debating and discussing the various aspects of this research with Dr. Gitelson. The research tips and the diligent guidance I received from him was hugely responsible for the successful completion of this research. It was a privilege for me to work with him. I also acknowledge the valuable contributions from the other members of my Supervisory Committee, namely, Prof. Donald C. Rundquist, Prof. Vitaly A. Zlotnik, and Prof. Kyle D. Hoagland. Prof. William D. Philpot from Cornell University was a courtesy member of the committee, and was always very prompt in responding to questions I had concerning my research.

Field data collection was a huge component of this research. Dr. Giorgio Dall'Olmo, who is currently at the Oregon State University and was in the final year of his doctorate program when I started my studies here, introduced me to the data collection techniques followed at CALMIT (Center for Advanced Land Management Information Technology, University of Nebraska-Lincoln). I enjoyed my discussions with him and he has been an inspiration to me in my research. I thank my fellow students, Daniela Gurlin and Yi Peng, for their contributions in data collection. Ms. Gurlin did the laborious task of filtering the water samples and estimating the constituent

concentrations. I am very thankful to her for providing me the *in situ* data. Tadd Barrow was very generous in sparing his time and energy and driving us on the boat whenever we went out to collect data. I enjoyed my conversations with him, which spanned topics such as politics, sports, and life in general. Bryan Leavitt was instrumental in ensuring that all equipments were tested and fully functional prior to setting out to the lakes. He was always very swift in providing technical support as needed. I am also thankful to Dr. Sergey Berdnikov and the research team at the Southern Scientific Center of the Russian Academy of Sciences, Rostov-on-Don, Russia, and the research team at the Institute for Environmental Quality, Kiev, Ukraine, for the *in situ* data they provided. I enjoyed working with Dr. Yosef Yacobi on the Sea of Galilee in Israel. I thank him for giving me the *in situ* data from the Sea of Galilee (Lake Kinneret).

Rick Perk gave me the airborne hyperspectral images in processed form. The satellite images were provided free of charge by NASA and the European Space Agency.

I am also very thankful to the other students at CALMIT who helped keep an atmosphere that was conducive to my studies. The comments from Anthony Nguy-Robertson significantly helped me in presenting my defense.

Aside from the aforementioned technical support, the emotional and spiritual support that I received from my family and friends were critical to the successful completion of this research.

Finally, my heart-felt gratitude and thanks go to my wonderful wife, whose love, prayers, and unmatched dedication encouraged me in ways that cannot be measured.

TABLE OF CONTENTS

INDEX OF FIGURES

INDEX OF TABLES

Chapter 1. Introduction

Researchers in the last two decades have been, with varying degrees of success, attempting to use remotely sensed data to study the inland, estuarine, and coastal water ecosystems. The objective of almost all of these studies has been to explore the possibilities of using remote sensing as a tool to assess the water quality in these ecosystems by detecting and monitoring the density and the condition of algae in the water bodies. This research is an attempt to develop satellite-based spectral algorithms to estimate algal densities in turbid and biologically productive inland, estuarine, and coastal waters.

1.1 The Need for Monitoring Algal Biomass

Algae are microscopic phytoplanktonic organisms that photosynthesize and thus form the base of aquatic food chains. Inasmuch as scarcity of free-floating algae (also called phytoplankton) can damage an ecosystem, over-abundance can also cause damages of equal proportions to the ecosystem. Over-abundance of phytoplankton and their subsequent decomposition affect the aquatic biota in a number of different ways, such as, blocking the sunlight from reaching the lower layers of water and thus depriving the under-water aquatic life of the much needed solar radiation, causing a severe depletion of dissolved oxygen in the waters, and producing toxins that fatally affect aquatic life and cause several diseases such as respiratory and skin disorders in human beings (Carmichael 1997). Inland, estuarine, and coastal water bodies, which are mostly turbid and productive, are home to a wide variety of flora and fauna that are crucial to not only maintaining global biodiversity but also providing the biotic resources that are essential

for human sustenance (Revenga and Kura 2003). Apart from being a pool of biodiversity, inland, estuarine, and coastal waters also serve as valuable resources for tourism, transportation, energy supply, and recreation. Specific instances of damage caused by harmful algal blooms to humans and the flora and fauna of an ecosystem have been very well documented in the literature, and it goes without saying that the need for prediction, early detection, and quantification of these algal blooms is of paramount importance.

Even though it is possible to monitor aquatic ecosystems through laboratory analysis of water samples collected from water bodies, it is extremely tedious and virtually impossible to do so on a frequent basis in a large ecosystem. The multi-temporal coverage and the synoptic view offered by remotely sensed data make remote sensing a suitable tool for this purpose (Gitelson et al. 2000).

1.2. Remote Sensing as a Tool for Real-time Algal Monitoring

Remote sensing was initially targeted by water resource scientists as a tool to detect algal blooms. With proven success in the realm of detection abetted by the improved spatial and spectral resolutions offered by the sensors and enhanced understanding of the bio-physical properties of water bodies, scientists have been pushing the technology to use it as a tool to obtain a quantitative measure of water quality by estimating the concentrations of different algal pigments that can be used as indicators of the bio-physical condition of water bodies. Whereas accurate detection of algal biomass has been proven achievable with not much difficulty, estimation of pigment concentrations has been more challenging.

Chlorophyll-*a* (chl-*a*) is a green pigment found in phytoplankton. The concentration of chl-*a* in water is a key indicator of phytoplankton biomass (Schalles et al. 1998; Honeywill et al. 2002).

Estimation of chl-*a* concentration by remote sensing is based on the effect of chl-*a* on the optical properties of water (which define the way water reacts to incident light), and is done by direct or indirect measurement of these optical properties. The optical properties are classified as Inherent Optical Properties (IOPs) and Apparent Optical Properties (AOPs). The IOPs depend strictly on the characteristics of the water medium alone whereas the AOPs depend on the geometry of the light field interacting with the water medium also. Refractive index, absorption coefficient, and scattering coefficient are some of the examples of IOPs; the radiance reflectance and the diffuse attenuation coefficient are examples of AOPs. Ideally it would be best to estimate chl-*a* concentration from direct measurements of the IOPs. However, this requires sophisticated instrumentation and meticulous analysis, making it virtually impossible to make regular routine measurements of the IOPs on a frequent basis. Thus the directly measured data of IOPs are difficult to obtain and hence scarcely available, which lends to the use of AOPs instead, specifically, the radiance reflectance.

The radiance reflectance, or remote sensing reflectance (R_{rs}), is defined as the ratio of the upwelling radiance (L_u) reflected from a body to the downwelling irradiance (E_d) incident on it.

$$R_{rs} = \frac{L_u}{E_d}$$

Chl-*a* is a photoactive pigment that causes distinct changes in the color of water by absorbing and scattering at specific wavelengths the light incident on water. These spectral features are evident in the reflectance spectrum at specific wavelengths and can be related to the concentration of chl-*a*. The ease of this procedure depends on the optical characteristics of the water body.

In deep ocean waters, phytoplankton is usually the predominant constituent and the concentrations of other constituents co-vary with chl-*a* concentration. Thus, the optical properties of these waters are dominated by phytoplankton and the observed spectral features in the reflected light can be directly related to chl-*a* concentration. Such waters are commonly referred to as Case I waters (Morel and Prieur 1977). Chl-*a* is primarily responsible for the strong absorption in the blue region and the peak reflectance in the green region of the reflectance spectrum from Case I waters. For these waters, spectral algorithms that use reflectances in the blue and green regions can be used to accurately estimate chl-*a* concentration (Gordon and Morel 1983; Gordon et al. 1988; O'Reilly et al. 1998; O'Reilly et al. 2000).

In most inland, estuarine, and coastal waters, constituents such as inorganic suspended solids and dissolved organic matter occur in abundance and their concentrations do not co-vary with chl-*a* concentration. Thus phytoplankton does not solely dominate the optical properties of such turbid productive waters, which are commonly referred to as Case II waters (Morel and Prieur 1977). Due to the optical complexity of Case II waters, specifically, the overlapping and uncorrelated absorptions by non-algal particles and dissolved organic matter in the blue region of the spectrum, algorithms that rely on blue-green ratios cannot be reliably used to estimate chl-*a*

concentration (Carder et al. 2004; Darecki and Stramski 2004; Dall'Olmo et al. 2005). When the chl-*a* concentration is considerably high, as it is in turbid productive waters, there is a prominent valley in the red region of reflectance spectrum caused due to strong absorption by chl-*a*. There is also a reflectance peak in the near-infrared (NIR) region around 700 nm (Vasilkov and Kopelevich 1982; Gitelson and Kondratyev 1991; Gitelson 1992; Han et al. 1994) caused by the combination of decreasing absorption by chl-*a* and increasing absorption by water. Since the absorption by non-algal particles and dissolved organic matter is significantly lower in the red and NIR regions than in the blue and green regions (Dekker 1993; Ruddick et al. 2001; Dall'Olmo et al. 2005), spectral algorithms that are based on reflectances in the red and NIR regions are preferable for estimating chl-*a* concentration in turbid productive waters (Gitelson 1992; Han and Rundquist 1997; Gons 1999; Gower et al. 1999; Dall'Olmo and Gitelson 2005)

In addition to the challenge of developing spectral algorithms that can reliably isolate chl-*a* induced spectral features from recorded reflectances and accurately relate those features to chl-*a* concentration, the problem of estimating chl-*a* concentration through remote sensing has another challenge in the form of atmospheric interference on the radiance signal recorded by the sensor.

Light has to pass through the Earth's atmosphere twice (sun-to-surface [sensor-to-surface for active sensors] and surface-to-sensor) before it is recorded by the remote sensor and is thus inevitably subject to atmospheric interference in the form of absorption and scattering of light by atmospheric gases and particles. Due to high absorption by water, on average, the water-leaving radiance is only about 10% or less of the total radiance recorded by the sensor (Siegel et al. 2000; Brivio et al. 2001). Thus it is

imperative that the atmospheric effects on remotely sensed data be first removed before any meaningful spectral analysis can be done for quantitatively estimating biophysical parameters in water. The process of removing atmospheric effects on the recorded radiance and retrieving the surface reflectance is called atmospheric correction. The low magnitude of water-leaving radiance makes atmospheric correction very difficult.

Absorption by the principal and trace atmospheric gases is accounted for by using well established databases of their spectral properties. Scattering by molecules is treated using the Rayleigh theory of scattering. Thus atmospheric effects due to gaseous absorption and molecular scattering and their seasonal and latitudinal variations can be adequately accounted for using look-up tables with computed values for different geographic locations and illumination conditions (Gordon et al. 1983; Gordon and Wang 1994). However, scattering by aerosol particles is difficult to correct for. This requires a determination of the variable aerosol optical depth, which is then used to determine the concentration of aerosol, its type, and its particle size distribution.

Original atmospheric correction procedures for ocean color data assumed zero water-leaving radiance at the NIR wavelengths. The at-sensor radiance at the NIR wavelengths, after being corrected for gaseous absorption and molecular scattering, were assumed to have been entirely due to atmospheric aerosol particulate scattering and were used to calculate the aerosol parameters (Gordon et al. 1983; Andre and Morel 1991; Gordon and Wang 1994). The assumption of zero water-leaving radiance in the NIR region (commonly referred to as black-pixel assumption), though valid for clear open ocean waters, is not valid for turbid waters due to scattering by suspended particles in the water, which results in appreciable water-leaving radiance in the NIR region (Moore

1980; Stumpf and Tyler 1988; Stumpf and Pennock 1989; Han and Rundquist 1994; Han and Rundquist 1996; Hu et al. 2000; Ruddick et al. 2000; Siegel et al. 2000; Stumpf et al. 2003). This results in over-estimation of the aerosol contribution and subsequent over-correction of the radiances, resulting in invalid and often negative reflectances throughout the spectrum, especially at the shorter wavelengths. Thus the accurate characterization of aerosol scattering is the most challenging aspect of atmospherically correcting remotely sensed data from turbid waters.

Researchers have tried various methods to account for the non-zero water-leaving radiance from turbid waters. Some methods use assumptions of empirically pre-defined relationships between the water-leaving radiances at specific wavelengths and attribute observed deviations from the relationships to atmospheric contribution, which is factored out iteratively (Smith 1981; Mueller 1984; Gould and Arnone 1994). The main problem with this approach is that the empirical relationships which are often based on regional data may not be applicable to waters from different geographic locations, with different biophysical and optical characteristics. Hu et al. (2000) used neighboring non-turbid water pixels to retrieve aerosol properties and extended them to turbid water pixels. This approach presumes the presence of clear water pixels in the image and spatial homogeneity of the aerosol type over the area considered, both of which may not be valid in many circumstances. Several approaches that combine the basic aerosol retrieval procedure in Gordon and Wang's (1994) atmospheric correction model (which was based on black-pixel assumption) with bio-optical reflectance models that explicitly account for non-zero water reflectance in the NIR region and calculate the water-leaving radiance iteratively or in a single step, have been shown to yield reliable water-leaving radiances

from MERIS (Medium Resolution Imaging Spectrometer) and MODIS (Moderate Resolution Imaging Spectroradiometer) data (Moore et al. 1999; Ruddick et al. 2000; Siegel et al. 2000; Stumpf et al. 2003; Wang and Shi 2005). Neural-networks that are trained using large datasets of observed radiances and radiances simulated by radiative transfer models for a wide range of atmospheric and illumination conditions for different geographic regions have been also used to derive water-leaving radiance from the at-sensor radiance (Doerffer and Schiller 2007; Doerffer and Schiller 2008). Atmospheric correction procedures of the latter two kinds have been used in this research.

Thus, successfully estimating chl-*a* concentration from satellite data has challenges on two fronts – (i) the spectral algorithm should be maximally sensitive to variations in chl-*a* concentrations and minimally sensitive to absorption and scattering of light by constituents other than chl-*a*, (ii) the radiance recorded by the sensor should be adequately corrected for atmospheric effects, resulting in reasonably valid reflectance values, so that the spectral algorithm can be applied reliably. The first challenge is addressed in Chapter 2, wherein NIR-red models designed for MODIS and MERIS sensors were tested using reflectance data collected through field spectrometers from several lakes in Nebraska, the Chesapeake Bay, and Lake Kinneret, Israel. These waters constitute a wide range of biophysical characteristics. The objective was to test whether the NIR-red models yield consistently high accuracies over a wide range of chl-*a* concentrations, especially in the low-to-moderate range. It was also tested whether the models have a steady correlation with chl-*a* concentration in spite of variations in the biophysical characteristics of the water body.

Chapters 3 and 4 deal with the second challenge. The problem of reliable atmospheric correction has not been dealt with in an absolute sense but in a relative sense in terms of their effects on the performance of the NIR-red models. Chapter 3 contains the results of applying the NIR-red models to aircraft data, which was done as an intermediate step before applying the models to satellite data. At a low-flying aircraft altitude of about 10,000 ft above ground, the sensor sees through a far less amount of the Earth's atmosphere than a space-borne satellite would see through. Moreover, the flexibility offered by aircraft image acquisition in terms of flight planning and the adjustability of spectral characteristics, as well as high spatial resolution, make aircraft data an useful and essential platform for testing the NIR-red spectral models before applying them to satellite data.

The first half of Chapter 4 illustrates the close correlations that the NIR-red models have with phytoplankton biophysical characteristics in general and chl-*a* concentration in particular, when the models were applied to MODIS and MERIS data. The second half of the chapter describes the development of NIR-red algorithms to estimate chl-*a* concentration from MERIS data, the validation of the algorithms, and the issues and challenges involved in developing such algorithms for universal application to satellite data routinely acquired over inland, estuarine, and coastal waters around the globe. The summary and intended future work are presented in Chapter 5.

Chapter 2. Accuracy Assessment of NIR-red Models with MODIS and MERIS Wavebands

The objective of this chapter was to test the accuracy of the NIR-red models (with wavebands that match the spectral channels of MODIS and MERIS sensors) in estimating a wide range of chl-*a* concentrations, using reflectance data collected with field spectrometers, with special attention given to low-to-moderate chl-*a* concentrations. The excellent results from the NIR-red models as reported in previous studies (Dall'Olmo and Gitelson 2005; Dall'Olmo et al. 2005; Gitelson et al. 2007; Gitelson et al. 2008) were largely due to the moderate-to-high chl-*a* concentrations in the respective datasets, while uncertainties still remained in the low-to-moderate range. In this chapter, particular focus has been given to the low-to-moderate chl-*a* concentrations, which are typical for inland, estuarine, and coastal waters. In addition, the ability of the NIR-red models to account for biophysical and bio-optical variability in water has also been analyzed.

Thus, the specific question addressed was whether the MODIS and MERIS NIR-red models can consistently explain variations in chl-*a* concentrations for waters with widely varying biophysical characteristics so as to enable the development of robust algorithms that can be universally applied to satellite data for estimating chl-*a* concentration in inland, estuarine, and coastal waters.

2.1. The MODIS and MERIS NIR-red Models

The MODIS and MERIS NIR-red models are based on the NIR-red model developed by Dall'Olmo and Gitelson (2005). The model is based on a fundamental

relationship between the remote sensing reflectance (R_{rs}) and the optical properties of water, given by Gordon's model (Gordon et al. 1975)

$$R_{rs} \propto \frac{b_b}{a + b_b},$$

where, a is the absorption coefficient, and b_b is the back-scattering coefficient.

The absorption coefficient a is the sum of the absorption coefficients of water (a_{w}), phytoplankton (a_{ph}), non-algal particles (a_{nap}), and colored dissolved organic matter (a_{CDOM}).

Using Gordon's model as the foundation, the NIR-red model was designed by choosing three optimal wavelengths such that the contributions due to absorption by constituents other than chl-*a* and the back-scattering by particular matter are kept to a negligible minimum and the model output is maximally sensitive to variations due to spectral contributions from chl-*a*. The three-band NIR-red model is of the form (Dall'Olmo and Gitelson 2005),

chl-*a* $\propto \left(R_{\lambda_1}^{-1} - R_{\lambda_2}^{-1}\right) \times R_{\lambda_3}$, where R_{λ_i} is the remote sensing reflectance at wavelength λ_i.

λ_1 is in the red region at around 670 nm where there is maximal absorption by chl-*a* and some absorption by other constituents. λ_2 is at a longer wavelength than λ_1, where absorption by chl-*a* is minimal and absorption by other constituents is about the same as at λ_1. Thus $R_{\lambda_1}^{-1}$ is a measure of the absorption due to chl-*a* and other constituents and $R_{\lambda_2}^{-1}$ is a measure of the absorption due to constituents other than chl-*a*. The back-scattering coefficient is considered spectrally uniform across the range of

wavelengths considered – λ_1 through λ_3 (Dall'Olmo and Gitelson 2005). The subtraction of $R_{\lambda_2}^{-1}$ from $R_{\lambda_1}^{-1}$ isolates the absorption by chl-*a* as shown below:

$$R_{\lambda_1}^{-1} - R_{\lambda_2}^{-1} \propto \left[\frac{a_{\mathrm{w}\lambda_1} + a_{\mathrm{ph}_{\lambda_1}} + a_{\mathrm{nap}_{\lambda_1}} + a_{\mathrm{CDOM}_{\lambda_1}} + b_b}{b_b} - \frac{a_{\mathrm{w}\lambda_2} + a_{\mathrm{ph}\lambda 2} + a_{\mathrm{nap}\lambda 2} + a_{\mathrm{CDOM}\lambda 2} + b_b}{b_b} \right]$$

$$\propto \frac{a_{\mathrm{ph}} + a_{w_{\lambda_1}} - a_{w_{\lambda_2}}}{b_b}$$

λ_3 is at a wavelength beyond λ_2, in the NIR region, where there is no absorption by any constituent and the absorption by water is much greater than the total back-scattering such that $a_{w_{\lambda_3}} >> b_b$ and $a \sim a_{w_{\lambda_3}}$.

$$\therefore R_{\lambda_3} \propto \frac{b_b}{a_{w_{\lambda_3}}}$$

Considering the fact that a_{w} is independent of the concentrations of the constituents in water and ignoring its dependence on the temperature of water (thus, a_{w} is constant at each wavelength), the equation for the spectral algorithm becomes,

$$\left(R_{\lambda_1}^{-1} - R_{\lambda_2}^{-1}\right) \times R_{\lambda_3} \propto a_{\mathrm{ph}}.$$

$a_{\mathrm{ph}} = a_{\mathrm{ph}}^{*} \times C_{\text{chl-}a}$, where a_{ph}^{*} is the specific absorption coefficient of phytoplankton, and $C_{\text{chl-}a}$ is the concentration of chl-*a*. Thus,

$$\left(R_{\lambda_1}^{-1} - R_{\lambda_2}^{-1}\right) \times R_{\lambda_3} \propto \text{ chl-}a \qquad (2.1)$$

For waters that do not have significant concentrations of non-algal particles and colored dissolved organic matter, the subtraction of $R_{\lambda_2}^{-1}$ in the model can be dropped (Dall'Olmo and Gitelson 2005), leading to a special case two-band NIR-red model (Stumpf and Tyler 1988), given by,

$$R_{\lambda_1}^{-1} \times R_{\lambda_3} \propto \text{chl-}a \tag{2.2}$$

MERIS has spectral bands centered at 665 nm (band 7), 681 nm (band 8), 708 nm (band 9), and 753 nm (band 10) in the red and NIR regions. MODIS has spectral bands centered at 667 nm (band 13), 678 nm (band 14) and 748 nm (band 15) in the red and NIR regions. The 681 nm MERIS band and 678 nm MODIS bands were not considered because of their proximity to chl-*a* fluorescence wavelength, which might affect the accuracy of chl-*a* estimation due to the variable quantum yield of fluorescence (Dall'Olmo and Gitelson 2006). Thus, for MERIS, λ_1, λ_2, and λ_3 were 665 nm, 708 nm, and 753 nm, respectively. For MODIS (with no spectral band available at λ_2), λ_1 and λ_3 were 667 nm and 748 nm, respectively.

Considering the spectral band locations for MERIS, another case of a two-band model was considered, which takes advantage of the reflectance peak around 700 nm, which is in the region of the MERIS λ_2 band. This peak is caused by the combination of diminishing absorption by chl-*a* and increasing absorption by water (Vasilkov and Kopelevich 1982; Gitelson 1992). This model is fundamentally different from the previously mentioned two-band model (equation (2.2)) and is of the form,

$$R_{\lambda_1}^{-1} \times R_{\lambda_2} \propto \text{chl-}a \tag{2.3}$$

Thus the NIR-red models used in this study were formulated as follows:

$$\text{Three-Band MERIS NIR-red Model: } \text{Chl-}a \propto \left(R_{665}^{-1} - R_{708}^{-1}\right) \times R_{753} \tag{2.4}$$

$$\text{Two-Band MERIS NIR-red Model: } \text{Chl-}a \propto \left(R_{665}^{-1} \times R_{708}\right) \tag{2.5}$$

$$\text{Two-Band MODIS NIR-red Model: } \text{Chl-}a \propto \left(R_{667}^{-1} \times R_{748}\right) \tag{2.6}$$

2.2. Field Measurements

In situ reflectance data were collected from repeated data collection campaigns at several lakes in Nebraska, viz., Fremont State Lakes 01, 03, 05, and 20, Lake Christensen, Copper Dollar Cove, Cedar Creek, and Lake Benak, in the summer of 2005, and Fremont State Lakes 01, 02, 03, 04, 05, 16, 17, 18, and 20 in the summer of 2008. The upwelling radiance and downwelling irradiance spectra were collected using two Ocean Optics® USB2000 radiometers deployed from a boat. The radiometers recorded radiances over the wavelength range of 349 nm – 1017 nm, at 0.3 nm sampling intervals, with a spectral resolution of 1.5 nm and a signal-to-noise ratio of 250:1.

Radiometer #1 was connected to a 25° field-of-view optical fiber that was taped to a measurement stick and pointed towards nadir to measure the upwelling radiance. The stick was held such that the tip of the optical fiber was just beneath the water surface and as far away from the boat as possible on the sun-lit side in order to avoid light rays reflected from the boat and the effects of the boat shadow. Windy and choppy conditions on the water bodies affected the ability to hold the measurement stick such that the tip of the optical fiber was just beneath the water surface. As a result, on several occasions, the tip of the optical fiber was actually a few centimeters below the surface instead of being 'just-below'. However, errors in estimated chl-*a* concentrations due to such unavoidable variations in the depth of the tip position were small (Gitelson et al. 2008).

Radiometer #2 was connected to an optical fiber that was equipped with an almost 180° field-of-view cosine collector that was mounted on a mast and held vertically up at the highest possible spot on the boat such that the cosine collector had a clear 180° field-of-view of the downwelling solar irradiance. The upwelling radiance and the

downwelling irradiance were recorded simultaneously. At each station, several sets of measurements were taken such that there were at least six virtually overlaying upwelling radiance spectra, the median of which was taken as the representative spectrum. The radiometers recorded the radiances and irradiances as digital counts. Measurements were also taken over a flat Spectralon® calibration panel with a known reflectance in order to account for the differing solar/sky illumination conditions and convert the digital counts to reflectance values.

In addition to radiance data, ancillary data such as the Secchi disk depth, turbidity, and water temperature were also taken. Water samples were collected at each station and kept in an ice-cooler in the boat during data collection. These samples were analyzed in the laboratory immediately after the crew returned from the field campaign.

2.3. Laboratory Measurements

Water samples collected at each station were filtered through Whatman GF/F glass filters. Chl-*a* was extracted in hot ethanol and its concentration was determined fluorometrically (Welschmeyer 1994). The concentration of total suspended solids (TSS) was measured by gravimetric analysis (Dall'Olmo and Gitelson 2005; Gitelson et al. 2008).

2.4. Application of the NIR-red models

The measured radiance data were converted to remote sensing reflectance, R_{rs}, as,

$$R_{rs} = \frac{L_u}{E_d}\frac{E_{cal}}{L_{cal}}\frac{R_{cal}}{\pi}\frac{t}{n^2}F_i, \qquad (2.7)$$

where, L_u is the upwelling radiance from the water, E_d is the downwelling solar irradiance, L_{cal} is the upwelling radiance from the calibration panel, E_{cal} is the downwelling solar irradiance at the time of calibration measurements, R_{cal} is the known reflectance of the calibration panel, t is the transmittance of water (0.98), n is the refractive index of water (1.33), and F_i is the immersion factor, which accounts for the difference between the in-air and in-water absolute response of the radiometer (Austin 1976; Mueller and Austin 1995; Zibordi 2006), and was calculated using the formula used in (Ohde and Siegel 2003). The *in situ* measured reflectance data were averaged to match the bandwidths (~ 10 nm) of the MERIS and MODIS spectral channels.

2.4.1. 2005 Nebraska Lakes Data

The dataset collected in 2005 showed significant variations in biophysical parameters of lakes, such as the concentrations of chl-*a* and TSS, the turbidity, and the Secchi disk depth (Table 2.1). Chl-*a* concentrations ranged from 1.2 mg m^{-3} to 202.8 mg m^{-3} and there was up to a sixteen-fold variation in TSS concentration. The concentrations of chl-*a* and TSS varied almost independent of each other (figure 2.1), confirming that the waters sampled were Case II waters (Morel and Prieur 1977). The remote sensing reflectance spectra were similar in shape and magnitude to those from typical turbid productive waters (Lee et al. 1994; Gitelson et al. 2000; Dall'Olmo and Gitelson 2005; Schalles 2006), with significant variations in the visible and near-infrared regions (figure 2.2). The reflectances were characterized by (i) low values in the blue region (400 – 500 nm) due to high absorption by chl-*a*, TSS, and CDOM, (ii) a local maximum in the green region (around 550 nm) due to decreased absorption by all constituents, (iii) a local minimum around 625 nm due to absorption by phycocyanin in lakes where phycocyanin

was present, (iv) a local minimum in the red region (around 670 nm) due to absorption by chl-*a*, (v) a local maximum in the region between 690 nm and 720 nm due to the combined effect of decreasing absorption by chl-*a* and increasing absorption by water, and (vi) low values in the NIR region beyond 750 nm due to high absorption by water. The coefficient of variation of reflectance was highest in the 700 – 800 nm region. In this region, reflectance is controlled mostly by scattering by particulate matter. The high magnitude of the coefficient of variation in the 700 – 800 nm region suggests a wide variation in the concentration of suspended particulate matter.

Parameter	**Min.**	**Median**	**Max.**	**Mean**	**Standard Deviation**	**Coefficient of Variation**	**Number of Samples**
Secchi Disk Depth (m)	0.23	0.94	3.71	1.08	0.74	0.7	81
Turbidity (Nephelometric Turbidity Units)	1.57	6.71	52.5	13.24	12.6	0.95	83
TSS (g m^{-3})	2	7.6	32.5	11.28	8.73	0.77	64
ISS (g m^{-3})	0	1.2	10.8	1.77	2.24	1.27	35
Chl-*a* (mg m^{-3})	1.2	15	202.8	41.15	50.11	1.22	83

Table 2. 1. Summary of the ancillary data for 2005.

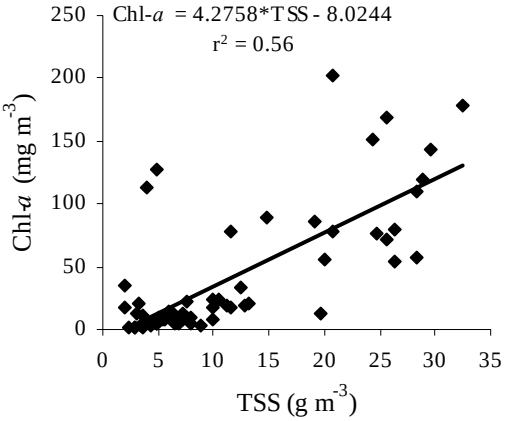

Figure 2. 1. Plot of TSS concentration versus chl-*a* concentration for waters sampled from Nebraska lakes in 2005.

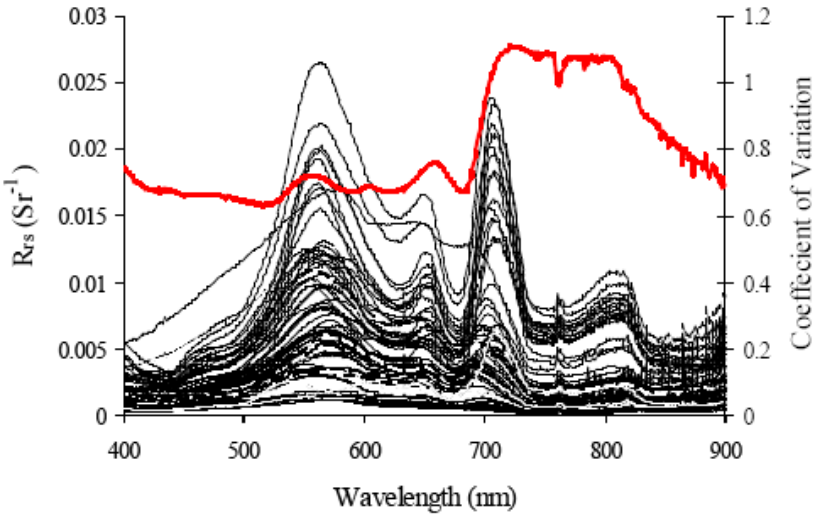

Figure 2. 2. Remote sensing reflectance (R_{rs}) spectra for waters sampled in 2005. The coefficient of variation of reflectance is plotted in red.

The three-band and two-band model values (equations (2.4) – (2.6)) were calculated for the reflectance data collected at 83 stations (figures 2.3(a) through 2.5). λ_1 (at 665 nm for the MERIS models (equations (2.4) and (2.5)); at 667 nm for the MODIS model (equation (2.6)) was chosen such that $R_{\lambda_1}^{-1}$ is a measure of absorption that is primarily due to chl-*a*. However, chl-*a* absorption was not the only factor that influenced $R_{\lambda_1}^{-1}$. Factors such as scattering due to suspended solids (figure 2.3(b)) and absorption due to non-algal particles and dissolved organic matter also contributed to $R_{\lambda_1}^{-1}$. Because of this, even though the absorption due to chl-*a* increased with increase in chl-*a* concentration, $R_{\lambda_1}^{-1}$ did not have a steady positive linear correlation with chl-*a* concentration. The relationship, in fact, had a negative slope (figure 2.3(a)). A positive correlation was seen for chl-*a* above 160 mg m^{-3}, where the absorption due to chl-*a* is so strong as to mask the contributions from the other factors. The reciprocal reflectance at

λ_2 (708 nm), R_{708}^{-1}, which is influenced by absorption due to non-algal particles and colored dissolved organic matter, and scattering by suspended solids, was related to the concentration of total suspended solids (figure 2.3(b)). The subtraction of R_{708}^{-1} from R_{665}^{-1} yielded a positive correlation with chl-*a* concentration (figure 2.3(c)). However, in addition to absorption by chl-*a*, the relationship was also strongly affected by backscattering by suspended solids. Multiplication by R_{753}, which accounts for scattering by suspended solids, resulted in a close linear relationship between the three-band model values and chl-*a* concentration, with a coefficient of determination (r^2) of 0.94.

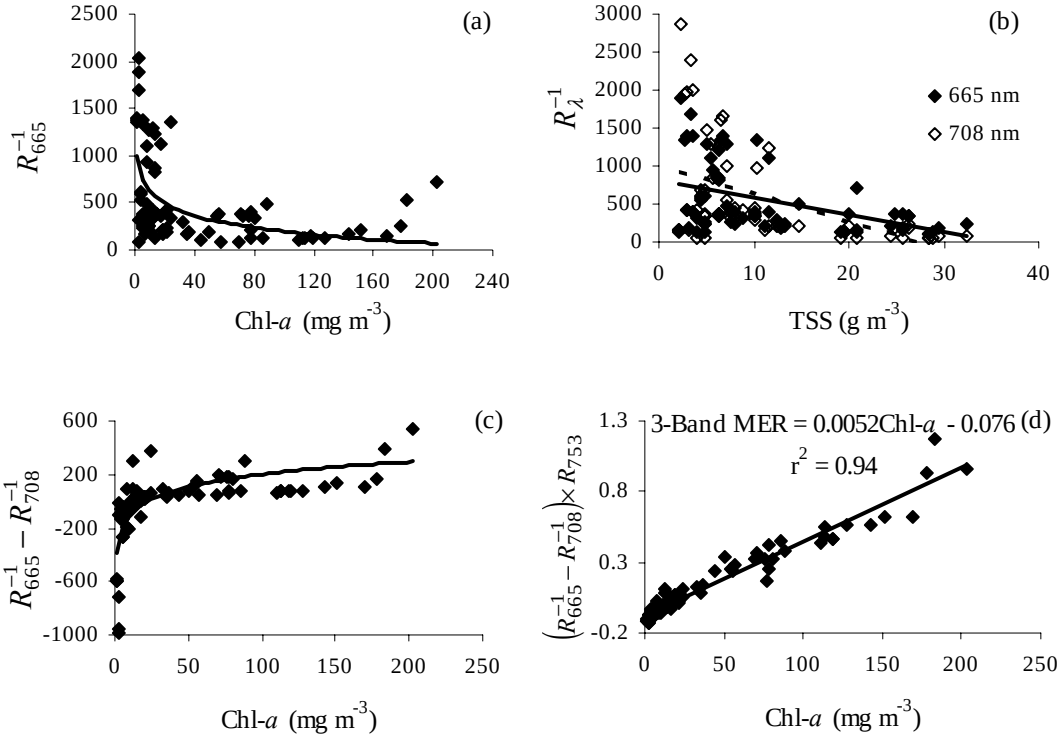

Figure 2. 3. Plots of (a) chl-*a* concentration versus the reciprocal reflectance at 665 nm, (b) TSS concentration versus the reciprocal reflectances at 665 nm and 708 nm, (c) chl-*a* concentration versus $\left(R_{665}^{-1} - R_{708}^{-1}\right)$, (d) chl-*a* concentration versus the three-band MERIS NIR-red model, for the 2005 Nebraska lakes dataset.

The reflectance in the MERIS 708 nm band is highly affected by the reflectance peak around 700 nm (Vasilkov and Kopelevich 1982). The magnitude of this peak

depends on the concentrations of chl-*a* and suspended solids and its position shifts toward longer wavelength as chl-*a* concentration increases (Gitelson 1992). The two-band MERIS NIR-red model, $R_{665}^{-1} \times R_{708}$ took advantage of the effect of this reflectance peak and the reflectance minimum around 665 nm due to maximal absorption by chl-*a*. The model values had a close linear relationship with chl-*a* concentration (figure 2.4), with a coefficient of determination of 0.93.

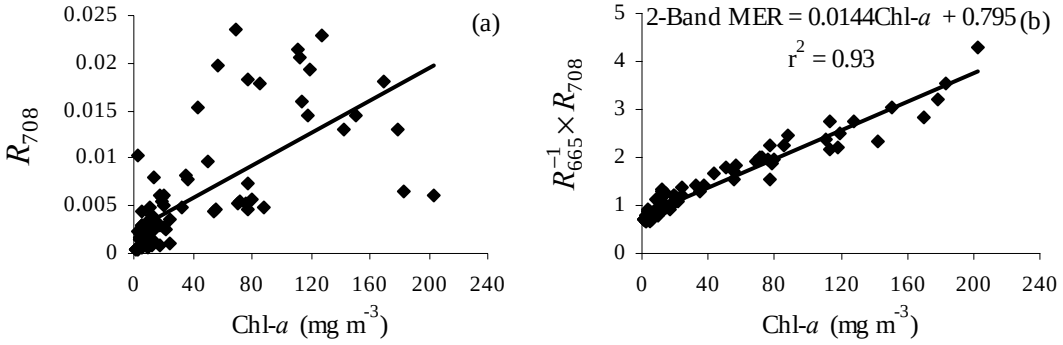

Figure 2. 4. Plots of (a) chl-*a* concentration versus reflectance in the MERIS 708 nm band, and (b) chl-*a* concentration versus the two-band MERIS NIR-red model, for the 2005 Nebraska lakes dataset.

The two-band MODIS NIR-red model does not involve the subtraction of $R_{\lambda_2}^{-1}$, which accounts for the absorption due to constituents other than phytoplankton (Dall'Olmo and Gitelson 2005; Gitelson et al. 2008). Nevertheless, for the whole range of chl-*a* concentrations considered (1.2 mg m^{-3} to 202.8 mg m^{-3}), the two-band MODIS NIR-red model had a close linear correlation with chl-*a* concentration (figure 2.5), with a coefficient of determination of 0.92, which is comparable to that for the three-band MERIS NIR-red model and the two-band MERIS NIR-red model. The subtraction of $R_{\lambda_2}^{-1}$ became critical for low-to-moderate chl-*a* concentrations. Compared to the three-band and the two-band MERIS NIR-red models, the two-band MODIS NIR-red model was

virtually insensitive to chl-*a* concentrations less than 25 mg m^{-3} (figure 2.6) and proved unreliable for estimating chl-*a* concentration below 25 mg m^{-3}. This is because the reflectance at 748 nm (λ_3 for the two-band MODIS NIR-red model) is mostly influenced only by scattering due to suspended particles and is not affected by changes in chl-*a* concentration. Moreover, the reflectance in MODIS λ_1 waveband is affected by contribution from other constituents and is not closely related to chl-*a* concentration (figure 2.3(a)). Thus the numerator and the denominator in the two-band MODIS NIR-red model are strongly affected by factors other than chl-*a* absorption, which is especially the case at low-to-moderate chl-*a* concentration.

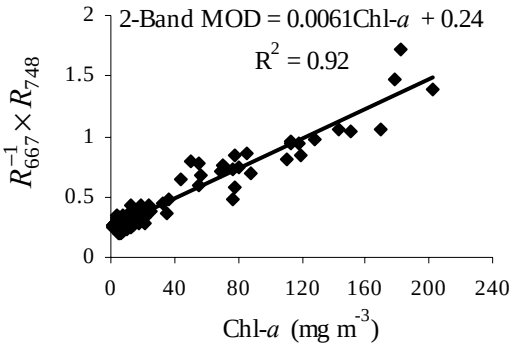

Figure 2. 5. Plot of chl-*a* concentration versus two-band MODIS NIR-red model for the 2005 dataset.

2.4.2. 2008 Nebraska Lakes Data

Similar to the 2005 dataset, the 2008 dataset also had significant variations in biophysical parameters such as the concentrations of chl-*a* and TSS, the turbidity, and the Secchi disk depth (Table 2.2). The chl-*a* concentration ranged from 2.07 mg m^{-3} to 103.4 mg m^{-3}, whereas TSS concentration varied from 1.19 g m^{-3} to 15 g m^{-3}. The high concentrations of chl-*a* and TSS and the weak correlation between them (figure 2.7) confirmed that the waters sampled were turbid and productive Case II waters. Figure 2.8

shows the reflectance spectra for the waters sampled. As with the 2005 Nebraska lakes data, there were significant variations in reflectance in the visible and NIR regions. There were fewer lakes with significant concentrations of phycocyanin.

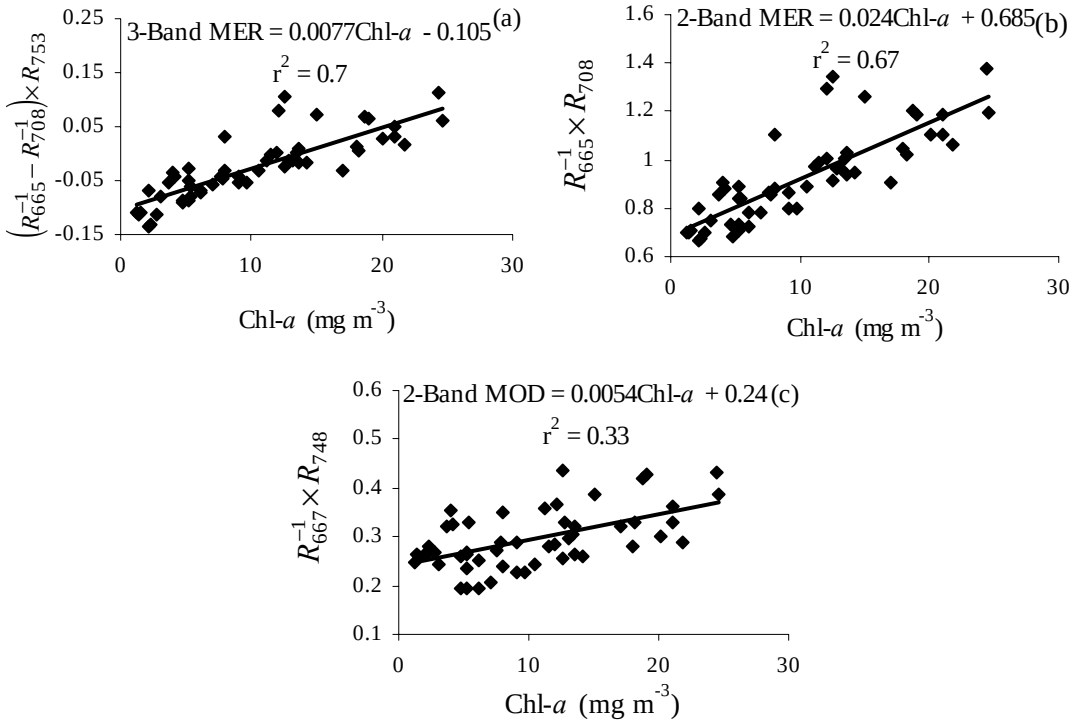

Figure 2. 6. Plots of chl-*a* concentration versus (a) three-band MERIS NIR-red model, (b) two-band MERIS NIR-red model, and (c) two-band MODIS NIR-red model, for the 2005 dataset.

Parameter	**Min.**	**Median**	**Max.**	**Mean**	**Standard Deviation**	**Coefficient of Variation**	**Number of Samples**
Secchi Disk Depth (cm)	0.51	0.96	4.2	1.21	0.71	0.59	85
Turbidity (Nephelometric Turbidity Units)	1.51	6.95	19.2	7.7	4.45	0.58	85
TSS (g m^{-3})	1.19	6.8	15	7.22	3.22	0.45	85
ISS (g m^{-3})	0.15	0.80	3.5	0.98	0.64	0.66	84
Chl-*a* (mg m^{-3})	2.07	23.07	103.4	26.28	18.13	0.69	85

Table 2. 2. Summary of the ancillary data for 2008

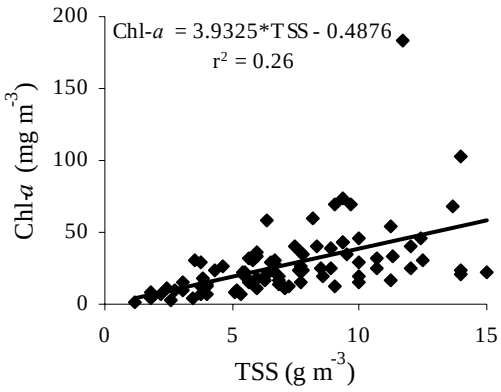

Figure 2. 7. Plot of TSS concentration versus chl-*a* concentration for waters sampled from Nebraska lakes in 2008.

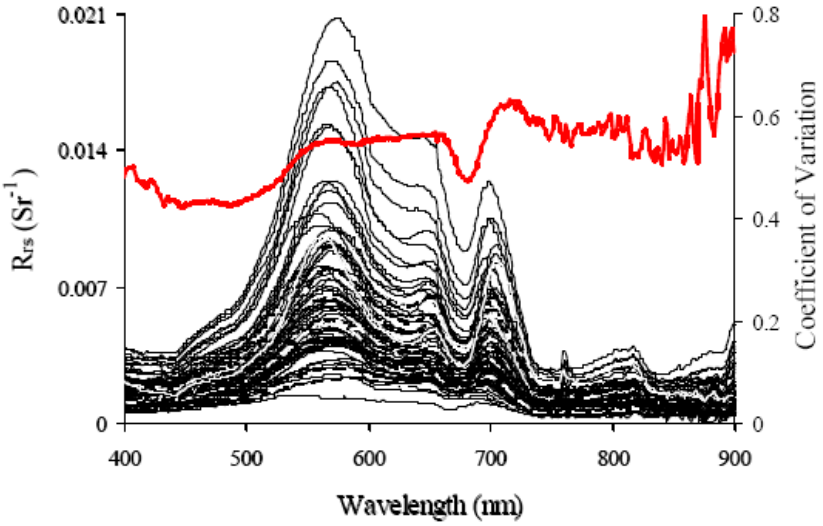

Figure 2. 8. Remote sensing reflectance (R_{rs}) spectra for waters sampled in 2008. The coefficient of variation of reflectance is plotted in red.

Figures 2.9(a) through 2.9(d) show the step-by-step plots for each term in the three-band MERIS NIR-red model for the 2008 data. As it was with the 2005 data, the reciprocal reflectance at 665 nm was affected by absorption by constituents other than chl-*a* and scattering by suspended solids (figure 2.9(b) in addition to absorption by chl-*a*. This resulted in a negative correlation between R_{665}^{-1} and chl-*a* concentration, which was more pronounced at low-to-moderate chl-*a* concentrations (figure 2.9(a)).

The reciprocal reflectance at 708 nm, R_{708}^{-1}, had a strong correlation with TSS concentration (figure 2.9(d)). The subtraction, $R_{665}^{-1} - R_{708}^{-1}$, resulted in the removal of the effects due to absorption by constituents other than chl-*a*, leading to a better correlation with chl-*a* concentration (figure 2.9(c)) than R_{665}^{-1} had (figure 2.9(a). But the relationship was still affected by backscattering by suspended solids. This was rectified by multiplying $(R_{665}^{-1} - R_{708}^{-1})$ with R_{753}, leading to a very close relationship with chl-*a* concentration, with a coefficient of determination of 0.94 (figure 2.9(d)).

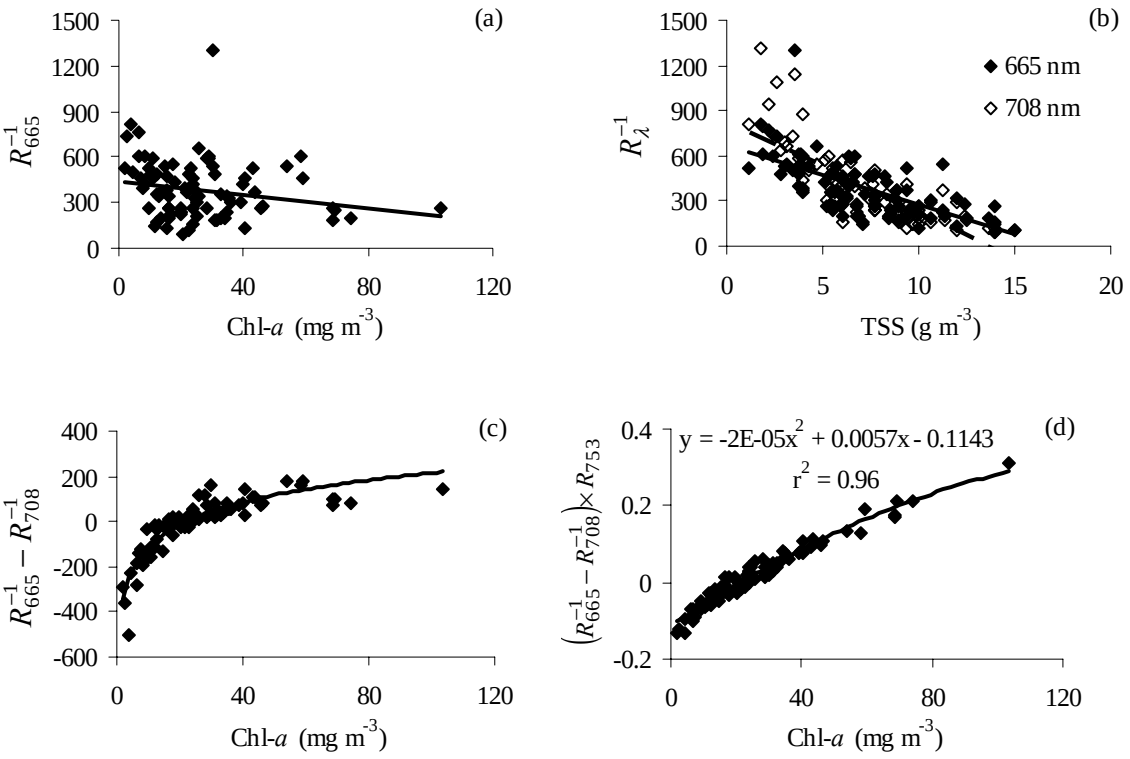

Figure 2. 9. Plots of (a) chl-*a* concentration versus the reciprocal reflectance at 665 nm, (b) TSS concentration versus the reciprocal reflectances at 665 nm and 708 nm, (c) chl-*a* concentration versus $\left(R_{665}^{-1} - R_{708}^{-1}\right)$, (d) chl-*a* concentration versus the three-band MERIS NIR-red model, for the 2008 dataset.

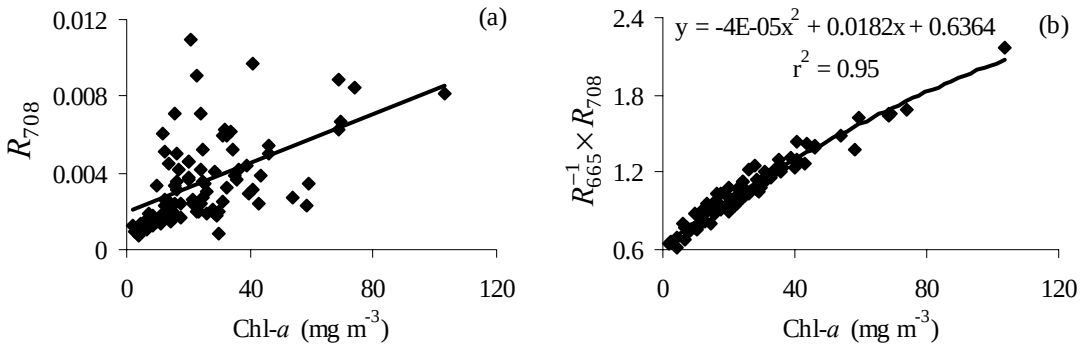

Figure 2. 10. Plots of (a) chl-*a* concentration versus reflectance at 708 nm, and (b) chl-*a* concentration versus the two-band MERIS NIR-red model, for the 2008 dataset.

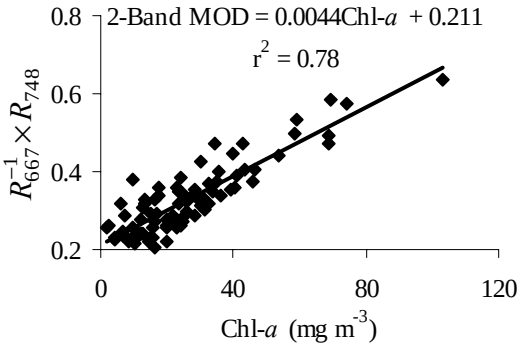

Figure 2. 11. Plot of chl-*a* concentration versus two-band MODIS NIR-red model for the 2008 dataset.

The two-band MERIS NIR-red model and the two-band MODIS NIR-red model also had close linear relationships with chl-*a* concentration, with coefficients of determination 0.95 and 0.78, respectively (figures 2.10 and 2.11). However, as it was for the 2005 dataset, the two-band MODIS NIR-red model was less sensitive to low-to-moderate chl-*a* concentrations (< 25 mg m^{-3}) than the three-band and the two-band MERIS NIR-red models were (figure 2.12), as evidenced by the looser fit of data points around the regression line, re-establishing the fact that the two-band MODIS NIR-red model is not reliable for estimating low-to-moderate chl-*a* concentrations. Due to the low

accuracy and unreliability of the two-band MODIS NIR-red model at low-to-moderate chl-*a* concentrations, no attempt was made to calibrate this model for potential use with satellite and aircraft data.

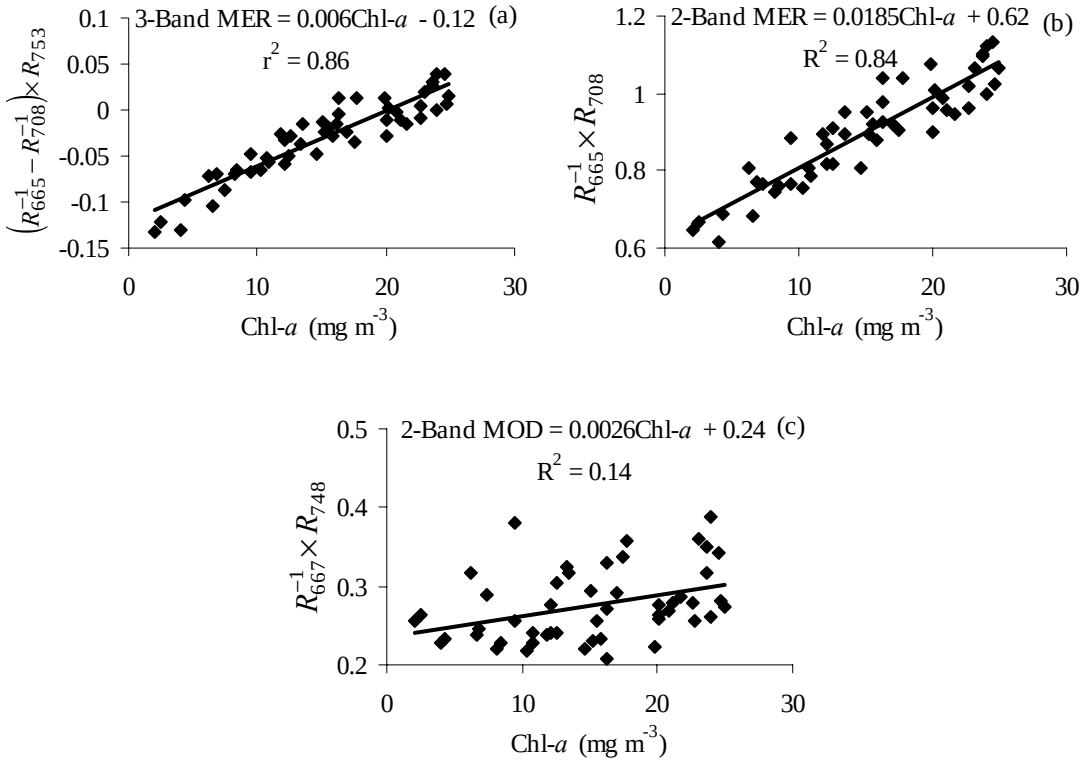

Figure 2. 12. Plots of chl-*a* concentration versus (a) three-band MERIS NIR-red model, (b) two-band MERIS NIR-red model, and (c) two-band MODIS NIR-red model, for the 2008 dataset.

2.5. Choosing the Best NIR-red Model

The three NIR-red models (equations (2.4) through (2.6)) were compared against each other in order to choose the most suitable model for application to aircraft and satellite data.

2.5.1. Comparison between the two-band MODIS and the two-band MERIS NIR-red models

The two-band MODIS NIR-red model and the two-band MERIS NIR-red model have virtually the same denominator (R_{667} and R_{665} respectively). The models differ in their numerator (R_{748} for the two-band MODIS NIR-red model and R_{708} for the two-band MERIS NIR-red model).

A fundamental assumption in the NIR-red models is the spectral independence of backscattering by suspended particles (Dall'Olmo and Gitelson 2005) throughout the wavelengths considered (λ_1 through λ_3). However, the absorption by water at 748 nm is much higher than that at 667 nm, and with the exponential decrease in particulate backscattering toward longer wavelengths, the reflectance at 748 nm had a very different relationship with inorganic suspended solids (ISS) concentration than did the reflectance at 667 nm (figure 2.13). For instance, for the 2008 Nebraska lakes data, the linear regression of R_{667} versus ISS concentration had a slope of 0.001 and an intercept of 0.0022 Sr^{-1}. The corresponding figures were 0.0003 and 0.0007 Sr^{-1} respectively for R_{748}, thus indicating that the effect of scattering by ISS on the recorded reflectance is significantly different at 748 nm than at 667 nm. Thus, in the two-band MODIS NIR-red model, the multiplication by R_{748} does not produce the desired outcome of removing the effects of scattering by suspended particles. This makes the two-band MODIS NIR-red model susceptible to random variations due to scattering by inorganic suspended particles, which is pronouncedly seen at low-to-moderate chl-*a* concentrations (figure 2.12).

Due to the proximity of the 665 nm and 708 nm bands, the effects of scattering by inorganic suspended solids were almost similar at these two wavebands. The slopes and offsets of the relationships between the reflectances at 665 nm and 708 nm and ISS concentration were very similar (figure 2.13). Thus, the ratio R_{708}/R_{665} essentially cancelled out the effect of scattering by ISS, thereby making the two-band MERIS NIR-red model maximally sensitive to variations in chl-*a* concentration and minimally sensitive to scattering by ISS.

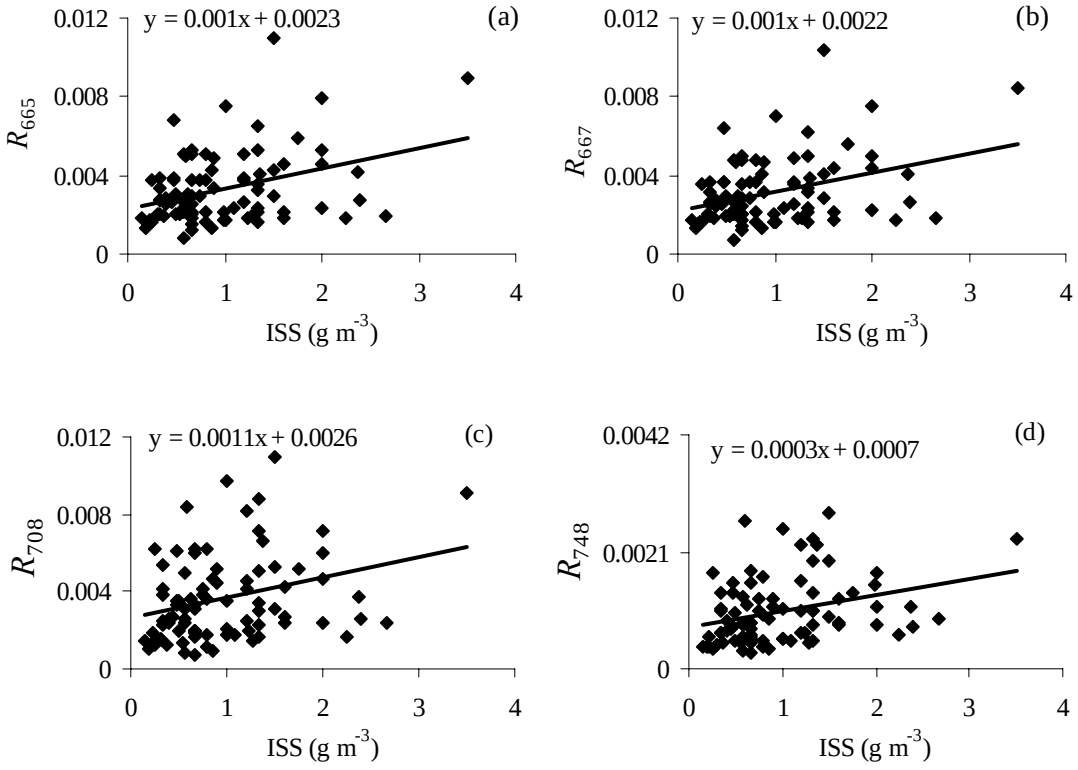

Figure 2. 13. Plots of ISS concentrations versus reflectance at (a) 665 nm (MERIS λ_1), (b) 667 nm (MODIS λ_1), (c) 708 nm (MERIS λ_2), and (d) 748 nm (MODIS λ_3) for the 2008 Nebraska lakes data.

2.5.2. Comparison between the three-band and the two-band MERIS NIR-red models

The two-band MERIS NIR-red model was more reliable than the three-band MERIS NIR-red model for estimating chl-*a* concentration. This is because the reflectance at λ_3 (753 nm), which does not depend on chl-*a* concentration, is susceptible to variations due to scattering by inorganic suspended solids. The reflectance at 753 nm bears a significantly different relationship with the concentration of ISS than do the reflectances at 665 nm and 708 nm (figures 2.13 (a) and (b) and figure 2.14), thereby invalidating the assumption of spectral independence of scattering by suspended particles in the wavelength range from λ_1 through λ_3. Thus the effects of scattering by ISS are not fully removed in the three-band MERIS NIR-red model. This introduces uncertainties in chl-*a* estimation by the three-band MERIS NIR-red model, especially at low-to-moderate chl-*a* concentrations, where (i) R_{665} is greatly affected by scattering by suspended solids, and (ii) R_{λ_3} is very small and minor differences in its magnitude cause significant changes in the output of the three-band model.

The two-band MERIS NIR-red model takes full advantage of the reflectance trough around 665 nm due to absorption by chl-*a* and the reflectance peak near 700 nm which is related to both chl-*a* and suspended solids concentrations. Thus the two-band MERIS NIR-red model is very sensitive to variations in chl-*a* concentration and is stable, reliable, and accurate over a wide range of chl-*a* concentrations, and is the best suited model for application to satellite data.

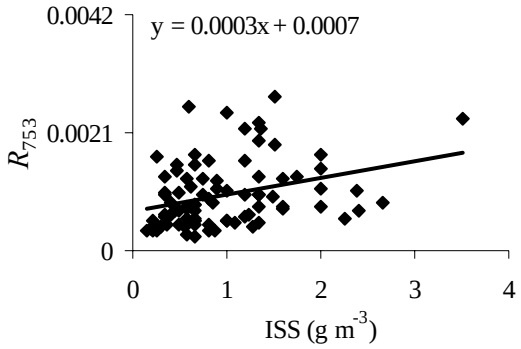

Figure 2. 14. Plot of ISS concentrations versus reflectance at 753 nm for the 2008 Nebraska lakes data.

2.6. Universal Applicability of Chl-*a* Algorithms Derived from MERIS NIR-red Models

With the ultimate goal being the development of NIR-red algorithms that can be universally applied to satellite data, it was of particular interest to test whether the parameters of the relationship between the NIR-red models and chl-*a* concentrations obtained from the data collected from Nebraska lakes are valid for waters from different geographic locations with widely varying biophysical characteristics. Given the limitation of the two-band MODIS NIR-red model for low-to-moderate chl-*a* concentrations, only the three-band and the two-band MERIS NIR-red models were tested.

The three-band and two-band MERIS NIR-red models had a much closer correlation with chl-*a* concentration for the 2008 dataset than for the 2005 dataset (figures 2.3 through 2.5 and 2.9 through 2.11). This can be attributed to the significant improvements implemented in 2008 in the techniques for collecting the reflectance data and measuring chl-*a* concentration from water samples.

The instrument set-up was kept the same for the whole season of data collection in 2008 by using the same calibration panel and the same set of Ocean Optics radiometers and optical fibers was used for measuring the upwelling radiance and downwelling irradiance. Thus the uncertainties in the data due to differences in the reflectance of the calibration standard and different transmission functions of the radiometers and the optical fibers were eliminated. In 2005, different calibration panels, and different sets of radiometers and optical fibers were used throughout the season. This meant that the data were subject to non-uniform effects due to the different transmission functions of the instruments.

The fluorometer readings were not completely stable and precise during the data collection season. There were random variations up to 5% due to instrument imprecision. The instrument was calibrated about every two-three months. However, the fluorometer readings were not stable across different calibrations. For example, when the same water samples were fluorometrically analyzed with successive calibrations, a difference up to 30% was found in the measured chl-*a* concentration between the two calibrations. In 2008, in order to account for this difference, Daniela Gurlin at the School of Natural Resources, University of Nebraska-Lincoln, measured a chl-*a* standard curve for each calibration and applied a correction factor to all the readings. Such a correction was not applied to the 2005 dataset because the errors resulting from successive calibrations were not monitored.

Thus the reflectance measurements and *in situ* chl-*a* concentrations were more accurate and reliable in the 2008 dataset than in the 2005 dataset, leading to a closer correlation between the NIR-red models and chl-*a* concentration for the 2008 dataset.

The potential universality of the relationships obtained from the 2008 Nebraska lakes dataset for the three-band and two-band MERIS NIR-red models were tested using data from the 2005 Nebraska lakes dataset and data from the Chesapeake Bay and Lake Kinneret, Israel.

The three-band and the two-band MERIS NIR-red models had the following linear relationships with chl-*a* concentration for the whole range of chl-*a* concentrations measured in 2008 (figure 2.15).

$$\text{Chl-}a = 219.32[\text{Three-Band MER NIR-red}] + 22.249 \quad (2.8)$$

$$\text{Chl-}a = 64.052[\text{Two-Band MER NIR-red}] - 42.404 \quad (2.9)$$

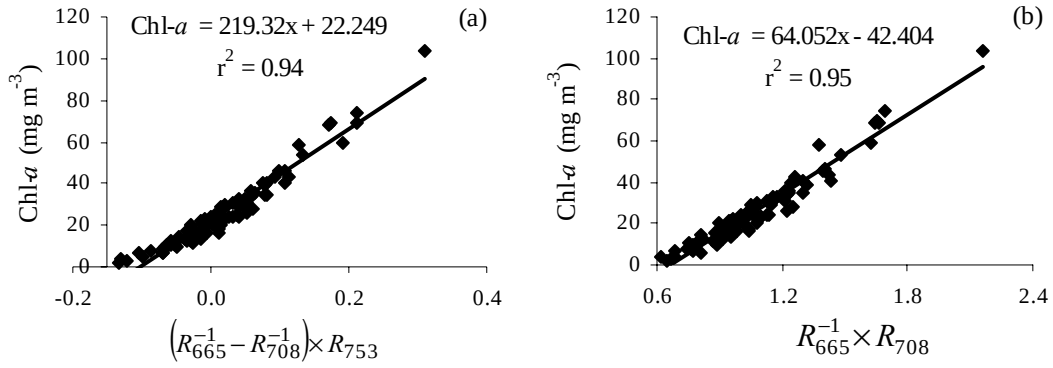

Figure 2. 15. Plots of the (a) three-band and the (b) two-band MERIS NIR-red models versus chl-*a* concentrations for 2008 Nebraska lakes data set.

2.6.1. Comparison with 2005 Nebraska Lakes Data

2.6.1(a). Three-Band MERIS NIR-red Model:

The slope and offset of the relationship between the three-band MERIS NIR-red model and chl-*a* concentration for the 2005 Nebraska lakes dataset were 179.86 and 16.037 mg m^{-3} respectively (figure 2.16), which were quite different than the corresponding figures for the 2008 Nebraska lakes dataset (equation (2.8)). When the algorithm derived from the 2008 dataset (equation (2.8)) was applied to the 2005 data,

which had chl-*a* concentrations ranging from 1.2 to 202.8 mg m^{-3}, the Root Mean Square Error (RMSE) of chl-*a* estimation was 19.74 mg m^{-3} (figure 2.17).

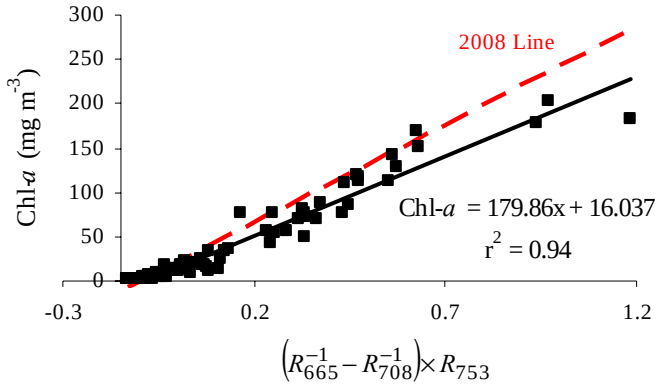

Figure 2. 16. Plot of the three-band MERIS NIR-red model versus chl-*a* concentration for the 2005 dataset. The red dashed line is the line of linear regression of the three-band MERIS NIR-red model with chl-*a* concentration for the 2008 dataset.

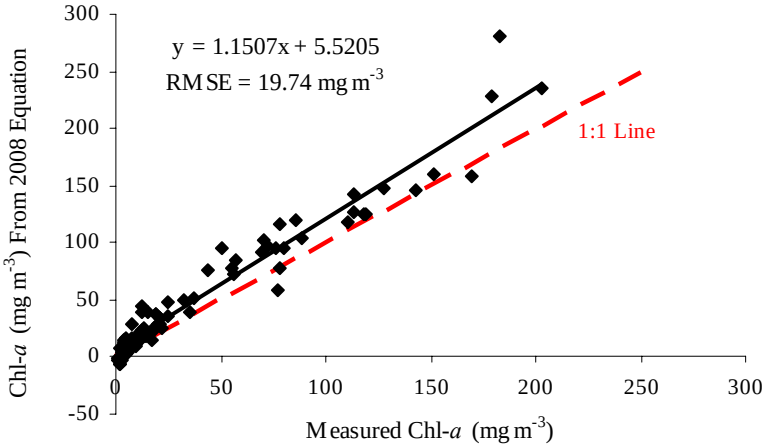

Figure 2. 17. Plot of chl-*a* concentrations measured *in situ* in 2005 versus chl-*a* concentrations estimated using the 2008 three-band MERIS NIR-red algorithm.

2.6.1(b). Two-Band MERIS NIR-red Model:

The slope and offset of the relationship between the two-band MERIS NIR-red model and chl-*a* concentration for the 2005 dataset, 64.038 and -48.46 mg m^{-3} respectively (figure 2.18), were quite close to the corresponding figures for the 2008 dataset (equation (2.9)). When the algorithm derived from the 2008 dataset (equation

(2.9)) was applied to the 2005 data, the RMSE was 13.13 mg m^{-3} (figure 2.19), which is much lower than that for the three-band MERIS NIR-red model (figure 2.17).

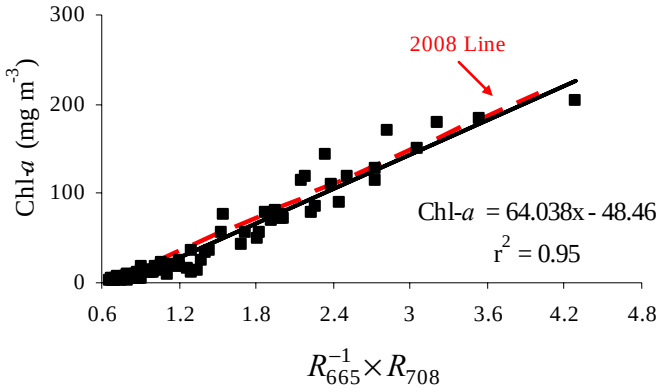

Figure 2. 18. Plot of the two-band MERIS NIR-red model versus chl-*a* concentration for the 2005 dataset. The red dashed line is the line of linear regression of the two-band MERIS NIR-red model with chl-*a* concentration for the 2008 dataset.

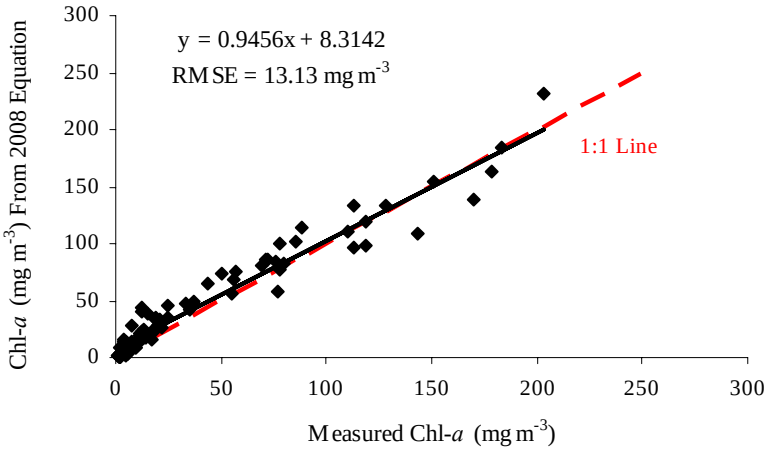

Figure 2. 19. Plot of chl-*a* concentrations measured *in situ* in 2005 versus chl-*a* concentrations estimated using the 2008 two-band MERIS NIR-red algorithm.

2.6.2. Comparison with 2009 Lake Kinneret Data

Measurements of *in situ* chl-*a* concentration and surface reflectance were taken at Lake Kinneret on 13th May, 26th May, 31st May, and 15th June of 2009 by Dr. Yosef Yacobi and the crew at the Kinneret Limnological Laboratory, Israel. The lake, which is

usually eutrophic in this season, was uncharacteristically not productive during the time of data collection, resulting in chl-*a* concentrations less than 21 mg m^{-3}.

For the 2008 Nebraska dataset, the relationships between the three-band and two-band MERIS NIR-red models and chl-*a* concentration were not perfectly linear for the whole range of chl-*a* concentrations. A slight change in slope can be observed for chl-*a* concentration less than 25 mg m^{-3} (figure 2.15). Considering the low chl-*a* concentrations in the Lake Kinneret dataset, regression equations from the 2008 dataset for chl-*a* concentrations in the range 0-25 mg m^{-3} (equations (2.10) and (2.11); figure 2.20) were chosen instead of the regression equations for the entire range of chl-*a* concentrations.

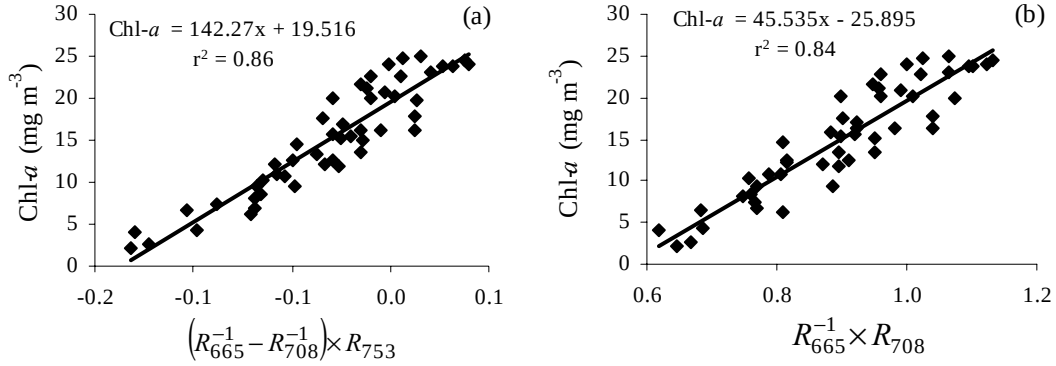

Figure 2. 20. Plots of the (a) three-band and the (b) two-band MERIS NIR-red models versus chl-*a* concentrations for the 2008 Nebraska lakes dataset for chl-*a* < 25 mg m^{-3}.

The linear regression equations for the three-band and two-band MERIS NIR-red models from the 2008 dataset were,

For chl-*a* < 25 mg m^{-3},

$$\text{Chl-}a = 142.27[\text{Three-Band MER NIR-red}] + 19.516 \quad (2.10)$$

$$\text{Chl-}a = 45.535[\text{Two-Band MER NIR-red}] - 25.895 \quad (2.11)$$

2.6.2(a). Three-Band MERIS NIR-red Model:

The overall relationship between the three-band MERIS NIR-red model and chl-*a* concentration was reasonably good, with a coefficient of determination of 0.89. Figure 2.21 shows a plot of three-band MERIS NIR-red model values versus chl-*a* concentration. The red dotted line represents the linear regression line for the relationship between the model values and chl-*a* concentration for the 2008 Nebraska lakes dataset. The plot was characterized by (i) a horizontal scatter of points for chl-*a* concentration below 7 mg m^{-3} (these points show large variations in model values for virtually the same chl-*a* concentration), (ii) a close correlation between the model values and chl-*a* concentration but a distinctly lower slope than that for the 2008 Nebraska lakes data, for chl-*a* concentrations between 7 and 15 mg m^{-3}, and (iii) a close correlation and a similar slope to that for the 2008 Nebraska lakes data, for chl-*a* concentrations higher than 15 mg m^{-3}.

The horizontal scatter of points for chl-*a* concentrations below 7 mg m^{-3}, which was observed for the two-band MERIS NIR-red model as well (figure 2.23), could be due to uncertainties in the fluorometric measurements of chl-*a* concentration. The effect of these uncertainties, which could amount up to 3 mg m^{-3} (Y. Z. Yacobi, personal communication), is more pronounced at low chl-*a* concentrations and can greatly affect the relationship between the model values and low chl-*a* concentrations.

The lower slope observed for chl-*a* concentrations between 7 and 15 mg m^{-3} could be due to the inherent behavior of the three-band NIR-red model at low chl-*a* concentrations. The reflectance at λ_3 depends only on scattering by suspended matter and absorption by water, and has no correlation with chl-*a* concentration. As described in

section 2.5.2, the effect of particulate scattering on reflectance is different at λ_3 than at λ_1 and λ_2. This makes the three-band NIR-red model quite susceptible to variations in backscattering coefficient, especially at low chl-*a* concentrations. It is plausible that the suspended particles in Lake Kinneret might have been of a different size distribution than those in Nebraska lakes, resulting in distinctly different values for backscattering coefficient than those for Nebraska lakes for similar chl-*a* concentrations. This probable difference in backscattering coefficient could explain the difference in slope for chl-*a* concentrations between 7 and 15 mg m^{-3}. Nevertheless, with a lack of actual measurements of backscattering coefficient, this reason cannot be affirmed definitely.

Due primarily to the performance of the model at low chl-*a* concentrations, the overall slope and offset, 82.804 and 18.089 respectively, were significantly different than those from the 2008 Nebraska lakes dataset (equation (2.10)). The algorithm from the 2008 Nebraska lakes dataset, when applied to the Lake Kinneret dataset, resulted in negative chl-*a* concentrations for several stations. The overall RMSE was 4.78 mg m^{-3} (figure 2.22).

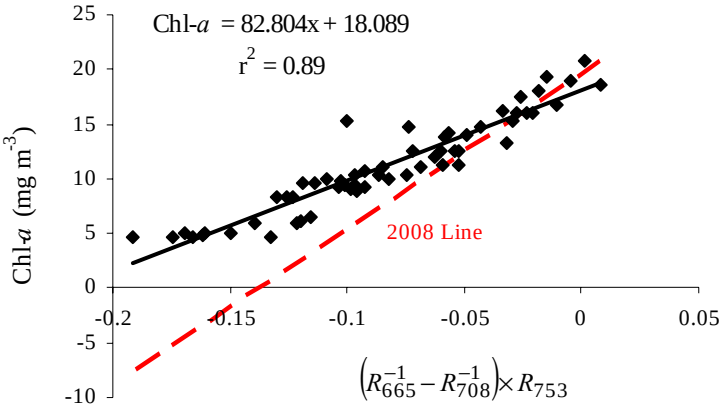

Figure 2. 21. Plot of the three-band MERIS NIR-red model versus chl-*a* concentration for the Lake Kinneret dataset. The red dashed line is the line of linear regression of the three-band MERIS NIR-red model with chl-*a* concentration for the 2008 dataset.

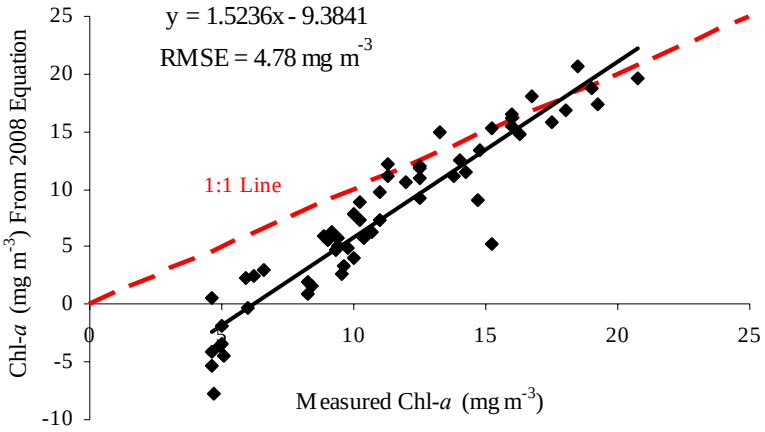

Figure 2. 22. Plot of chl-*a* concentrations measured *in situ* in Lake Kinneret versus chl-*a* concentrations estimated using the 2008 three-band MERIS NIR-red algorithm.

2.6.2(b) Two-Band MERIS NIR-red Model:

The relationship between the two-band MERIS NIR-red model and chl-*a* concentration for the Lake Kinneret data was similar to that for the 2008 Nebraska lakes data (figure 2.23). The slope and offset were 42.509 and -23.81 mg m^{-3}, respectively, which were similar to the corresponding figures, 45.535 and -25.895 mg m^{-3}, respectively (equation 2.11), for the 2008 Nebraska lakes data. As with the plot for the three-band MERIS NIR-red model (figure 2.21), there is a horizontal scatter of points for chl-*a* concentrations below 7 mg m^{-3}. In addition to the possibility of uncertainties in fluorometric measurements of chl-*a* concentration, another reason for poorer performance of the two-band MERIS NIR-red model at this low chl-*a* range is that, at low chl-*a* concentrations, the reflectance peak occurs at a much shorter wavelength than 708 nm (at around 690-685 nm (Gitelson 1992)).This results in the model benefiting less from the reflectance peak, which is crucial to the performance of the two-band MERIS NIR-red model.

When the algorithm developed using the 2008 Nebraska lakes dataset (equation (2.11)) was applied to the Lake Kinneret data, the RMSE was 1.46 mg m^{-3} (figure 2.24).

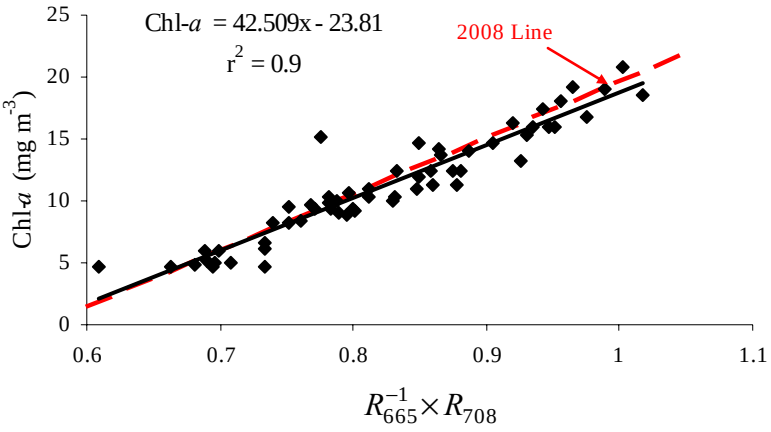

Figure 2. 23. Plot of the two-band MERIS NIR-red model versus chl-*a* concentration for the Lake Kinneret dataset. The red dashed line is the line of linear regression of the two-band MERIS NIR-red model with chl-*a* concentration for the 2008 dataset.

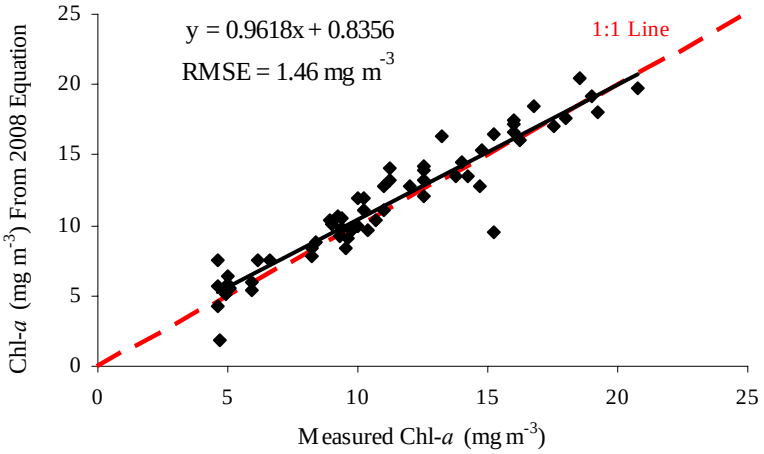

Figure 2. 24. Plot of chl-*a* concentrations measured *in situ* in Lake Kinneret versus chl-*a* concentrations estimated using the 2008 two-band MERIS NIR-red algorithm.

2.6.3. Comparison with 2006 Chesapeake Bay Data

In April 2006, measurements of *in situ* chl-*a* concentration and surface reflectance were taken on Choptank River and a few tributaries of the Chesapeake Bay. The dataset

contained 11 stations with chl-*a* concentrations ranging from 6.21 to 34.89 mg m^{-3}. The linear regression equations from the 2008 Nebraska lakes data for chl-*a* concentration less than 35 mg m^{-3} (equations (2.12) and (2.13); figure 2.25) were applied.

For chl-*a* < 35 mg m^{-3},

$$\text{Chl-}a = 166.33[\text{Three-Band MER NIR-red}] + 21.012 \quad (2.12)$$

$$\text{Chl-}a = 50.693[\text{Two-Band MER NIR-red}] - 29.977 \quad (2.13)$$

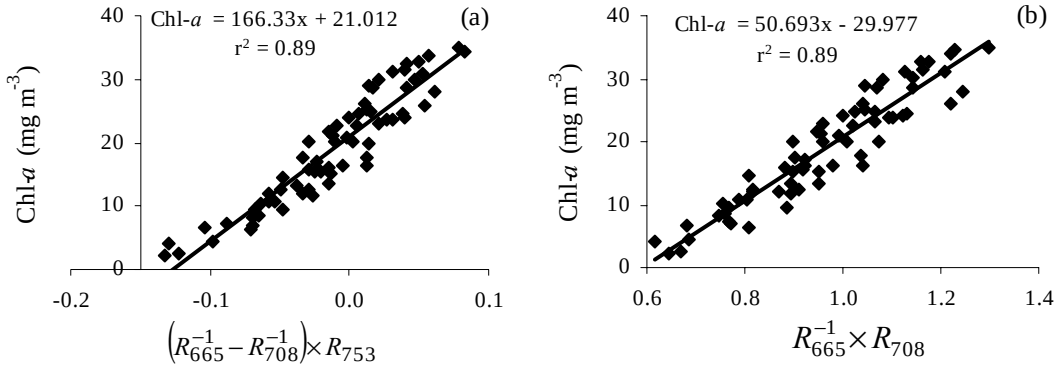

Figure 2. 25. Plots of the (a) three-band and the (b) two-band MERIS NIR-red models versus chl-*a* concentrations for the 2008 Nebraska lakes dataset for chl-*a* < 35 mg m^{-3}.

2.6.3(a). Three-Band MERIS NIR-red Model:

The three-band MERIS NIR-red model had a very close relationship with chl-*a* concentration, with a coefficient of determination of 0.98 (figure 2.26). The linear regression line was almost parallel to that for the 2008 Nebraska lakes data, with an offset of about 4 mg m^{-3} between the two regression lines. When the algorithm developed from the 2008 Nebraska lakes data (equation 2.12) was applied to the Chesapeake Bay data, the RMSE was 3.63 mg m^{-3} (figure 2.27).

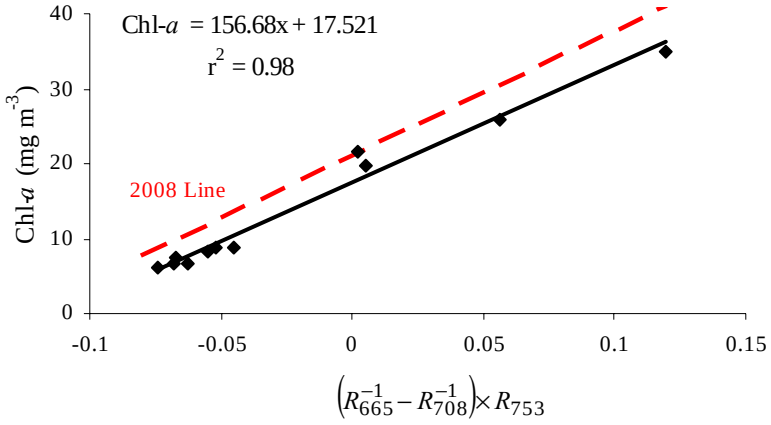

Figure 2. 26. Plot of the three-band MERIS NIR-red model versus chl-*a* concentration for the Chesapeake Bay dataset. The red dashed line is the line of linear regression of the three-band MERIS NIR-red model with chl-*a* concentration for the 2008 dataset.

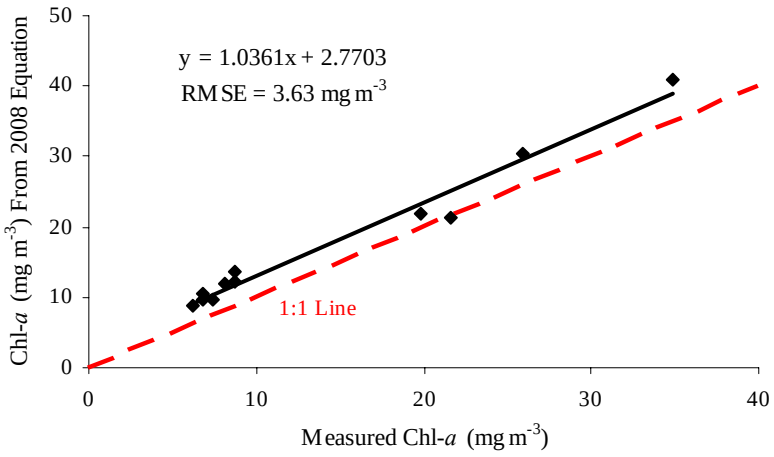

Figure 2. 27. Plot of chl-*a* concentrations measured *in situ* in Chesapeake Bay versus chl-*a* concentrations estimated using the 2008 three-band MERIS NIR-red algorithm.

2.6.3(b). Two-Band MERIS NIR-red Model:

The two-band MERIS NIR-red model also had a very close relationship with chl-*a* concentration, with a coefficient of determination of 0.97. The linear regression line was virtually parallel to the regression line for the 2008 Nebraska lakes data, with an offset of about 2 mg m^{-3} (figure 2.28). When the algorithm developed using the 2008

Nebraska lakes data (equation 2.13) was applied to the Chesapeake Bay data, the RMSE was 3.42 mg m^{-3} (figure 2.29).

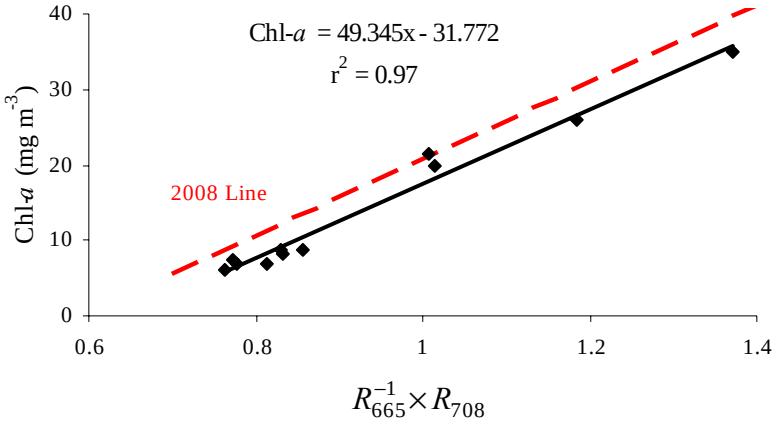

Figure 2. 28. Plot of the two-band MERIS NIR-red model versus chl-*a* concentration for the Chesapeake Bay dataset. The red dashed line is the line of linear regression of the two-band MERIS NIR-red model with chl-*a* concentration for the 2008 dataset.

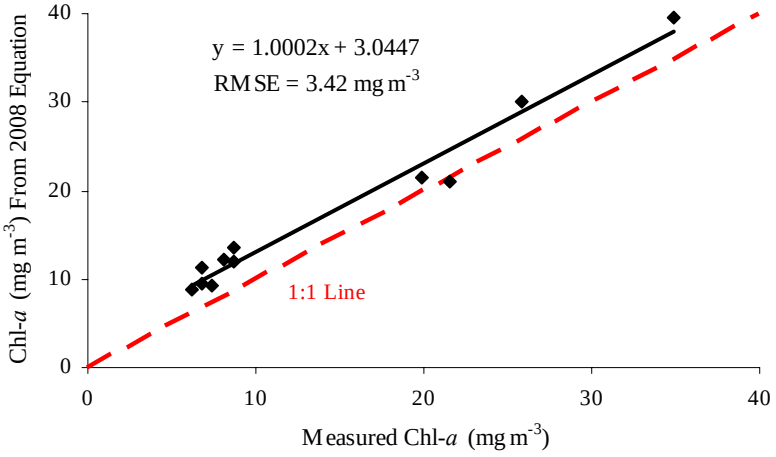

Figure 2. 29. Plot of chl-*a* concentrations measured *in situ* in Chesapeake Bay versus chl-*a* concentrations estimated using the 2008 two-band MERIS NIR-red algorithm.

2.7. Conclusion

The results presented in the preceding sections lead to the following conclusions:

1. **The MERIS NIR-red models have a high potential for universal applicability**

The data used in the previous section came from waters with widely varying biophysical characteristics and from different geographical locations. Yet the MERIS NIR-red models, especially the two-band MERIS NIR-red model, had a very stable relation with chl-*a* concentration. The algorithms developed from the 2008 Nebraska lakes dataset, when applied to data collected from different water bodies, gave accuracies (calculated as $\text{accuracy} = (\text{RMSE}/\text{range of chl-}a\text{ concentration}) \times 100$) higher than 80% for the three-band MERIS NIR-red model and 90% for the two-band MERIS NIR-red model. This shows that the algorithms do not need to be re-parameterized for each different water body. The universal applicability of the algorithms needs to be further tested with data from many more turbid productive water bodies from different geographic locations and under different climatic regimes. Most of the suspended matter in the lakes sampled in 2005 and 2008 was of organic nature. On average, ISS composed less than 19% of TSS in the lakes that were used to develop the algorithms. The algorithms need to be tested using data from lakes with higher proportions of ISS concentration. Nevertheless, the results obtained so far provide a firm basis for developing algorithms that can be routinely applied to satellite data.

2. **The two-band MODIS NIR-red model is unreliable for estimating low-to-moderate chl-*a* concentrations**

This is because the reflectance at 748 nm is not sensitive to variations in chl-*a* concentration since it depends mostly only on scattering by suspended particles in addition to absorption by water. The sensitivity of the model to random variations due

to scattering by suspended particles is more pronounced at low-to-moderate chl-*a* concentrations (< 25 mg m^{-3}), where the magnitude of reflectance at 748 nm is very low. Thus, this model includes one term (R_{667}) that is affected by absorption by chl-*a* and other constituents as well as scattering by suspended particles, and another term (R_{748}) that is affected only by scattering by suspended particles, in addition to absorption by water, which is independent of the concentrations of constituents. The ratio, R_{748}/R_{667} , does not eliminate the effects of scattering, especially at low-to moderate chl-*a* concentrations. This is because the values of backscattering coefficient at 667 nm and 748 nm might be different. Moreover, the two-band MODIS NIR-red model does not take advantage of the effect of reflectance peak around 700 nm (Gitelson 1992), which is related to chl-*a* concentration. Nevertheless, the model gives reasonably good accuracies for moderate-to-high chl-*a* concentrations and can be applied to satellite data to detect algal bloom conditions and also estimate chl-*a* concentration in such conditions.

3. The two-band MERIS NIR-red model is more reliable than the three-band MERIS NIR-red model

Due to reasons described in section 2.5.2, the two-band MERIS NIR-red model has a definite advantage over the three-band MERIS NIR-red model and is the most suitable NIR-red model for application to satellite data.

Chapter 3. Application of Satellite-based NIR-red Models to Aircraft Data

Testing the NIR-red models using data collected by sensors mounted on low-flying aircrafts is a good and essential intermediary step before applying the models to satellite data. Aircraft data provide several advantages over satellite data for the purpose of testing the models. Data acquisitions can be planned to coincide with *in situ* data collections in fine weather conditions. This minimizes the effect of temporal variations in the water body between the *in situ* data collection and the remotely sensed data acquisition, and eliminates the loss of remotely sensed data due to adverse atmospheric conditions such as cloud cover and haze. At low-flying altitudes, data can be acquired at high spatial resolutions in continuously placed narrow spectral bands. With programmable scanners, the spectral channel locations can be adjusted to match the specific spectral model that is being analyzed.

This chapter contains results obtained in applying the NIR-red models to data from airborne sensors as a prelude to applying the models to satellite data. First, models based on optimal spectral bands suggested by Dall'Olmo and Gitelson (2005) were tested. Then models based on spectral bands that match the MERIS spectral channels were tested. The objective was to test whether the MERIS NIR-red models, which were shown to be reliable and accurate for data collected with field spectrometers, yield comparable reliability and accuracy for data from airborne sensors. Since an airborne sensor sees through a lesser portion of the Earth's atmosphere than does a space-borne sensor, the atmospheric effect on aircraft data will be lesser than on satellite data, but still

significant. The sensitivity of the models to non-uniform atmospheric effects on different days in a multi-temporal dataset was also analyzed.

3.1. Data

In 2008, five images were acquired by Rick Perk, (manager of CALMIT Hyperspectral Airborne Monitoring Program at the University of Nebraska-Lincoln), over the Fremont State Lakes using the hyperspectral sensor, AISA-Eagle (Airborne Imaging Spectrometer for Applications), mounted on a Piper Saratoga aircraft that was flown at an altitude of about 3 km above ground. The images were acquired on 02nd July, 14th July, 26th September, 25th October, and 19th November of 2008, with *in situ* reflectance and chl-*a* concentrations measured coincidentally on all these days except for 25th Oct 2008, when the *in situ* data were collected a day earlier (on 24th Oct 2008). The overall dataset contained 35 stations, with a wide range of chl-*a* concentrations (Table 3.1).

Date	Min.	Median	Max.	Mean	Standard Deviation	Coefficient of Variation	Number of Stations
02 July 08	4.35	16.20	22.68	14.04	6.68	0.48	7
14 July 08	6.59	13.54	20.80	13.80	5.98	0.43	6
26 Sep 08	8.47	31.06	68.62	31.11	19.04	0.61	8
25 Oct 08	9.42	27.02	69.23	32.23	21.33	0.66	6
19 Nov 08	2.07	20.25	74.19	26.85	25.11	0.94	8

Table 3. 1. Descriptive statistics of chl-*a* data (in mg m^{-3}) from the five campaigns.

AISA is a programmable imaging spectrometer. A maximum of 256 continuous spectral channels are possible in the 400 – 970 nm wavelength range, with spectral resolution as high as 2.3 nm. The central wavelength location and the bandwidth of the spectral channels are programmable, enabling the acquisition of data with the desired

spectral characteristics based on the specific research need. The sensor has a peak signal–to–noise ratio of 490, obtained for a typical vegetation target. At a flight altitude of about 10,000 ft (~ 3 km) above ground, the sensor acquires data at a spatial resolution of 2 m. More detailed information on the sensor characteristics can be obtained at www.specim.fi. The images used in this research had a spectral resolution of 10 nm and a spatial resolution of 2 m.

Figure 3. 1. Screen-shot of a true-color composite of an AISA image acquired over the Fremont State Lakes.

3.2. Application of the NIR-red models

The at-sensor radiance recorded by the AISA sensor was processed using the software CaliGeo (which is the default software for processing raw AISA data) and converted to remote sensing reflectance, and the NIR-red models were applied to the reflectance data.

A three-band model,

$$\text{Chl-}a \propto \left(R_{671}^{-1} - R_{710}^{-1}\right) \times R_{740} \tag{3.1}$$

and a two-band model,

$$\text{Chl-}a \propto \left(R_{675}^{-1} \times R_{705}\right) \tag{3.2}$$

suggested by Dall'Olmo and Gitelson (2005) were considered. The AISA data suffered heavily from instrument noise in the NIR region. As a result, reflectances at wavelengths beyond 730 nm (where there is high absorption by water) were uncharacteristically high and thus unreliable. This is illustrated in figure 3.2, where the AISA at-sensor reflectance is plotted together with the reflectance measured *in situ* with the Ocean Optics® radiometers for the same station. Apart from the strong oxygen absorption feature at 760 nm, there is no spectrally significant atmospheric phenomenon taking place in the range 730 nm – 800 nm. Therefore, atmospheric correction could not correct the abnormally high reflectance values at wavelengths beyond 730 nm (figure 3.2 (b)). Thus the abnormally high reflectance values recorded by the AISA sensor are attributable to instrument noise, which is particularly more pronounced due to very low signal at this spectral region.

Due to this high influence of instrument noise, the three-band model had to be modified with λ_3 at 723 nm, which is within the range recommended by Dall'Olmo and Gitelson (2005). For λ_1 and λ_2, AISA spectral channels closest to Dall'Olmo and Gitelson's wavebands were used. Thus, the three-band and two-band NIR-red models applied to AISA data were,

$$\text{The Three-Band AISA NIR-red Model: } \text{Chl-}a \propto \left(R_{676}^{-1} - R_{704}^{-1}\right) \times R_{723} \tag{3.3}$$

The Two-Band AISA NIR-red Model: Chl-$a \propto \left(R_{676}^{-1} \times R_{704}\right)$ (3.4)

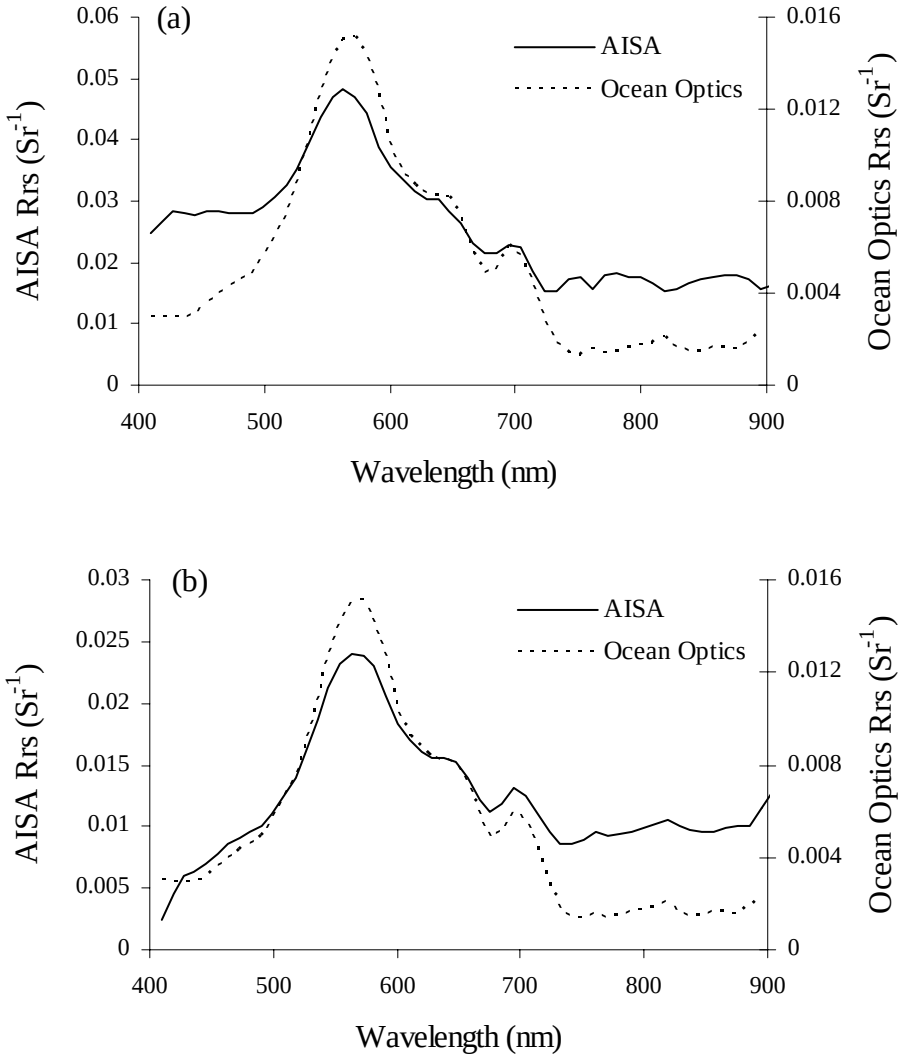

Figure 3. 2. Plots comparing *in situ* reflectance measured just below the water surface using Ocean Optics ® radiometers with (a) AISA at-sensor reflectance and (b) atmospherically corrected (using FLAASH (section 3.2.1)) AISA surface reflectance.

When data from the five individual campaigns were plotted separately, both the three-band and the two-band NIR-red models (equations (3.1) and (3.2)) consistently had very close correlations with chl-*a* concentrations. The coefficient of determination was

higher than 0.85 for the three-band model and higher than 0.87 for the two-band model (figures 3.3 and 3.4).

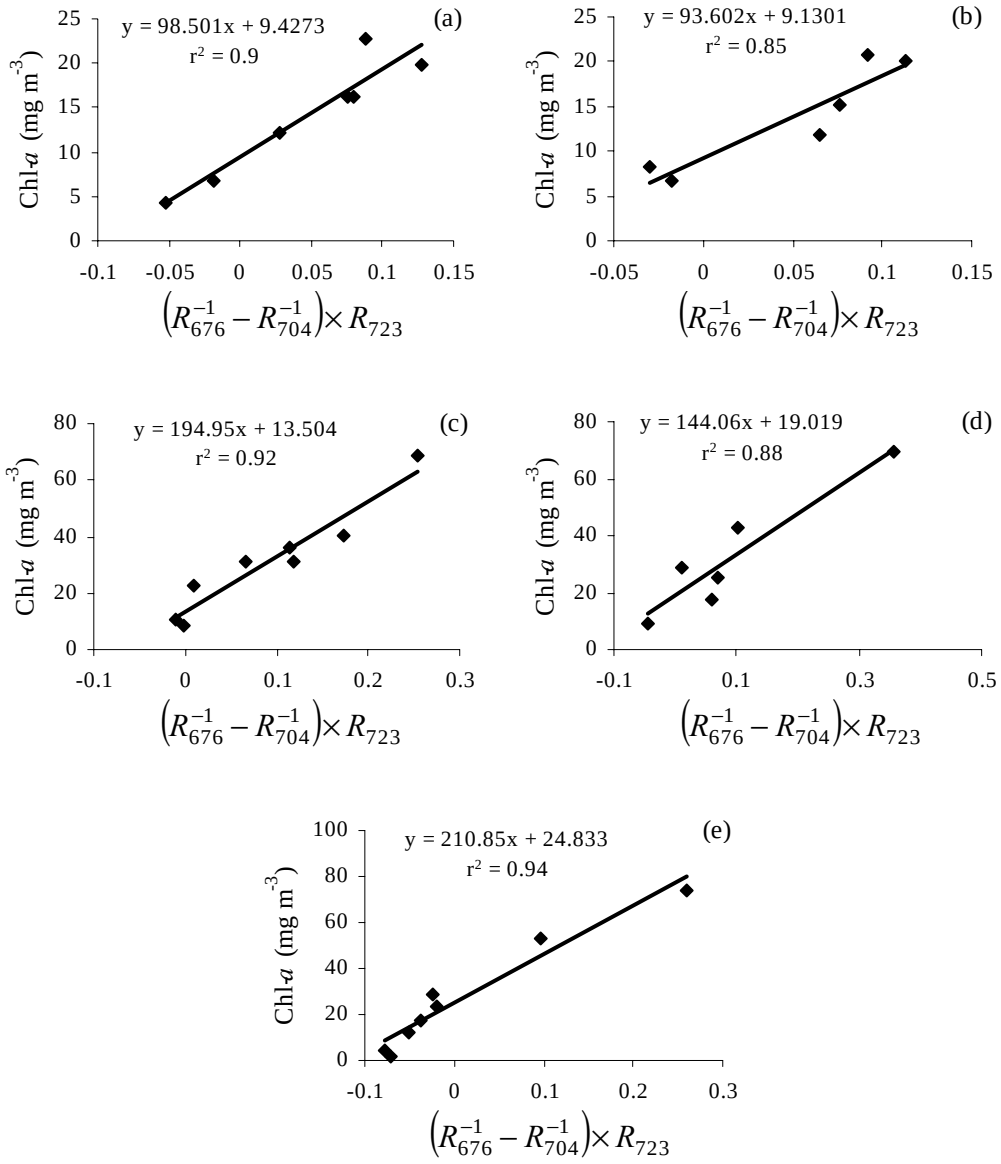

Figure 3. 3. Plots of three-band AISA NIR-red model versus *in situ* chl-*a* concentration for (a) 02nd July, (b) 14th July, (c) 26th Sep, (d) 25th Oct, and (e) 19th Nov 2008 data.

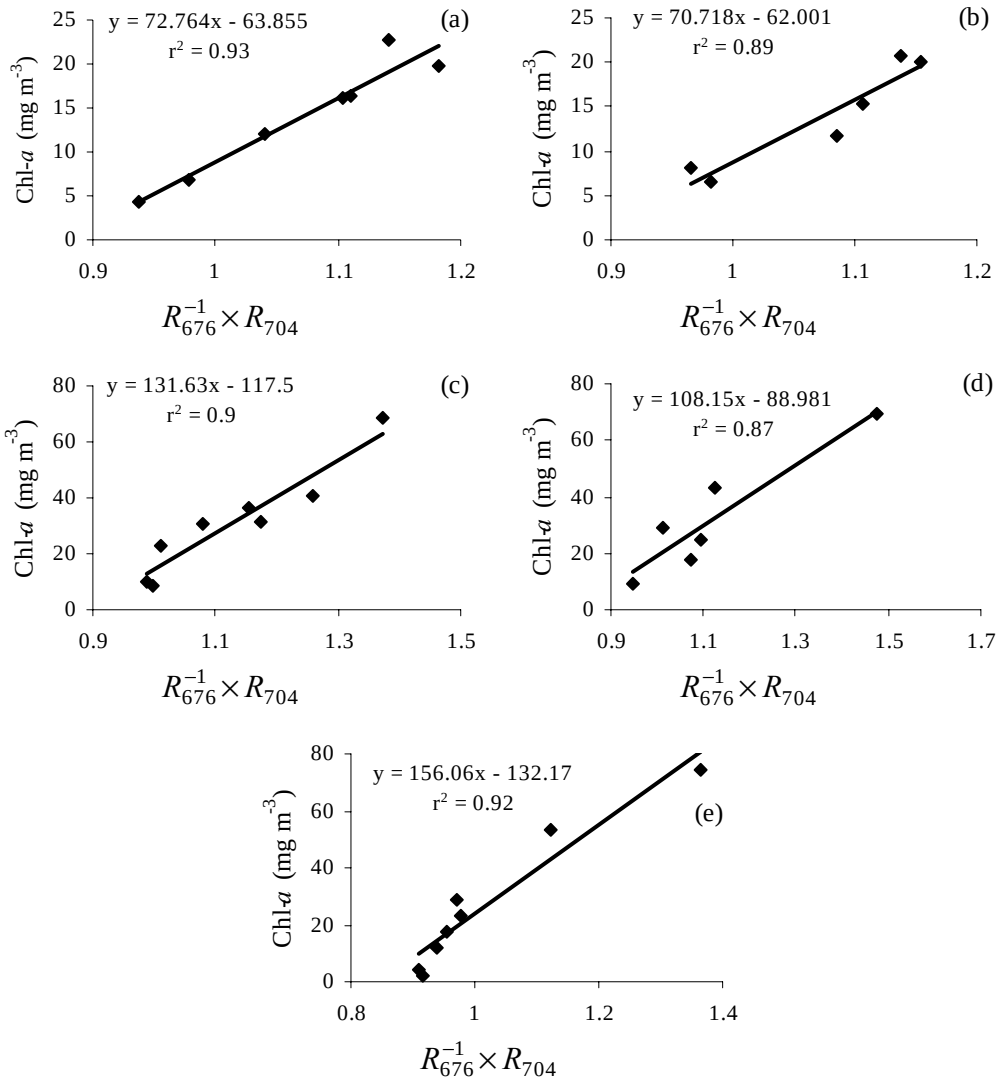

Figure 3. 4. Plots of two-band AISA NIR-red model versus *in situ* chl-*a* concentration for (a) 02nd July, (b) 14th July, (c) 26th Sep, (d) 25th Oct, and (e) 19th Nov 2008 data.

However, the slope and offset of the relationships between the model values and chl-*a* concentration varied significantly across the different dates (figures 3.3, 3.4, 3.5(a) and 3.6(a)). Thus, for both models, when data from all five campaigns were plotted together, the overall relationships between the model values and chl-*a* concentration were significantly poorer (figures 3.5(b) and 3.6(b)) than what was obtained for each individual campaign. The overall coefficient of determination was 0.73 for the three-band

AISA NIR-red model and 0.72 for the two-band AISA NIR-red model. The data points were quite scattered away from the regression lines for chl-*a* concentrations in the range 15 – 50 mg m^{-3}. Such inconsistencies in the slope and offset of the relationships impede the development of a reliable algorithm that can be routinely applied to remotely sensed data acquired on different days. Considering the fact that the NIR-red models, when applied to *in situ* measured reflectance data, had a consistent relationship with chl-*a* concentration for multiple datasets from different water bodies (Chapter 2), these differences in slope and offset across the different days are not due to variations in the biophysical properties of water. Rather, they are attributable to non-uniform atmospheric effects on the AISA images on these different days. Hence, the AISA images were atmospherically corrected.

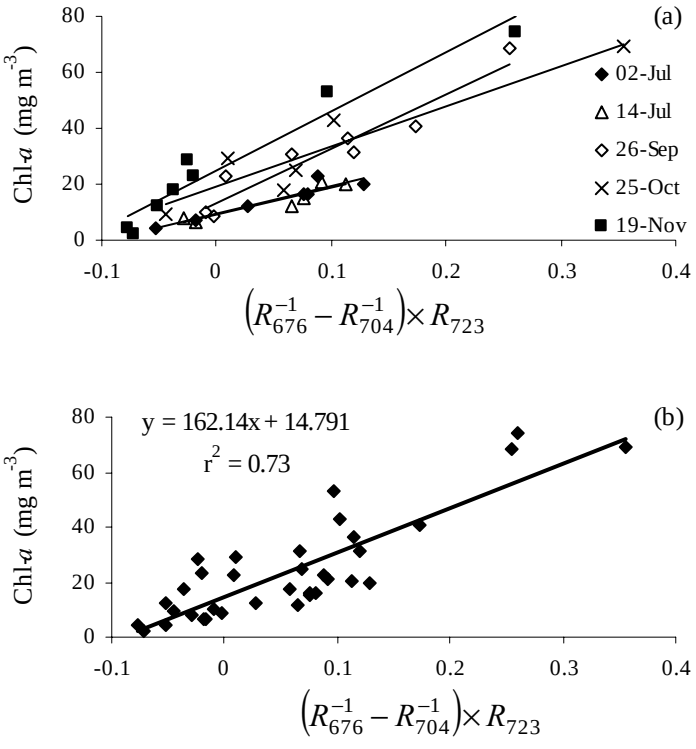

Figure 3. 5. Plots of the three-band AISA NIR-red model versus chl-*a* concentration, showing (a) the regression lines for the individual campaigns and (b) the overall regression line.

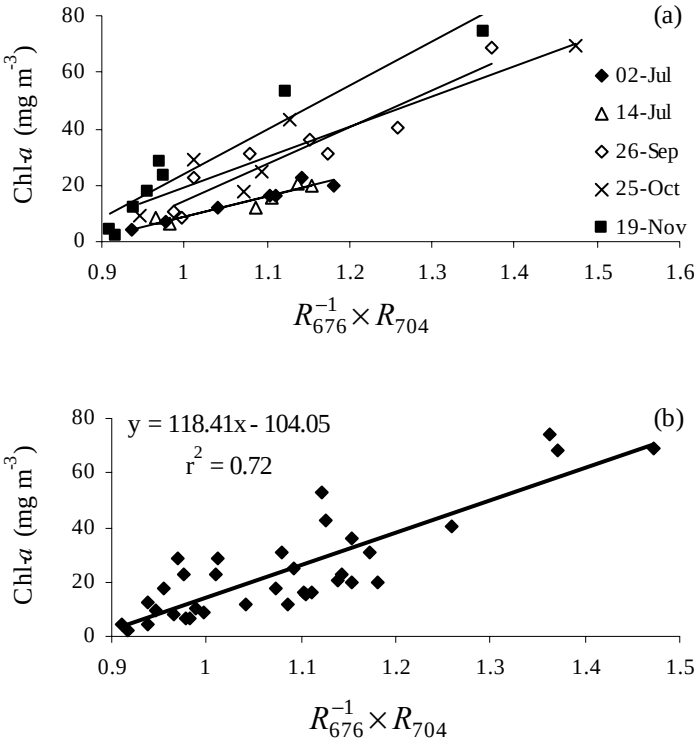

Figure 3. 6. Plots of the three-band AISA NIR-red model versus chl-*a* concentration, showing (a) the regression lines for the individual campaigns and (b) the overall regression line.

3.2.1. Atmospheric Correction of AISA Images

The AISA images were atmospherically corrected using the program FLAASH (Fast Line-of-sight Atmospheric Analysis of Spectral Hypercubes; developed by Spectral Sciences Inc.), which can be obtained as an add-on to the image processing software, ENVI (Environment for Visualizing Images), from ITT – VIS (International Telephone and Telegraph – Visual Information Solutions). The objective was to test whether atmospheric correction could remove the non-uniform atmospheric effects on the AISA images and produce results such that the slope and offset of the relationships between the NIR-red models and chl-*a* concentration are similar for all five images.

Atmospheric Correction by FLAASH

FLAASH is a 'first-principles' atmospheric correction program. First-principles atmospheric correction typically involves three steps, viz., (i) Retrieval of atmospheric parameters (primarily, visibility/ optical depth, aerosol type, and column water vapor amount), (ii) Solution of the radiative transfer equation using the retrieved/derived atmospheric parameters and conversion of the radiance values into reflectance values, and (iii) Spectral polishing to remove spectral artifacts that may have been introduced during the correction process (Matthew et al. 2002).

FLAASH is based on the radiative transfer code, MODTRAN 4 (MODerate spectral resolution atmospheric TRANsmittance). MODTRAN is an improvement from the earlier code, LOWTRAN (LOW resolution TRANsmission). MODTRAN 4 was jointly developed by Spectral Sciences Inc. and the Air Force Research Laboratory (AFRL). It has all the features and capabilities of the latest version of LOWTRAN, LOWTRAN 7, with some upgrades. One of the important upgrades implemented in MODTRAN is the higher spectral resolution for calculating gaseous absorption. Spectral resolution for absorption measurements is normally expressed in the frequency domain (as wavenumbers). LOWTRAN 7 has a spectral resolution of $20\ \text{cm}^{-1}$ over the entire spectral range of $0 - 50,000\ \text{cm}^{-1}$ (or $0.2\ \mu\text{m}$ - infinity) (Abreu and Anderson 1996). MODTRAN 2/3 had a spectral resolution of $2\ \text{cm}^{-1}$ over the range, $0 - 22,680\ \text{cm}^{-1}$ (> 440 nm) and $20\ \text{cm}^{-1}$ over the range, $22,680 - 50,000\ \text{cm}^{-1}$ (200 – 440 nm). The latest release of MODTRAN 4 has an even higher resolution of $1\ \text{cm}^{-1}$ (Adler-Golden et al. 1999).

Some of the other upgrades include the addition of the multi-stream DISORT (DIScrete Ordinate Radiative Transfer) method to handle multiple scattering (Berk et al. 1998), a Bidirectional Reflectance Distribution Function (BRDF) with adjacency effect modeling to account for reflections from adjacent pixels on non-uniform surfaces (Acharya et al. 1999; Berk et al. 2000) , and the ability to handle spherical refractive geometry for limb observations (Berk et al. 2000). The algorithms for calculating multiple scattering have been improved, resulting in better performance of the model for data with cloudy or heavy aerosol loading conditions (Berk et al. 1998).

For the purpose of describing atmospheric profiles for the spectral modeling of atmospheric radiative processes and for calculating the atmospheric gaseous absorption, MODTRAN takes into consideration the seven principal atmospheric gases, viz., H_2O, CO_2, O_3, N_2O, CO, CH_4, and O_2, and also trace gases, such as, NO, SO_2, NO_2, NH_3, HNO_3, OH, HF, HCl, HBr, HOCl, CH_3Cl, H_2O_2, C_2H_2, H_2S, PH_3, etc. (Abreu and Anderson 1996). The importance of atmospheric gases is judged not based on their concentrations but on their contribution to atmospheric radiative processes.

FLAASH essentially serves as a user-interface to MODTRAN 4. As such, with the way the program is designed, it gives limited control to the user to choose and change the processing parameters. FLAASH is rather simple to execute in terms of the procedures as long as the user is able to specify appropriate input parameters. Default values or appropriate guesses (based on theoretical estimates or information from the literature) are used as input parameters when user-supplied data are not available. Atmospheric correction is implemented as an iterative process in which the spectral information from the image is used to determine atmospheric parameters. The input

parameters that describe the atmosphere serve as initial values that direct the iterative processes towards convergence. Accurate input parameters are helpful in achieving quick convergence, by way of reducing the number of iterations, but do not generally change the spectral shape of the final output reflectance significantly. Figures 3.7 and 3.8 show screen-shots of the Graphical User Interface (GUI) windows that FLAASH uses to accept the input parameters.

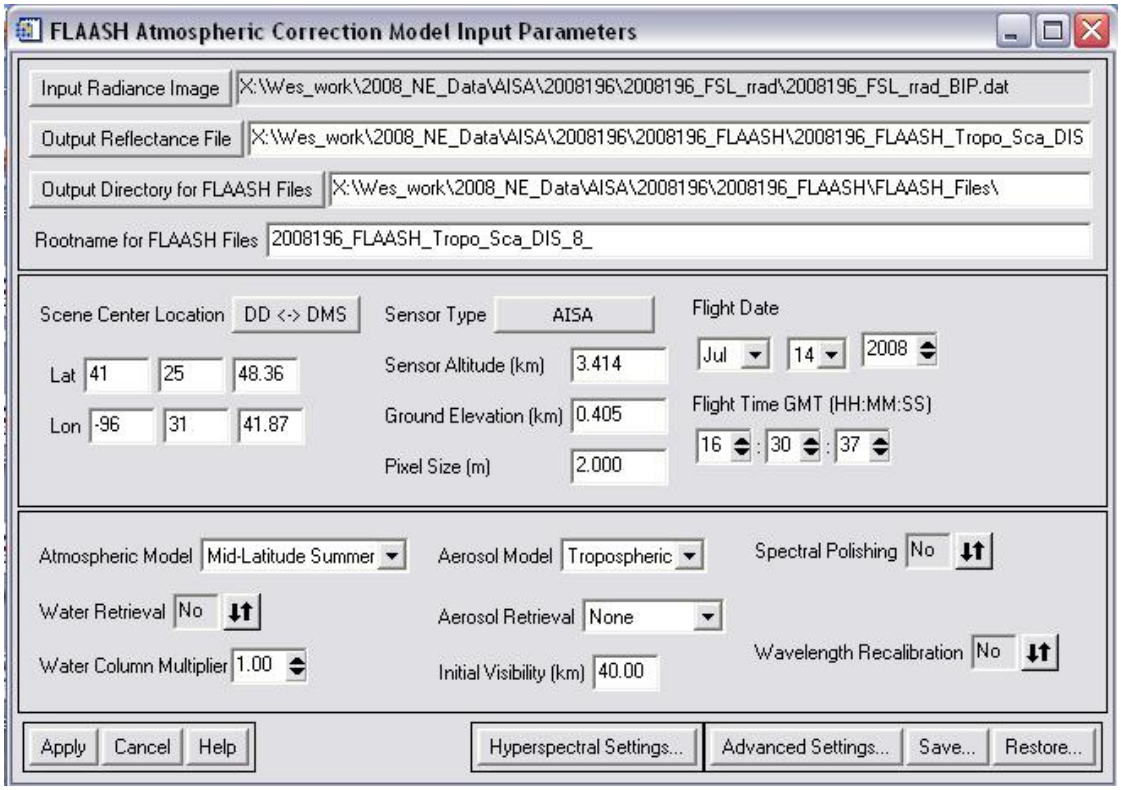

Figure 3. 7. Screen-shot of FLAASH GUI for feeding basic input parameters

The visibility, aerosol scale height, carbon-di-oxide (CO_2) mixing ratio are the basic atmospheric data parameters required by FLAASH. Since actual measurements of these parameters were not available, FLAASH was executed with default values for these parameters (visibility 40 km, aerosol scale height 2 km, and CO_2 mixing ratio 390 ppm)

for all five AISA images. Based on the guidelines from the FLAASH User Manual, the atmospheric model was chosen as ‘Mid-Latitude Summer’. Since the AISA data did not include strong water absorption channels, the option of retrieving vertical column water-vapor on a pixel-by-pixel basis was not possible. Thus the program had to assume uniform column water-vapor over the whole image. Based on the guidelines from the FLAASH User Manual, the atmospheric model, which depends on the geographic location and the season of the year, was chosen as ‘Mid-Latitude Summer’ for the 02nd July, 14th July, 26th Sep, and 25th Oct images, and ‘Sub-Arctic Summer’ for the 19th Nov image.

The program was executed repeatedly with a different choice each time for the aerosol model type. The aerosol types considered were, ‘No Aerosol’, Rural Aerosol, and Tropospheric Aerosol. Rural aerosol model represents aerosols in areas that are not strongly affected by urban or industrial sources. The particle sizes are a blend of two distributions – one large and one small. The tropospheric aerosol model represents clear and calm conditions over land, and it consists of the small-particle component of the rural model (Gordon and Morel 1983) (FLAASH Module User's Guide 2008).

As noted earlier, adjusting the input parameters had virtually no effect on the spectral shape of the output reflectances. The choice of aerosol model and the initial visibility value, which is a measure of the aerosol loading on a given day, affected the program’s assumption of the amount of contribution from particulate scattering to the input radiance. Accordingly, varying these parameters affected the magnitude of the output reflectance, with the shape remaining virtually the same.

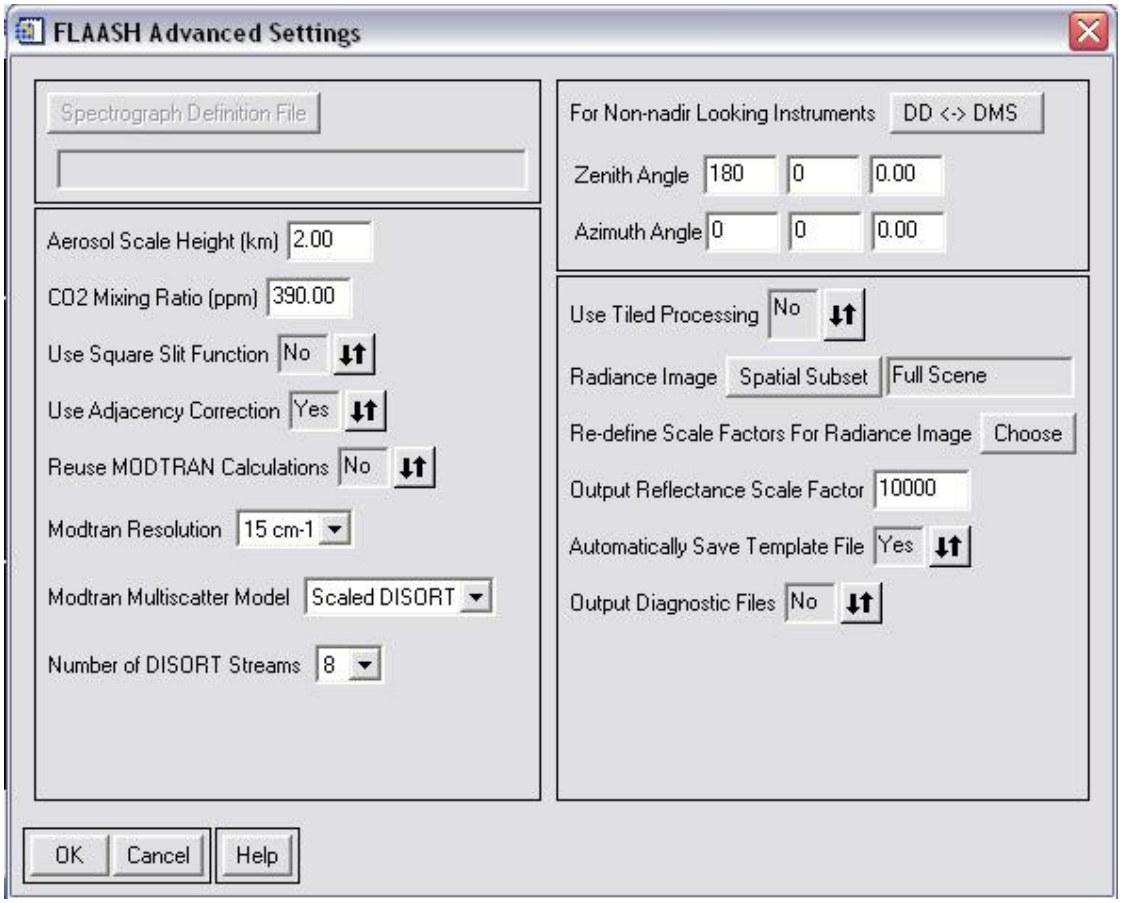

Figure 3. 8. Screen-shot of FLAASH GUI for feeding advanced input parameters

For each of the three aerosol models considered (No Aerosol, Rural Aerosol, and Tropospheric Aerosol), FLAASH was executed on all five AISA images by keeping the rest of the input parameters the same. When the input parameters were kept the same for all the images, the results were similar to those before atmospheric correction. The NIR-red model values were closely related to chl-*a* concentration for each individual image but the slope and offset varied across the different images, similar to the pattern observed in the results from the uncorrected AISA images. This suggested that FLAASH atmospheric correction with the same input parameters for all five images did not effectively remove the non-uniform atmospheric effects in the images. Figure 3.9 shows

the results for the 'No Aerosol' model with initial visibility set as 40 km. A similar pattern was obtained for the rural and tropospheric aerosol models as well.

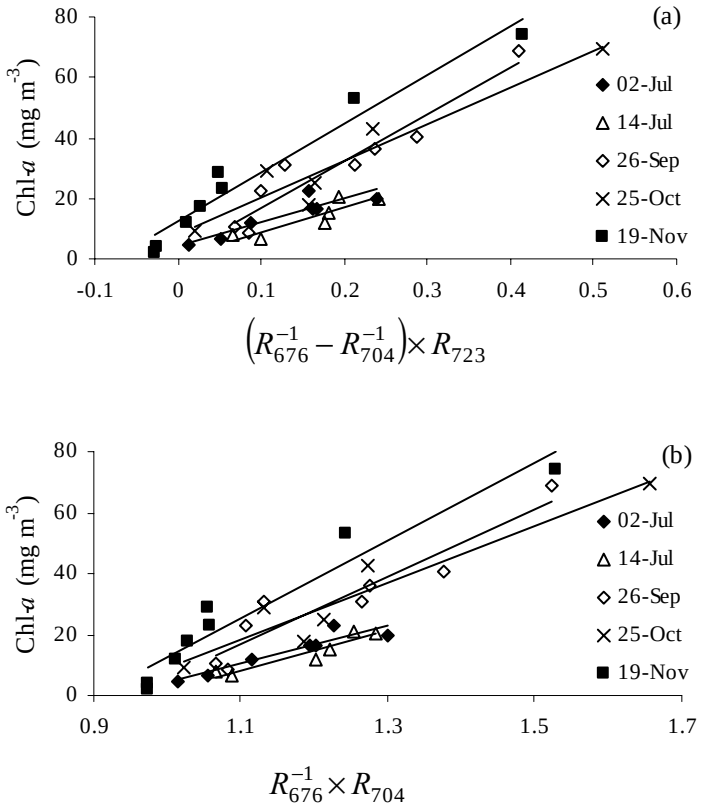

Figure 3. 9. Plots of (a) three-band AISA NIR-red model and (b) two-band AISA NIR-red model versus chl-*a* concentration for AISA images atmospherically corrected through FLAASH with the 'No Aerosol' model setting and initial visibility 40 km for all five images.

Based on the uncorrected at-sensor reflectance spectra from the five images (figure 3.10), it is apparent that the aerosol loading was not the same on all five days. The high values of reflectance in the blue region and the apparent slant tilt of the reflectance curves indicate a higher amount of particulate scattering on 26th Sep, 25th Oct, and 19th Nov than on 02nd July and 14th July. Hence it was decided to adjust the initial visibility and aerosol model settings independently for each image and thus feed input parameters

to FLAASH that were indicative of the different amounts of atmospheric particulate scattering in the images.

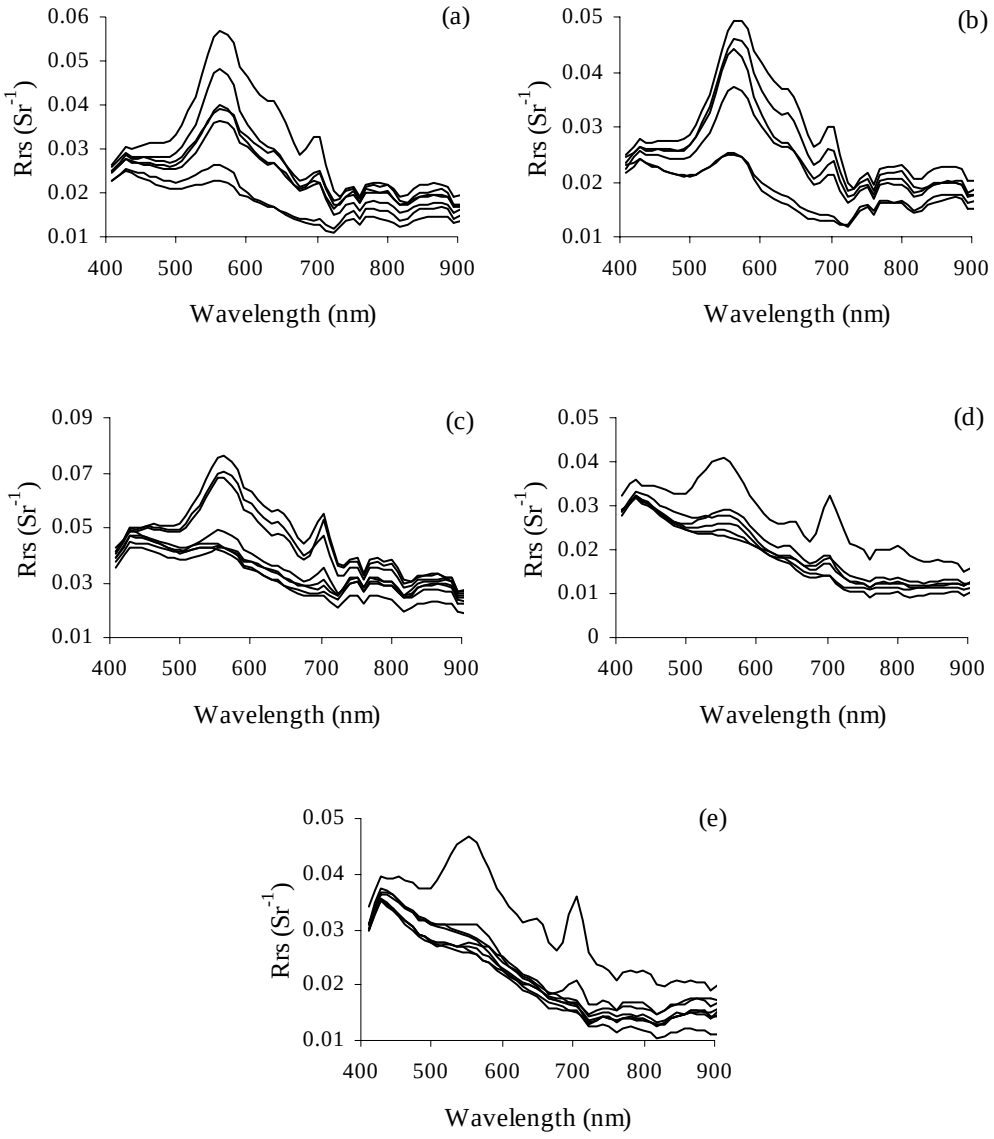

Figure 3. 10. At-sensor remote sensing reflectance spectra acquired by AISA over Fremont State Lakes on (a) 02nd July, (b) 14th July, (c) 26th Sep, (d) 25th Oct, and (e) 19th Nov of 2008.

Incidentally, the slope and offset of the relationships were similar for the 02nd July and 14th July images before atmospheric correction (figures 3.5 and 3.6) and after atmospheric correction with the same input parameters (figure 3.9), indicating that the

atmospheric effects on both these images were similar if not exactly the same. Hence the initial visibility and aerosol model settings were kept the same for both these images. Since radiations with shorter wavelengths get scattered the most, the magnitude of at-sensor reflectance in the blue region was used as a coarse relative indicator of the amount of atmospheric particulate scattering in each image. Thus the input parameters were adjusted such that, among the five images, FLAASH was to assume the highest amount of atmospheric particulate scattering in the 26th Sep image, followed by 19th Nov image, the 25th Oct image, and the 02nd & 14th July images.

In general, FLAASH tended to over-correct for atmospheric particulate scattering, resulting in negative reflectances, especially at shorter wavelengths. Hence, the input parameters for the five images were set conservatively and adjusted judiciously (table 3.2) so as to minimize the occurrence of negative reflectances in the output and still capture the relative variations in the atmospheric particulate scattering among the five images. When the images were corrected using the input parameters shown in table 3.2, the linear relationships between the NIR-red model values and chl-*a* concentration for the five images got remarkably close to each other in their slope and offset (figure 3.11). However, this uniformity in the relationship between the NIR-red models and chl-*a* concentration for images acquired on different days cannot be used to reliably calibrate the models to estimate chl-*a* concentration from airborne hyperspectral data because of the lack of actual measurements of atmospheric parameters to corroborate the input parameter settings for the atmospheric correction procedure. Nevertheless, the results strongly suggest that with an accurate correction procedure for atmospheric effects,

which accounts for non-uniform atmospheric effects on multi-temporal data, the NIR-red models can be calibrated for hyperspectral data from airborne sensors.

Date	Aerosol Model	Initial Visibility (km)
02 Jul 08	No Aerosol	40
14 Jul08	No Aerosol	40
26 Sep 08	Rural	30
25 Oct 08	Rural	60
19 Nov 08	Rural	40

Table 3. 2. Relatively adjusted input settings for aerosol model and initial visibility used in FLAASH atmospheric correction of AISA images

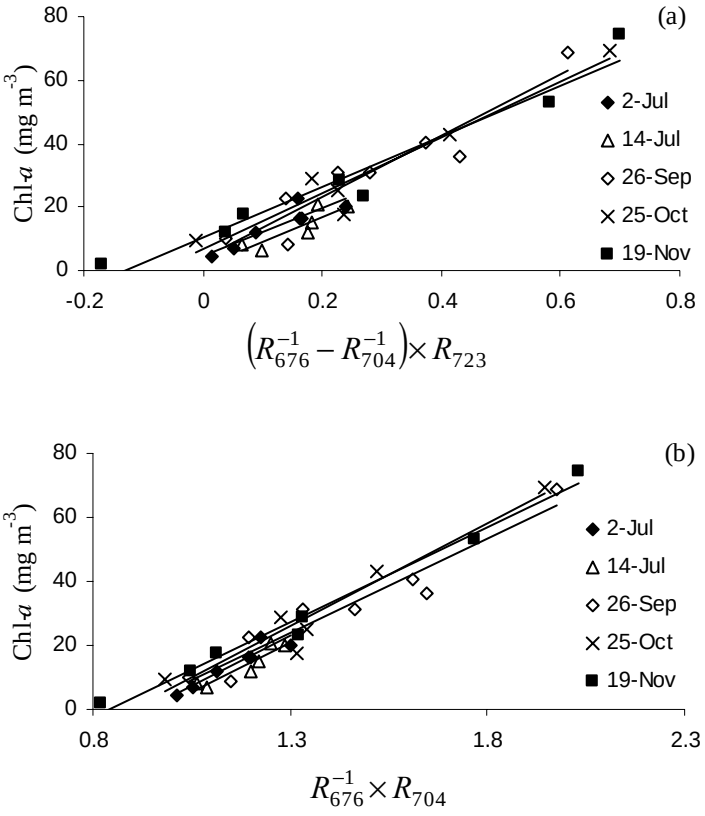

Figure 3. 11. Plots of (a) three-band AISA NIR-red model and (b) two-band AISA NIR-red model versus chl-*a* concentration after atmospheric correction, with the input parameters as shown in table 3.2.

3.3. Application of the MERIS NIR-red Models

Because of the unreliability of AISA reflectance values beyond 730 nm, the three-band MERIS NIR-red model was not tested. Selecting the spectral bands closest to MERIS spectral channels, the two-band MERIS NIR-red model for AISA data was formulated as follows:

$$\text{Two-band AISA-MERIS NIR-red model: Chl-}a \propto \left(R_{666}^{-1} \times R_{704}\right) \quad (3.5)$$

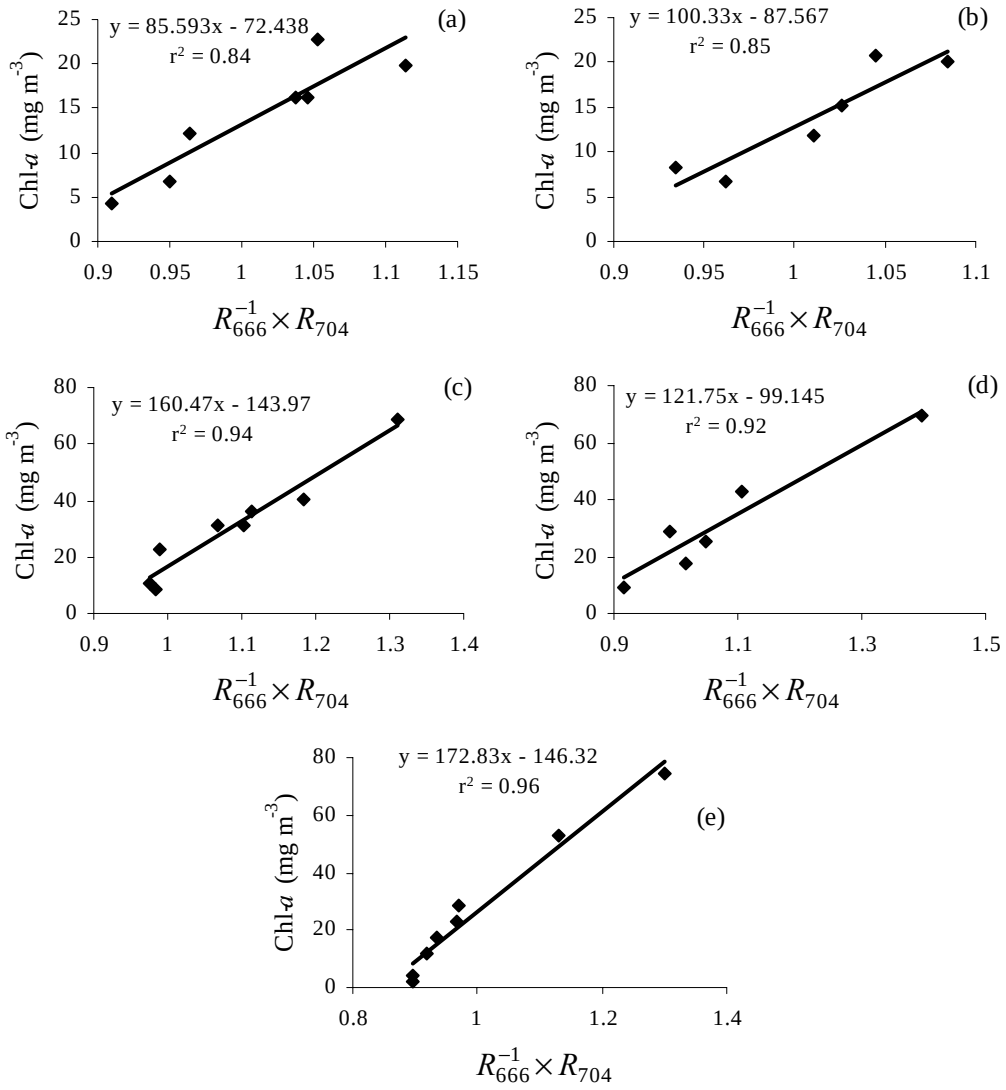

Figure 3. 12. Plots of two-band AISA-MERIS NIR-red model versus *in situ* chl-*a* concentration for (a) 02nd July, (b) 14th July, (c) 26th Sep, (d) 25th Oct, and (e) 19th Nov 2008 data before atmospheric correction.

The results for the two-band AISA-MERIS NIR-red model had a similar pattern as did the results from three-band and two-band AISA NIR-red models. When applied to AISA data before (figure 3.12) and after (figure 3.13) atmospheric correction with the same input parameters for all images, the two-band AISA-MERIS NIR-red model had close correlations with chl-*a* concentration for each individual image. But the slope and offset of the relationship varied significantly across the images (figures 3.14 and 3.15).

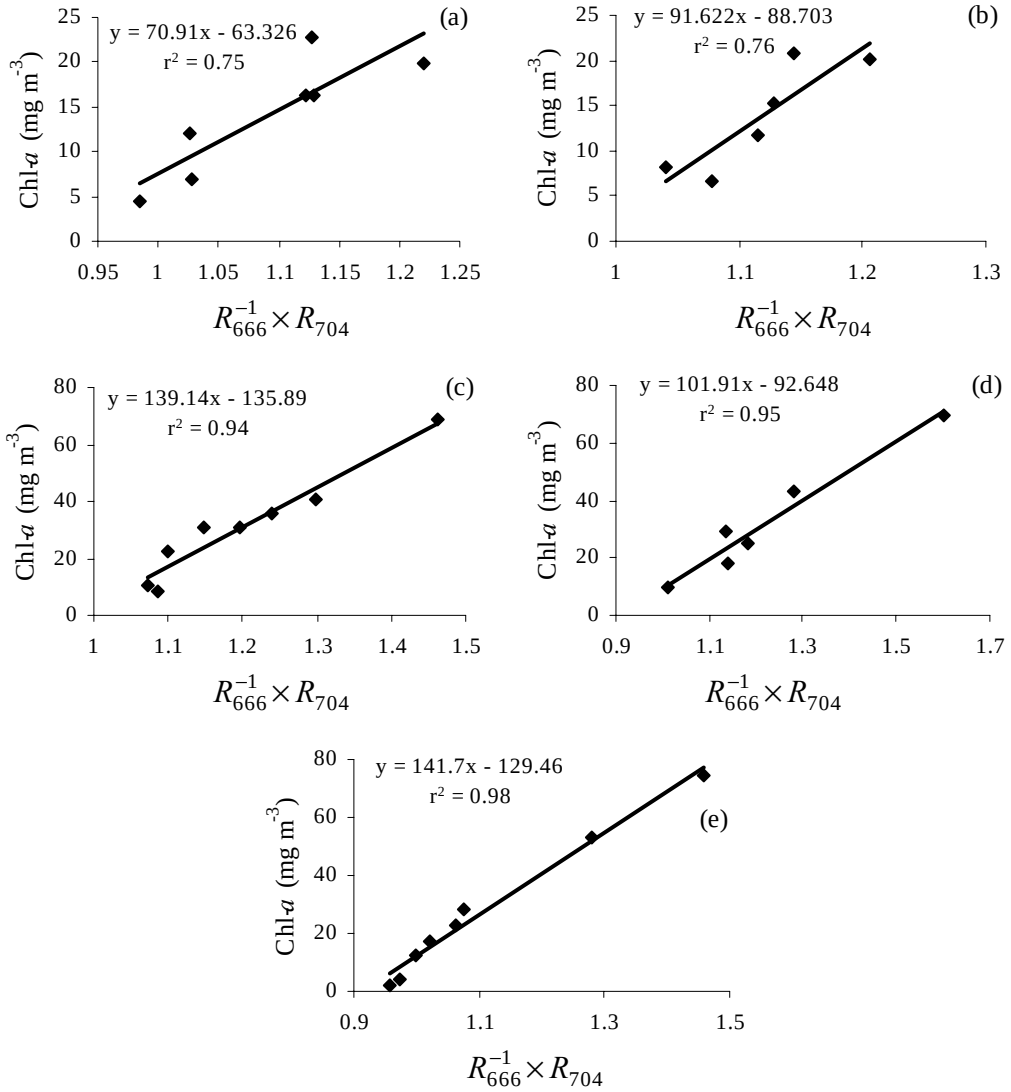

Figure 3. 13. Plots of two-band AISA-MERIS NIR-red model versus *in situ* chl-*a* concentration for (a) 02nd July, (b) 14th July, (c) 26th Sep, (d) 25th Oct, and (e) 19th Nov 2008 data after atmospheric correction with the 'No Aerosol' model setting and initial visibility 40 km.

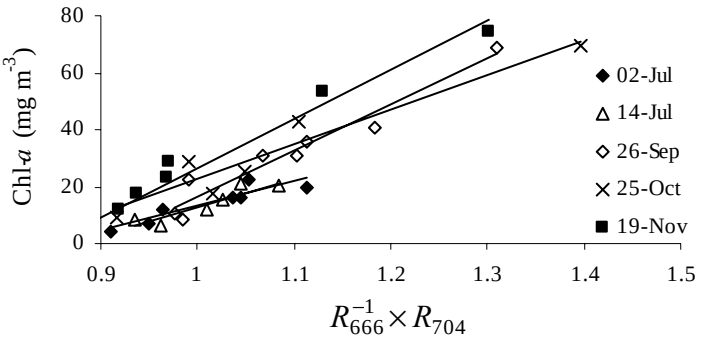

Figure 3. 14. Plot of the two-band AISA-MERIS NIR-red model versus chl-*a* concentration showing the linear regression lines for the individual campaigns, for AISA data before atmospheric correction.

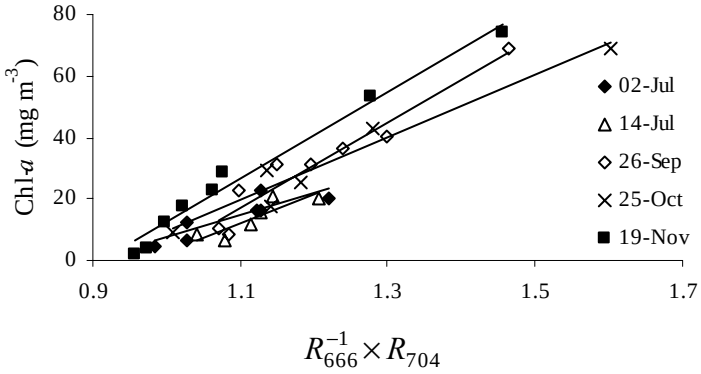

Figure 3. 15. Plot of the two-band AISA-MERIS NIR-red model versus chl-*a* concentration for AISA images atmospherically corrected through FLAASH with the 'No Aerosol' model setting and initial visibility 40 km.

When the input parameters for FLAASH were adjusted relative to the apparent atmospheric particulate scattering in each image, with the input parameters set as shown in table 3.2, linear relationships between the NIR-red models and chl-*a* concentration for the five images got close to each other in their slope and offset (figure 3.16).

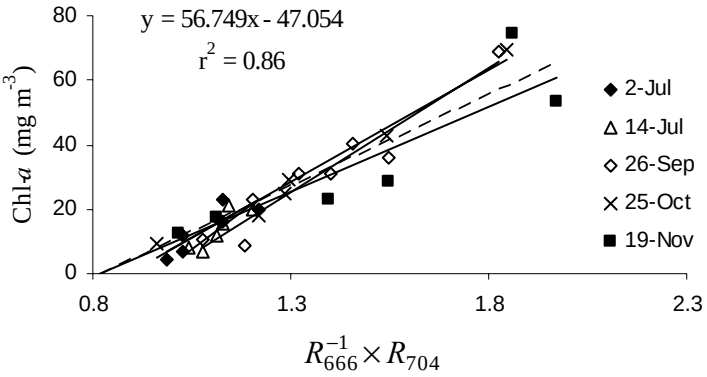

Figure 3. 16. Plot of two-band AISA-MERIS NIR-red model versus chl-*a* concentration after atmospheric correction, with the input parameters for atmospheric correction adjusted relatively.

3.4. Conclusion

The output from the three-band and two-band NIR-red models based on optimal spectral bands for AISA and the two-band NIR-red model based on AISA spectral bands that were closest to MERIS spectral bands had close correlations with chl-*a* concentrations, consistently for each of the five AISA images. However, the slope and offset of the linear relationship varied from image to image, which was attributed to the non-uniform atmospheric effects on the different days of image acquisition. Atmospheric correction of the AISA images was attempted in order to account for the non-uniform atmospheric effects and result in similar slope and offset for all five images. The input parameters were adjusted relatively such that the initial assumptions of the atmospheric correction procedure reflected the observed differences in the atmospheric particulate scattering in the five images. Atmospheric correction with relative adjustment of input parameters resulted in slopes and offset that were similar for all five images, suggesting that provided the atmospheric correction procedure can effectively remove the non-

uniform atmospheric effects on multi-temporal images, then the NIR-red models can be calibrated to estimate chl-*a* concentration from multi-temporal dataset.

Nevertheless the uniform slope and offset obtained by the relative atmospheric adjustment procedure in this study could not be used to calibrate the NIR-red model for estimating chl-*a* concentration from aircraft data because the input parameters fed into the atmospheric correction program were not based on actual measurements but on educated guess. *In situ* measurements of aerosol optical thickness taken at the time of image acquisition using a sun photometer should be used to set the input parameter values. If the atmospheric correction program is reliable and consistent, feeding input parameters based on actual measurements of aerosol optical thickness should result in atmospherically corrected output that lend to uniform relationships between the model values and chl-*a* concentrations for multi-temporal data. If slopes and offsets still vary across the images, then there might be a problem with the atmospheric correction procedure itself, which will have to be evaluated using coincidentally measured *in situ* radiance data. This, of course, assumes that the other relevant issues such as the quality and reliability of the spectral data from the airborne sensor have been sufficiently dealt with. If FLAASH does not uniformly remove the non-uniform atmospheric effects, then other atmospheric correction programs such as TAFKAA (The Algorithm Formerly Known As TAFKAA (Gao et al. 2000; Montes et al. 2001)) that are based on radiative transfer models should be tried. The other alternative would be procedures such as the Empirical Line Method (Kruse et al. 1990) that rely on calibrated references targets within each image.

A uniform slope and offset, resulting from a consistent and effective removal of non-uniform atmospheric effects, can be used to calibrate the two-band MERIS NIR-red model. Often, atmospheric correction procedures do not result in complete removal of atmospheric effects. The corrected output often carries some residual atmospheric effects or effects introduced by the atmospheric correction procedure and effects due to any spectral anomaly inherent in the radiance data from the sensor. The influence of these factors (which are specific to the atmospheric correction procedure and the type of sensor) on the performance of the NIR-red models should be assessed before a universal algorithm can be developed for multi-temporal data from other airborne sensors.

The results illustrate the ability of the two-band MERIS NIR-red model to estimate chl-*a* concentration in turbid productive waters using remotely sensed data from airborne sensors. With a robust atmospheric correction procedure that effectively removes the non-uniform atmospheric effects on multi-temporal data, a reliable two-band MERIS NIR-red algorithm can be developed, which can be applied to multi-temporal data from airborne as well as space-borne sensors.

Chapter 4. NIR-red Spectral Algorithms for Satellite Data – Results, Limitations, and Challenges

The ultimate objective of this research has been to develop NIR-red spectral algorithms that can be routinely applied for accurately estimating chl-*a* concentration from multi-temporal satellite data acquired over turbid productive waters with varied biophysical characteristics and from different geographic locations around the globe. Achieving this objective has challenges on several fronts. First, the spectral algorithm, which should be maximally sensitive to variations in chl-*a* concentration and minimally sensitive to absorption and scattering of light by constituents other than chl-*a*, must have a stable relationship with chl-*a* concentration irrespective of variations in the concentrations of other constituents. The results shown in chapters 2 and 3 confirm that the MERIS NIR-red models (especially the two-band MERIS NIR-red model) meet this condition. Furthermore, the radiance recorded by the sensor should be adequately corrected for atmospheric effects, resulting in reasonably valid reflectance values so that the spectral algorithm can be applied reliably, or, the spectral algorithm should be sufficiently resistant to atmospheric effects so that it precludes the need for a rigorous atmospheric correction procedure. The problem of calibrating and validating spectral algorithms for satellite data is further compounded by the differences in the spatial resolutions of the satellite data and *in situ* 'ground truth' data and the temporal difference between the times of satellite data acquisition and *in situ* data collection. This chapter contains the results and the issues encountered in developing MERIS NIR-red spectral algorithms for satellite data.

This chapter has four parts. The first part (section 4.2) deals with the description and significance of atmospheric correction procedures. The second part (section 4.3) illustrates the close relationships that the NIR-red models have with phytoplankton biophysical characteristics. The third part (section 4.4) deals with the calibration and validation of three-band and two-band MERIS NIR-red algorithms for estimating chl-*a* concentration and their comparisons with a few other standard algorithms. The limitations and challenges encountered in developing a reliable satellite algorithm are described in the fourth part (section 4.5).

4.1. Data

The *in situ* data consisted of analytical measures of the concentrations of chl-*a* and TSS from the Kremenchug Reservoir and the Dnieper Estuary in Ukraine, and the Taganrog Bay and the Azov Sea in Russia. The data were collected by the crews at the Southern Scientific Center of the Russian Academy of Sciences, Rostov-on-Don, Russia, and the Institute for Environmental Quality, Kiev, Ukraine. Water samples were collected at each station, filtered through Whatman GF/F glass filters, and analyzed for chl-*a* and TSS. Chl-*a* was extracted in hot ethanol and its concentration was quantified spectrophotometrically. TSS concentrations were determined gravimetrically.

MODIS and MERIS images acquired up to two days before or after the date of *in situ* data collection were used.

4.2. Satellite Data Processing

The MODIS and MERIS images were atmospherically corrected to convert the at-sensor radiance to surface reflectance values. Four different options were considered for atmospherically correcting MODIS images and two different options for MERIS images.

4.2.1. Atmospheric Correction of MODIS Images

The following four options of atmospheric correction were executed on MODIS images through the software, SeaDAS (SeaWiFS Data Analysis System), developed at the NASA Goddard Space Flight Center, Maryland.

(i) NIR Bands Procedure

This is an iterative procedure (Stumpf et al. 2003) based significantly on the atmospheric correction procedure developed by Gordon and Wang (1994), with a modification that explicitly recognizes scattering from suspended sediments in water in the NIR region. Gordon and Wang's approach assumed zero water-leaving radiance at 748 nm and 869 nm. The radiance recorded by the sensor at these wavelengths, after being corrected for Rayleigh (molecular) scattering, was considered to have entirely come from atmospheric particulate scattering. The at-sensor radiances at 748 nm and 869 nm were used to determine the aerosol type and size parameters and choose the pre-defined aerosol model. Thus, for turbid waters where there is a considerable amount of back-scattering by suspended particles that cause appreciable water-leaving radiance in the NIR region (Moore 1980; Stumpf and Tyler 1988; Stumpf and Pennock 1989; Ruddick et al. 2000; Siegel et al. 2000), Gordon and Wang's approach overestimates the atmospheric particulate scattering. This results in over-correction of atmospheric contribution, thereby yielding negative reflectances at shorter wavelengths.

Stumpf et al (2003) suggested an iterative procedure that takes into account the non-zero water-leaving radiance at 748 nm and 869 nm. The first iteration is essentially the same as Gordon and Wang's procedure. The Rayleigh-corrected at-sensor radiances at 748 nm and 869 nm are input as atmospheric particulate scattering into Gordon and

Wang's model, which corrects the radiances at all wavelengths using radiative transfer equations. The corrected radiance at 667 nm is fed into a semi-analytical bio-optical model that accounts for particulate scattering in water at the NIR region and estimates the water-leaving radiance at 748 nm and 869 nm (Stumpf et al. 2003). The estimated water-leaving radiances at 748 nm and 869 nm are propagated to the top of the atmosphere by correcting for atmospheric transmission. The top of the atmosphere water-leaving radiances at 748 nm and 869 nm are deducted from the Rayleigh-corrected at-sensor radiances at 748 nm and 869 nm, and the result is fed into Gordon and Wang's model for the second iteration. The process is continued iteratively until the successive estimates of the water-leaving radiance (from the bio-optical model) at 748 nm differ by less than 10^{-5} Sr^{-1}. The iterations successively lower the magnitude of at-sensor radiance fed as input into Gordon and Wang's model, thereby diminishing the overestimation of atmospheric particulate scattering and resulting in improved determination of the aerosol type and size parameters. This method significantly reduces the occurrences of negative reflectances in the shorter wavelengths but does not eliminate them completely.

(ii) SWIR Bands Procedure:

This method, developed by Wang and Shi (2005), is essentially the same as Gordon and Wang's (1994) approach except that the Short wave Infrared (SWIR) bands centered at 1240 and 2130 nm are used instead of the NIR bands centered at 748 nm and 869 nm for aerosol model selection. At the SWIR wavelengths, the absorption by water is extremely high so that even turbid productive waters can be safely presumed to have zero reflectance (Wang and Shi 2005). Thus the measured at-sensor radiance at 1240 nm and 2130 nm are considered to be entirely due to atmospheric contribution. In a similar

manner as with Gordon and Wang's model, the atmospheric particulate scattering is extrapolated to shorter wavelengths and the water-leaving radiance is determined for the whole spectral range. Even though the SWIR bands are theoretically better suited than the NIR bands for aerosol model selection, the magnitude of reflectance is much lower at the SWIR wavelengths than at the NIR wavelengths. Hence the SWIR Bands Procedure is more susceptible to detector noise issues. Wang and Shi (2005) originally suggested SWIR bands centered at 1240 nm and 1640 nm. Because of high noise effects in the MODIS 1640 nm band, the band centered at 2130 nm was used. In order to correct for the effect of detector noise, Wang and Shi (2005) vicariously calibrated the SWIR bands using the radiance at the NIR bands. The calibration coefficients were obtained from a linear regression of the MODIS-measured radiance at the SWIR bands with the radiance simulated at the SWIR bands. The MODIS-measured radiance at the NIR bands over an open ocean region (where there is virtually no reflectance from water at the NIR wavelengths) was input into Gordon and Wang's (1994) model to simulate the at-sensor radiance at the SWIR bands.

Though this method circumvents the problem of particulate scattering from turbid water, it is quite susceptible to detector noise due to the very low magnitude of signal at the SWIR wavelengths.

(iii) Wang-Shi Procedure:

This is the same as the SWIR Bands Procedure except that the SWIR bands are vicariously calibrated with a different set of coefficients.

(iv) MUMM Procedure:

MUMM stands for the Management Unit of the North Sea Mathematical Models, a department of the Royal Belgian Institute of Natural Sciences. Ruddick et al. (2000) developed this atmospheric correction procedure. This is essentially a modification of Gordon and Wang's (1994) procedure for turbid waters. For turbid waters, Ruddick et al. (2000) replaced the black-pixel assumption at the NIR wavebands with an assumption of spatial homogeneity of the ratios of aerosol reflectance and water reflectance at 748 nm and 869 nm. For each image, a scatterplot of Rayleigh-corrected radiances at 748 nm and 869 nm is used to determine the ratio of aerosol reflectances at 748 nm and 869 nm. The slope of the relationship between the Rayleigh-corrected reflectances at 748 nm and 869 nm at the lower part of the scatterplot (i.e., at lower magnitudes of Rayleigh-corrected reflectances, which correspond to clear water pixels with minimal water reflectance at 748 nm and 869 nm) gives the ratio of aerosol reflectances at 748 nm and 869 nm. The ratio of water reflectances at 748 nm and 869 nm is set at a default value of 1.945, which was determined based on a marine bio-optical reflectance model (Gordon et al. 1988) and previously published data (Palmer and Williams 1974). Ruddick et al. (2000) tested the sensitivity of the water reflectance ratio to factors such as absorption from other constituents in water, spectral variation of particulate back-scattering, internal reflection of the upwelling radiance field by the sea surface, and second-order scattering in the marine bio-optical reflectance model. They found that the ratio varied by less than 0.8%. The aerosol reflectance and water reflectance ratios are used in radiative transfer equations to deduce the reflectance due to aerosol multiple-scattering at 748 nm and 869 nm, which are then used to calculate the single-scattering aerosol reflectances at 748 nm

and 869 nm. The ratio of the single-scattering aerosol reflectances at 748 nm and 869 nm is used to determine the aerosol type and its particle size distribution. The multiple-scattering aerosol reflectance is extrapolated to the shorter wavelengths and factored out of the Rayleigh-corrected reflectance at each waveband to give final corrected surface reflectances for all the wavebands.

The MUMM procedure presents a theoretically solid way of avoiding the assumption of zero water reflectance in the NIR region. A significant drawback, however, is that the procedure assumes a single aerosol type for the whole image. This can be a significant source of error in images with mixed aerosol types, especially in coastal areas that are adjoined by industrial developments.

The two-band MODIS NIR-red model was applied to the atmospherically corrected surface reflectance data as,

$$\text{Two-Band MODIS NIR-red Model: } \text{Chl-}a \propto \left(R_{667}^{-1} \times R_{748}\right) \tag{4.1}$$

4.2.2. Atmospheric Correction of MERIS Images

MERIS images were obtained from the European Space Agency and processed through BEAM (the Basic ENVISAT and ERS (A)ATSR and MERIS toolbox), which was developed by Brockmann Consult, Germany. Two types of atmospheric correction were considered.

(i) Bright Pixel Atmospheric Correction:

This is a modification of the standard atmospheric correction procedure routinely applied to MERIS images (Moore et al. 1999; Aiken and Moore 2000). This involves classifying the pixels into Case I and Case II water pixels based on the radiance recorded by the sensor at 708 nm. The Case I pixels have zero water-leaving radiance in the NIR

region. For these pixels, the at-sensor radiance recorded at 708 nm is assumed to have been entirely due to atmospheric contribution and these pixels are subjected to the conventional atmospheric correction procedure according to Gordon and Wang (1994). For the Case II pixels, the radiances recorded at three NIR wavebands, centered at 708 nm, 778 nm, and 865 nm, are used in an iterative procedure to isolate the water-leaving radiance and estimate the single-scattering aerosol reflectance. The single-scattering aerosol reflectance is input into an open ocean processing chain (Antoine and Morel 1998) to determine the aerosol type, thickness, and path radiance. The estimated measure of aerosol scattering is then used in the same procedure as Gordon and Wang's (1994) to extrapolate the aerosol scattering at shorter wavelengths and retrieve the water-leaving radiance and subsequently the remote sensing reflectance at all wavelengths.

(ii) Case 2 Regional Processing:

This method is a neural-network-based procedure developed specifically for inland and coastal Case II waters that are very turbid (Doerffer and Schiller 2007; Doerffer and Schiller 2008), where even the Bright Pixel Atmospheric Correction procedure yields negative reflectances, especially in the blue region. It is implemented as a two-step procedure – (i) a forward neural-network for the retrieval of water-leaving radiances and subsequently the remote sensing reflectances from the at-sensor radiances (atmospheric correction) and (ii) a backward neural-network for the retrieval of the inherent optical properties of water and subsequently the concentrations of constituents by inverting the remote sensing reflectances. Both the forward and the backward neural-networks were trained based on radiances simulated by radiative transfer solutions and built to parameterize the relationships between the top-of-atmosphere radiances and the

water-leaving radiances (for the forward model) and between the remote sensing reflectances and the inherent optical properties (for the backward model). The recorded radiances at 12 wavebands (at visible and NIR wavelengths) are used in the neural-network.

The three-band and two-band MERIS NIR-red models were applied to the atmospherically corrected surface reflectance data as,

$$\text{Three-Band MERIS NIR-red Model: } \text{Chl-}a \propto \left(R_{665}^{-1} - R_{708}^{-1}\right) \times R_{753} \qquad (4.2)$$

$$\text{Two-Band MERIS NIR-red Model: } \text{Chl-}a \propto \left(R_{665}^{-1} \times R_{708}\right) \qquad (4.3)$$

Unless specifically stated, the MERIS results shown here are from the Bright Pixel Atmospheric Correction procedure.

4.2.3. Effects of Atmospheric Correction

The wavebands in the NIR-Red model are located close enough to each other that the atmospheric effects can be assumed to be almost uniform at the wavelengths considered. Thus, in principle, the models are not very sensitive to atmospheric effects. However, the water-leaving radiance is very low in the NIR region and the NIR reflectance is a multiplicative term in the models (equations (4.1) – (4.3)). Hence the models are very sensitive to changes in the magnitude of the NIR reflectance. Thus, good atmospheric correction, resulting in accurate retrievals of NIR reflectance, is crucial to the success of the models.

The atmospheric correction procedures differed in how the aerosol reflectance was approximated. As a result, the retrieved reflectances differed in their shape and, to a greater extent, their magnitude (figure 4.1). Consequently, the relationship between the NIR-red model values and chl-*a* concentration also varied widely for reflectances

retrieved through different atmospheric correction procedures for the same set of stations (figure 4.2). Thus it is evident that the accuracy obtained from the NIR-red models depends on the particular atmospheric correction applied to retrieve surface reflectance and any NIR-red algorithm is specific to the particular atmospheric correction procedure employed.

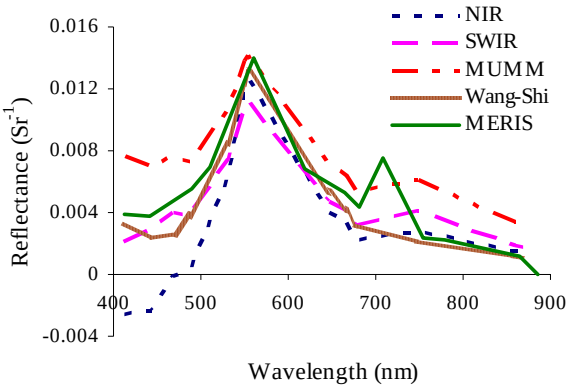

Figure 4. 1. Reflectance spectra for the same station (chl-*a* 39.17 mg m^{-3}) retrieved using different atmospheric correction procedures.

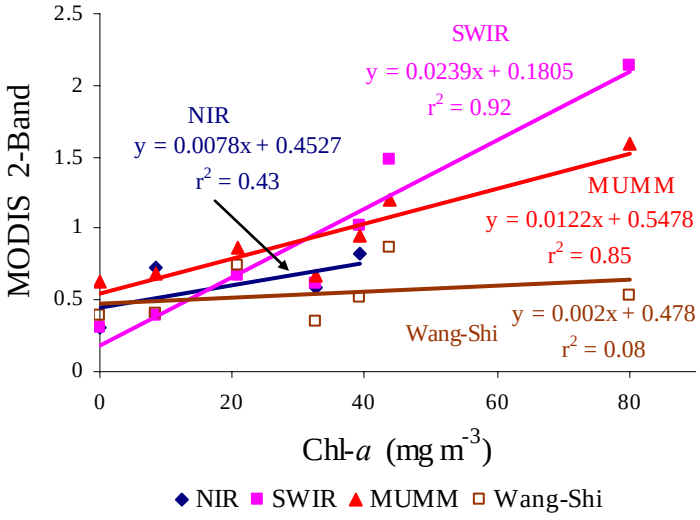

Figure 4. 2. Plot of Chl-*a* concentration versus two-band MODIS NIR-Red model (equation (4.1)) values for different atmospheric correction procedures for MODIS data.

4.3. Correlations between NIR-red Models and Phytoplankton Biophysical Characteristics

4.3.1. Chlorophyll Fluorescence Estimation

Continuous measurements of chl-*a* fluorescence were made from a ship along a transect on the Azov Sea on 17th June 2005. Figure 4.3 shows comparisons between fluorometer readings and the two-band and three-band model values for MERIS data acquired on the same day. The results show that both the two-band and the three-band models are able to explain about 70% of the variation in chl-*a* fluorescence.

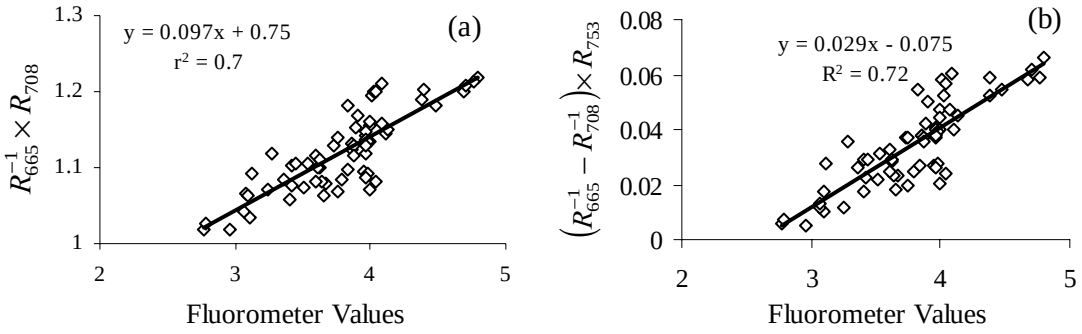

Figure 4. 3. Comparison of fluorometer readings and NIR-Red model values retrieved from MERIS data: (a) two-band MERIS NIR-red model, (b) three-band MERIS NIR-red model.

4.3.2. Phytoplankton Biomass Estimation

Water samples were collected from the Azov Sea on 30th June and 01st July of 2006 and the phytoplankton biomass was analytically measured. Satellite images were acquired between 29th June and 01st July of 2006. Comparisons of phytoplankton biomass with the NIR-Red model values calculated for MODIS and MERIS images are shown in figure 4.4. The slope and offset of the relationship and the coefficient of determination

were different for the different atmospheric correction procedures. The two-band MERIS NIR-red model was able to explain about 97% of the variation in phytoplankton biomass.

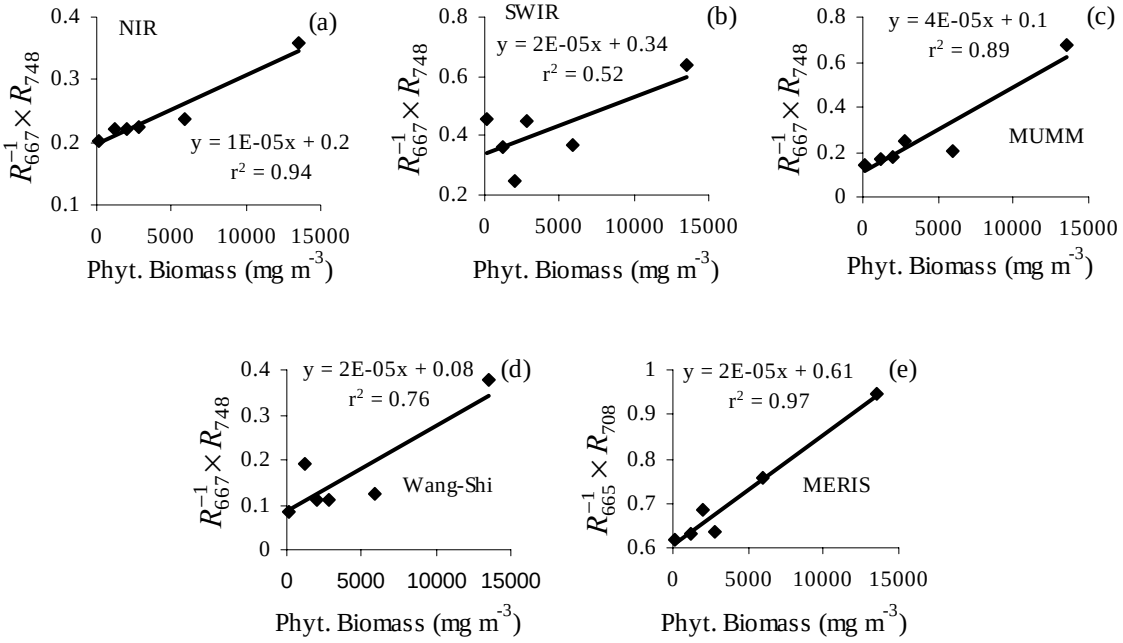

Figure 4. 4. Plots of Phytoplankton biomass versus NIR-Red model values. (a) - (d): two-band MODIS NIR-red model, (e): two-band MERIS NIR-red model.

4.3.3. Chlorophyll-*a* Estimation

The correlation between the NIR-red model (equations (4.1) – (4.3)) values and analytically measured *in situ* chl-*a* concentrations varied in their slope, offset, and coefficient of determination, based on the type of atmospheric correction procedure executed on the satellite images (figure 4.5).

Figures 4.5(a) through 4.5(d) show the results of comparisons for the two-band MODIS NIR-red model (equation 4.1). The *in situ* and satellite data were acquired on the same day (27th Aug 2003) from the Dnieper Estuary. The number of data points in each plot is not the same because not all station pixels were equally retrievable for the different procedures. Among the different atmospheric correction procedures for MODIS

data, in terms of the ability of the model to explain the highest percentage of the variation in chl-*a* concentration, no one procedure stood out consistently better than the rest. However, in general, the model values from the *SWIR Bands Procedure* and the *MUMM Correction* had a closer correlation with chl-*a* concentration than did the model values from the other two procedures.

Also, in general, the results from the MERIS NIR-red models, especially the two-band MERIS NIR-red model, were better than those from the two-band MODIS NIR-red model. This is due to the availability of a spectral channel centered at 708 nm in the MERIS sensor and the higher spatial resolution of MERIS (260 m x 290 m) compared to MODIS (1 km x 1 km). The reflectance at 708 nm well represents the chlorophyll-induced reflectance peak in the NIR region. With increase in chl-*a* concentration, the magnitude of the peak also increases (Gitelson 1992), resulting in a consequent increase in the value of the ratio, R_{708}/R_{665} . Whereas, the reflectance at 748 nm is not affected by chl-*a* absorption as it depends only on scattering by suspended particles and absorption by water. Moreover, the magnitude of the water-leaving radiance at 748 nm is much lower than that at 708 nm due to increased absorption by water at longer wavelengths. Thus, the uncertainties of the atmospheric correction procedure due to low signal-noise ratio are less pronounced at 708 nm than at 748 nm. Furthermore, with 708 nm being closer to λ_1 (665 nm) in the two-band MERIS NIR-red model than 748 nm is to λ_1 (667 nm) in the two-band MODIS NIR-red model, the differential atmospheric effects at the two wavebands in the model are less pronounced with the two-band MERIS NIR-red model than with the two-band MODIS NIR-red model. This makes the two-band MERIS NIR-red model less sensitive to spectrally non-uniform atmospheric effects. Figures

4.5(e) and 4.5(f) show the results from MERIS imagery for data collected from the Azov Sea during the period 17 – 19 June 2008. MERIS image was not available for 27th Aug 2003 from the Dnieper Estuary. As illustrated in the figure, in general, the model values derived from MERIS data were able to account for more than 90% of the variation in chl-*a* concentration, whereas the results from MODIS rarely accounted for more than 60%.

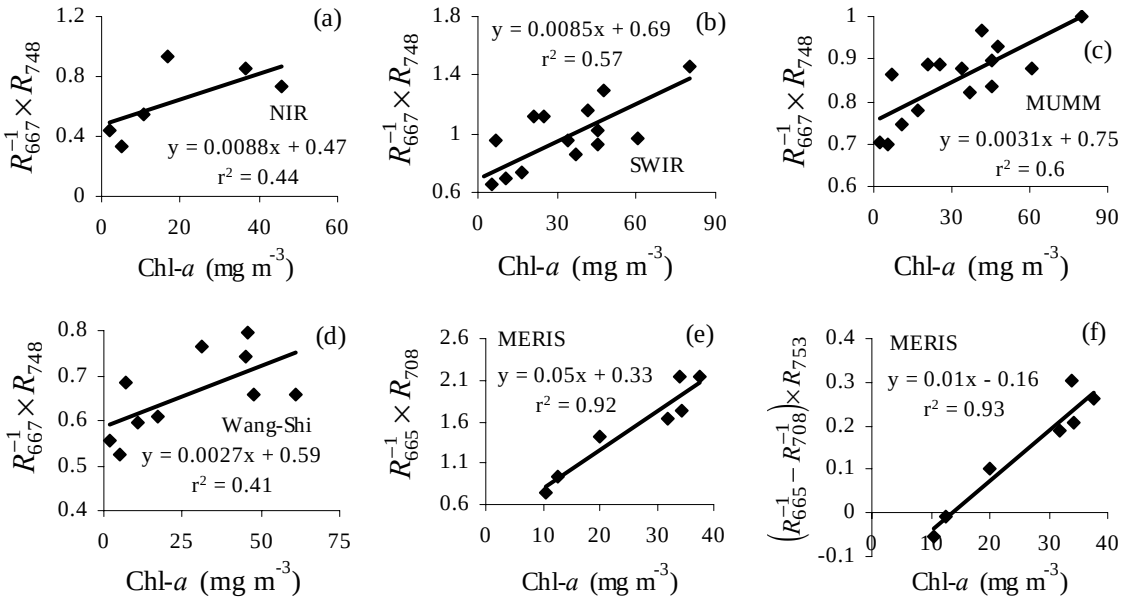

Figure 4. 5. Plots of chl-*a* concentration versus NIR-Red model values. (a) – (d): the results from MODIS data for 27th Aug 2003 from the Dnieper Estuary; (e) and (f): the results from MERIS data for Jun 2008 from the Azov Sea.

4.4. Development of MERIS NIR-red Algorithms for Estimating Chl-*a* Concentration

For reasons described in chapter 2 and in section 4.3.3, the two-band MODIS NIR-red model is less suitable than the MERIS NIR-red models for estimating chl-*a* concentrations, especially at low-to-moderate chl-*a* concentrations (Gitelson et al. 2009). Hence efforts were made to calibrate only the MERIS NIR-red models.

4.4.1. Data

Five data collection campaigns were undertaken (in April, July, September, and October of 2008 and March of 2009) on the Taganrog Bay and the Azov Sea by the crew at the Southern Scientific Centre of the Russian Academy of Sciences, Rostov-on-Don, Russia. Water samples were collected at each station, filtered through Whatman GF/F glass filters, and analyzed for chl-*a* and TSS (Total Suspended Solids). Chl-*a* was extracted in hot ethanol and its concentration was quantified spectrophotometrically. TSS concentrations were determined gravimetrically

MERIS images acquired up to two days before or after the date of *in situ* data acquisition were used in cases where same-day images were not available. For the whole dataset, the average temporal difference between the times of *in situ* and satellite data acquisitions was less than a day. The remote sensing reflectance was retrieved through the Bright Pixel Atmospheric Correction procedure and the Case 2 Regional Processing. After the retrieval of surface reflectances, the three-band (equation (4.2)) and two-band (equation (4.3)) MERIS NIR-red models were applied.

4.4.2. Calibration and Validation of the MERIS NIR-red Algorithms

Of all the stations where *in-situ* data were collected, the stations that satisfied the following criteria were considered for the comparisons:

- the station is at least at a two-pixel length from the shoreline;
- the station is on a cloud/haze–free pixel in an image acquired within 2 days before/after the date of *in-situ* data collection;
- the atmospheric correction procedure did not produce reflectance spectra with negative values beyond 443 nm;

- the reflectance spectrum is not inconsistent in its spectral shape with the observed *in-situ* data.

Outliers of the latter kind, which were very few, were identified by comparison with reflectance spectra from stations with similar chl-*a* concentration (figure 4.6). The reflectance spectra in figure 4.6 correspond to stations with chl-*a* concentrations between 23.3 mg m^{-3} and 26.5 mg m^{-3}. In contrast to the solid-line spectra, the dashed-line spectrum at the bottom has a distinct lack of the typical chl-*a* absorption in the red region (around 665 nm) and the peak reflectance in the NIR region (near 708 nm). Such outliers are deemed to have resulted from any one or a combination of the following factors: (i) within-pixel spatial heterogeneity of chl-*a* distribution, resulting in the point *in-situ* observation being not representative of the satellite pixel, (ii) an actual change in chl-*a* concentration in the water body between the time of *in-situ* data collection and time of the satellite image acquisition, and (iii) erroneous retrieval of the remote sensing reflectance.

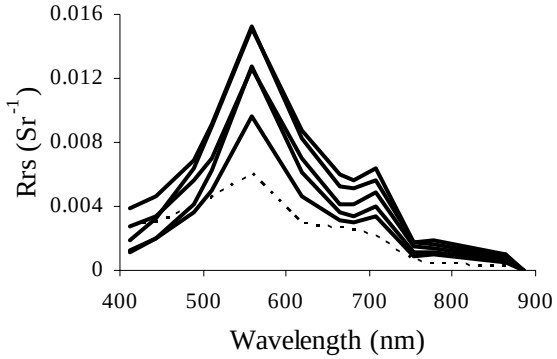

Figure 4. 6. Reflectance spectra from stations with chl-*a* concentrations between 23 and 26 mg m^{-3}. The spectrum shown as a dashed line has a distinct lack of spectral features in the red and NIR regions, in contrast to the rest of the spectra.

Altogether from the five *in-situ* data collection campaigns, there were 18 stations from the 2008 dataset and 8 stations from the 2009 dataset that satisfied the above criteria. The stations from the 2008 dataset were used to establish and calibrate the relationship between the chl-*a* concentrations and the model values, and the stations from the 2009 dataset were used to test the validity of the algorithms. The minimum, maximum, median, and mean *in situ* chl-*a* concentrations of the 18 stations for calibration were 0.63 mg m^{-3}, 65.51 mg m^{-3}, 24.35 mg m^{-3}, and 26.97 mg m^{-3} respectively. The corresponding figures for the 8 stations for validation were, respectively, 18.37 mg m^{-3}, 47.86 mg m^{-3}, 26.44 mg m^{-3}, and 28.56 mg m^{-3}. The TSS concentration ranged from 0.4 g m^{-3} to 27.4 g m^{-3} for the entire dataset.

(i) Bright Pixel Atmospheric Correction:

For the stations chosen for calibration, the three-band and the two-band model values had very close linear relationships with *in-situ* chl-*a* concentrations, with a coefficient of determination (r^2) higher than 0.95 (figure 4.7).

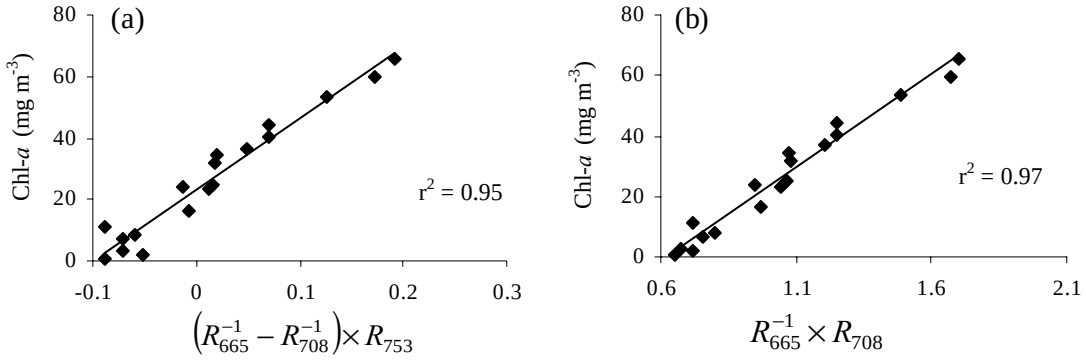

Figure 4. 7. Calibration of (a) the three-band and (b) the two-band MERIS NIR-red models for the *Bright Pixel Atmospheric Correction* procedure.

The calibrated NIR-Red MERIS algorithms were:

Three-band MERIS NIR-red algorithm: $\text{chl-}a = 232.29[\left(R_{665}^{-1} - R_{708}^{-1}\right) \times R_{753}] + 23.174$ (4.4)

Two-band MERIS NIR-red algorithm: $\text{chl-}a = 61.324[R_{665}^{-1} \times R_{708}] - 37.94$

(4.5)

The slope and intercept of both MERIS NIR-red algorithms compared well with the slope and intercept of the relationships derived from *in situ* reflectances collected in 2008 from several lakes in Nebraska, USA (Gitelson et al. 2009) for chl-*a* concentrations in the range similar to that of the calibration data. The slope and intercept of the three-band MERIS NIR-red algorithm (equation (4.4)) were 232.29 and 23.174 mg m^{-3}, respectively, whereas the corresponding figures for the *in situ* three-band algorithm were 207.34 and 22.175 mg m^{-3}, respectively. Similarly, the slope and intercept of the two-band MERIS NIR-red algorithm (equation (4.5)) were 61.324 and -37.94 mg m^{-3}, respectively, whereas the corresponding figures for the *in situ* two-band algorithm were 61.22 and -39.615 mg m^{-3}, respectively.

Further work needs to be done to test the stability of the slope and offset of the relationship between the model values and chl-*a* concentration. The quality of atmospheric correction is bound to have an impact on the magnitude of these parameters. Dall'Olmo et al. (2005) analyzed the propagation of systematic errors due to atmospheric correction in the NIR-Red models and concluded that the models are reasonably resistant to such errors.

The algorithms thus calibrated were used to estimate the chl-*a* concentration at the 8 stations from the 2009 dataset, which was marked for validation. The validation procedure included (a) the estimation of chl-*a* concentrations by applying the calibrated

algorithms (equations (4.5) and (4.6)) to the remote sensing reflectances retrieved for the stations in the validation data set, and (b) the comparison between the estimated chl-*a* concentrations and the *in situ* chl-*a* concentrations. The comparison showed that the chl-*a* concentrations estimated using the calibrated algorithms were remarkably accurate (figure 4.8). The three-band MERIS NIR-red algorithm yielded an RMSE of 5.02 mg m^{-3} (figure 4.8(a)), while the two-band MERIS NIR-red algorithm had an even smaller RMSE of 3.65 mg m^{-3} (figure 4.8(b)).

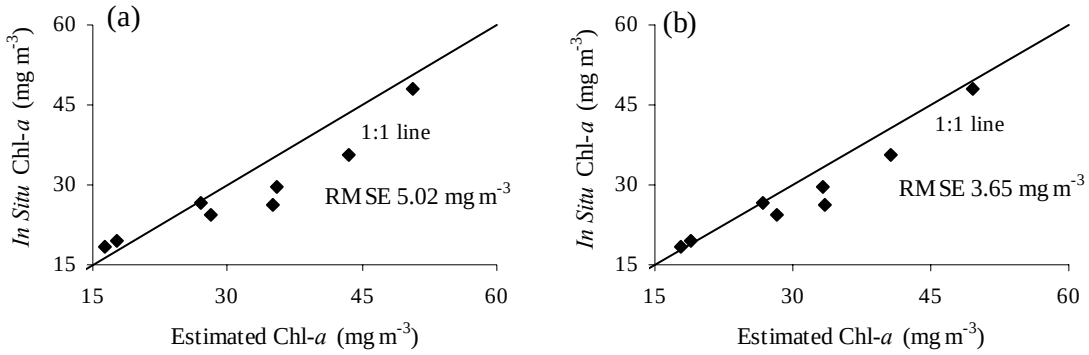

Figure 4. 8. Validation of the MERIS NIR-Red algorithms developed using data taken in 2008: relationships between the chl-*a* concentrations estimated by (a) the three-band and (b) the two-band MERIS NIR-red algorithms for the *Bright Pixel Atmospheric Correction* procedure and the chl-*a* concentrations measured *in situ*.

λ_3 in the three-band MERIS NIR-red model (equation (4.2)) is at a longer wavelength (753 nm) than λ_2 in the two-band MERIS NIR-red model (equation (4.3)). Hence, the three-band MERIS NIR-red model was more sensitive than the two-band MERIS NIR-red model was to uncertainties in the atmospheric correction procedure due to low signal-noise ratio, especially for stations with low chl-*a* concentrations and low magnitudes of reflectance in the NIR region. This, in addition to the reasons described in chapter 2, may explain the looser fit of points with chl-*a* concentration below 10 mg m^{-3}

(figure 4.7(a)) and the slightly higher RMSE for the three-band MERIS NIR-red model. Hence even though both the algorithms yield high accuracies, the two-band MERIS NIR-red algorithm is preferred over the three-band MERIS NIR-red algorithm.

(ii) Case 2 Regional Processing:

The three-band and the two-band MERIS NIR-red model values derived from the *Case 2 Regional Processing* method did not have as close a correlation with *in situ* chl-*a* concentrations as did the model values from the *Bright Pixel Atmospheric Correction* procedure. In this procedure, with increase in chl-*a* concentration, the spectral reflectance features in the red and NIR regions (specifically, the reflectance peak around 700 nm (Gitelson 1992)) were not proportionally increasingly pronounced as much as they should be (see *in situ* reflectance spectra: figure 2 in Dall'Olmo and Gitelson (2005)) and as they were in the reflectance spectra from the *Bright Pixel Atmospheric Correction* procedure (figure 4.9). Thus for both models, the relationship between the *in situ* chl-*a* concentrations and the model values were not uniform for the whole range of chl-*a* concentrations. The relationships were quite close for chl-*a* below 35 mg m^{-3}, with the coefficient of determination as high as 0.9 for both the models. However, the relationships broke and the models lost their sensitivity to chl-*a* above 35 mg m^{-3} (figure 4.10). For this reason, the output from the Case 2 Regional Processing method could not be used for estimating chl-*a* concentrations above 35 mg m^{-3} using the MERIS NIR-red algorithms. Thus no attempt was made to calibrate the MERIS NIR-red models for data processed by the Case 2 Regional Processing method.

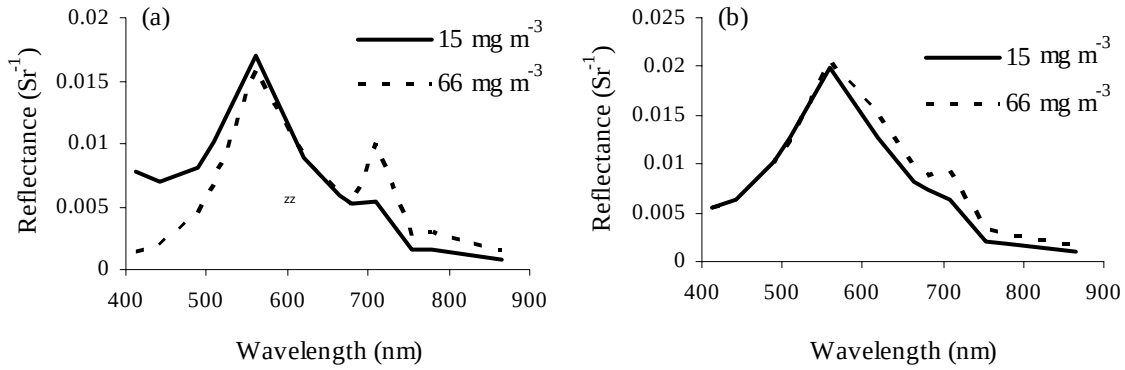

Figure 4. 9. Reflectance spectra of two stations retrieved using (a) the *Bright Pixel Atmospheric Correction* procedure and (b) the *Case 2 Regional Processing*; the spectral features in the red and NIR regions are better pronounced in proportion to increase in chl-*a* concentration in the reflectance spectra from the *Bright Pixel Atmospheric Correction* procedure than those from the *Case 2 Regional Processing* method.

The neural-network procedure is applied as a two-step process – (i) the retrieval of water-leaving radiances from the at-sensor radiances (atmospheric correction) and (ii) the inversion of the water-leaving radiances for the retrieval of the concentrations of the constituents in water. Both these steps have to be independently investigated to identify the reason for the apparent suppression of the spectral features in the red and NIR regions, which renders the procedure as yet unreliable for estimating chl-*a* concentrations over a wide range.

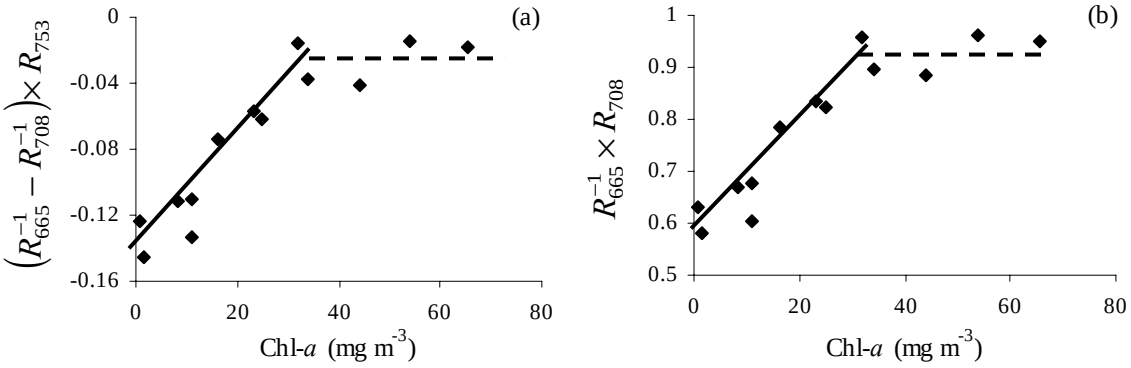

Figure 4. 10. Plots of *in situ* chl-*a* concentrations versus (a) the three-band and (b) the two-band NIR-Red MERIS model values for the *Case 2 Regional Processing* method.

4.4.3. Comparison of the MERIS NIR-red Algorithms with other Standard Algorithms

The results of chl-*a* estimation from the MERIS NIR-red algorithms (equations (4.4) and (4.5)) were compared with the results from a few other commonly used algorithms.

(i) OC4 Algorithm:

OC4 (Ocean Chlorophyll 4-band algorithm) is a standard algorithm (O'Reilly et al. 1998; O'Reilly et al. 2000) that is often used globally for estimating chl-*a* concentration from ocean color data. Its latest version, the OC4v4 algorithm is given by,

$$\text{Chl-}a = 10^{0.366 - 3.067R + 1.93R^2 + 0.649R^3 - 1.532R^4}, \tag{4.6}$$

$$\text{where, } R = \log_{10}\left(\frac{R_{443} > R_{490} > R_{510}}{R_{555}}\right) \tag{4.7}$$

When tuned to the MERIS spectral bands, the corresponding algorithm (OC4E) is (O'Reilly et al. 2000),

$$\text{Chl-}a = 10^{0.368 - 2.814R_E + 1.456R_E^2 + 0.768R_E^3 - 1.292R_E^4}, \tag{4.8}$$

$$\text{where, } R_E = \log_{10}\left(\frac{R_{443} > R_{490} > R_{510}}{R_{560}}\right) \tag{4.9}$$

The accuracies of both the NIR-Red MERIS algorithms were significantly better than what was obtained from the OC4v4 algorithm. For example, when the OC4v4 algorithm was applied to a MODIS image processed by the MUMM atmospheric correction procedure for the March 2009 dataset, the coefficient of determination of the relationship between the estimated and measured chl-*a* concentrations was as low as 0.11, with an RMSE of 19.89 mg m^{-3}. Processing the MODIS data through the other available

atmospheric correction procedures did not yield better results. For the corresponding dataset, the two-band MERIS NIR-red algorithm yielded an RMSE of 3.65 mg m^{-3}, and the three-band MERIS NIR-red algorithm yielded an RMSE of 5.02 mg m^{-3}.

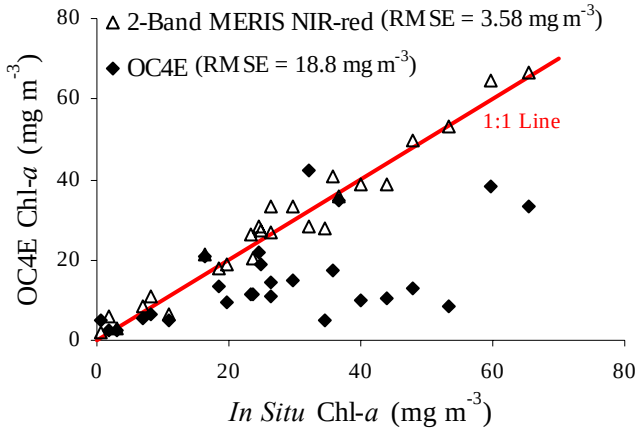

Figure 4. 11. Plot of *in situ* chl-*a* concentration versus chl-*a* concentration estimated by the two-band MERIS NIR-red algorithm and the OC4E algorithm.

The OC4E algorithm, when applied to the MERIS images for the entire dataset that was used to calibrate and validate the MERIS NIR-red algorithms, showed poor correlation with the *in situ* chl-*a* concentrations (figure 4.11), with an RMSE of 18.8 mg m^{-3}. For the same dataset, the two-band MERIS NIR-red algorithm had an RMSE of 3.58 mg m^{-3} and the three-band MERIS NIR-red algorithm had an RMSE of 4.54 mg m^{-3}.

(ii) Gons' Algorithm:

Gons proposed an algorithm that uses reflectances at three MERIS spectral channels centered at 708 nm, 665 nm, and 778 nm to estimate chl-*a* concentration (Gons 1999; Gons et al. 2002; Gons et al. 2005; Gons et al. 2008). The algorithm takes advantage of the maximal absorption by chl-*a* in the red region and the reflectance peak in the NIR region. The reflectance at 778 nm is used to approximate the effect of back-scattering by suspended particles in water. The algorithm is given by,

$$\text{Chl-}a = \left\{\left(R_{708}/R_{665}\right)\left(0.7 + b_b\right) - 0.4 - b_b^{1.06}\right\}/0.016, \quad (4.10)$$

$$\text{where, } b_b = 1.61R_{778}/\left(0.082 - 0.6R_{778}\right) \quad (4.11)$$

The chl-*a* concentrations estimated using Gons' algorithm were very closely correlated to the two-band MERIS NIR-red ratio values (figure 4.12). This indicates that the ratio R_{708}/R_{665} dominates Gons' algorithm and that the contribution by the back-scattering term (b_b) is rather insignificant. Moreover, the reflectance at 778 nm is prone to uncertainties due to the very low magnitude of reflectance from water in the NIR region. Thus the two-band MERIS NIR-red model is more reliable than Gons' algorithm. When applied to the entire dataset that was used to calibrate and validate the MERIS NIR-red algorithms, Gons' algorithm had an RMSE of 6.88 mg m^{-3}, compared to 3.58 mg m^{-3} for the two-band MERIS NIR-red algorithm and 4.54 mg m^{-3} for the three-band MERIS NIR-red algorithm (figure 4.13).

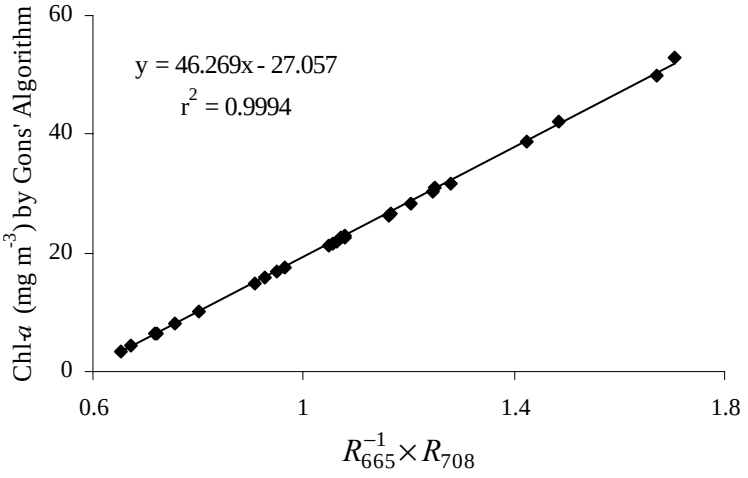

Figure 4. 12. Plot of two-band MERIS NIR-red ratio values versus chl-*a* concentration estimated by Gons' algorithm.

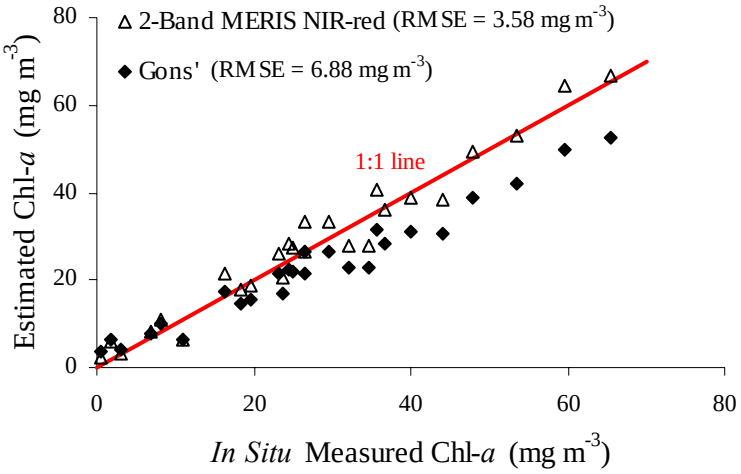

Figure 4. 13. Plot of *in situ* measured chl-a concentration versus chl-a concentration estimated by the two-band MERIS NIR-red algorithm and Gons' algorithm.

(iii) MERIS *algal_2* Algorithm:

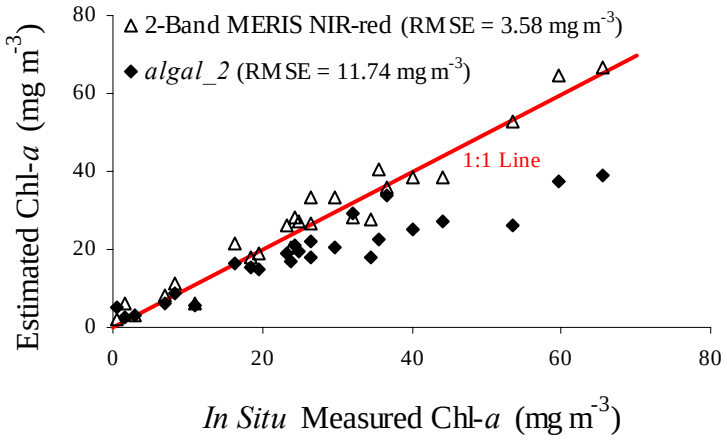

Figure 4. 14. Plot of *in situ* measured chl-*a* concentration versus chl-*a* concentration estimated by the two-band MERIS NIR-red algorithm and the MERIS *algal_2* algorithm.

The standard procedure for processing MERIS data (with Bright Pixel Atmospheric Correction procedure for turbid pixels) includes a neural-network-based approach for estimating chl-*a* concentration from reflectance values. The chl-*a* product is named *algal_2*. When compared with *in situ* data collected from Azov Sea in 2008 and

2009 (figure 4.14), the *algal_2* estimates had an RMSE of 11.74 mg m^{-3}, which is worse than that of the two-band (RMSE 3.58 mg m^{-3}) and three-band (RMSE 4.54 mg m^{-3}) MERIS NIR-red algorithms.

(iii) MERIS Case 2 Chl-*a* Neural-Network Algorithm:

The Case 2 Regional Processing method for MERIS images involves a two-step neural-network procedure, which uses the at-sensor radiances at 12 wavebands (at visible and NIR wavelengths) to calculate the surface reflectance values at each wavelength and subsequently biophysical products such as chl-*a* concentration. Based on the relationships obtained between the measured radiances and the training dataset, the chl-*a* concentration is estimated by the formula,

$$\text{Chl-conc (mg m}^{-3}) = 21 \times \text{a\_pig}^{1.04}, \tag{4.12}$$

where, a_pig is the phytoplankton pigment absorption at 443 nm.

While analyzing data from multiple MERIS images, it was found that the two-band MERIS NIR-Red model values (equation 4.3) had a consistently close correlation with chl-*a* concentrations estimated by the neural-network-based algorithm. The slope and offset of the relationship remained remarkably consistent for data from multiple images from the Chesapeake Bay, the Delaware Bay and the Azov Sea (figure 4.15). The Chesapeake Bay dataset contained a total of 318 data points from 10 different images; the Delaware Bay dataset contained 136 data points from 7 different images; the Azov Sea dataset contained 345 data points from 4 different images. This remarkably tight and consistently close relationship implies that the reflectances at 665 nm and 708 nm heavily influence the neural-network model and the neural-network model that takes into account

the radiances at 12 wavebands converges closely to the two-band ratio, R_{708}/R_{665}. Further investigation is needed to understand the reason for this close relationship.

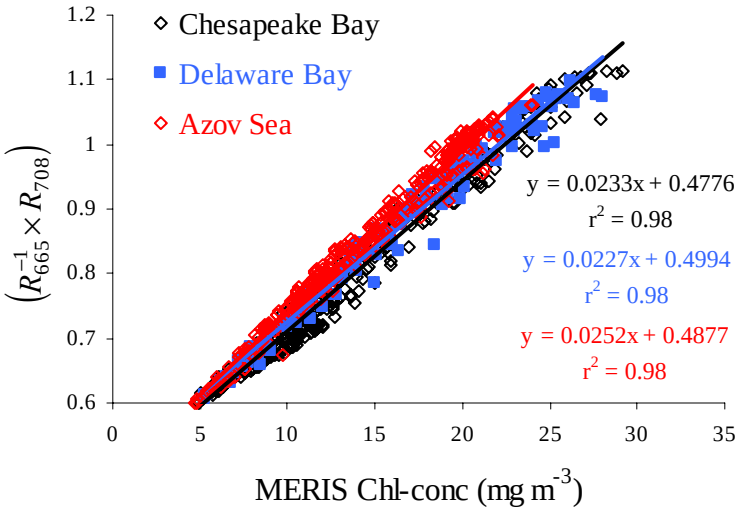

Figure 4. 15. Comparison between chl-*a* concentrations estimated by the Case 2 Regional Processing procedure and the two-band MERIS NIR-red values.

In spite of the close correlation with two-band MERIS NIR-red model values, the MERIS chl-conc values were much lower in magnitude when compared to actual chl-*a* concentrations measured *in situ*. This severe underestimation is due to the strong suppression of chl-*a*-related spectral features in the reflectance spectrum from the Case 2 Regional Processing method (see section 4.4.2(ii)). When MERIS chl-conc values were compared with chl-*a* concentrations measured *in situ* on the Azov Sea in 2008, the RMSE was 16.24 mg m^{-3} (figure 4.16).

The results indicate that the MERIS NIR-red algorithms, especially the two-band MERIS NIR-red algorithm, compare favorably with other standard algorithms for estimating chl-*a* concentration from satellite data. The two-band MERIS NIR-red algorithm is simple in its formulation, less susceptible to spectrally dependent

atmospheric effects, takes full advantage of the absorption trough in the red region and the reflectance peak in the NIR region, and has proven suitable for a wide range of chl-*a* concentrations from inland, estuarine, and coastal turbid productive waters with a wide range of biophysical characteristics.

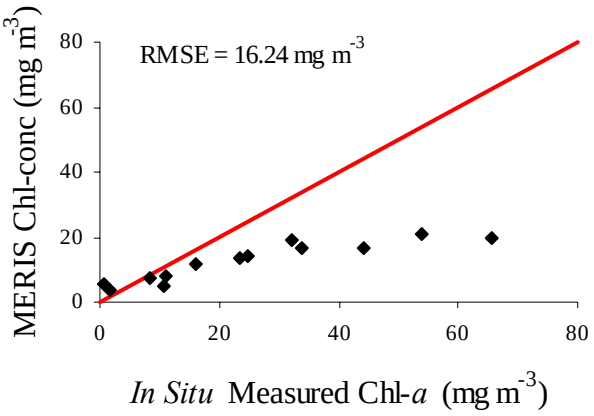

Figure 4. 16. Plot of *in situ* chl-*a* concentration versus chl-*a* concentration estimated by the MERIS Case 2 Regional Processing method.

4.5. Limitations and Challenges in Developing Satellite Algorithms

The results presented here illustrate the high potential of the three-band and the two-band NIR-Red models to accurately estimate chl-*a* concentration in turbid productive waters using MERIS data. It has been already shown that the 708 nm MERIS band can be used for the detection of phytoplankton bloom (Gower et al. 2005). However, to the best of my knowledge, this is the first time that the MERIS NIR-Red models have been successfully calibrated and validated to quantitatively estimate chl-*a* concentration using satellite data. Nevertheless, challenges still remain in calibrating the models for their universal application to satellite data (Moses et al. 2009a). The MERIS NIR-red algorithms were developed and validated with a rather small dataset (18 stations for calibration and 8 stations for validation). The algorithms need to be tested using a larger

set of data from water bodies with a wider variability of constituent composition and from different geographic locations. Some of the limitations and challenges involved in developing such a universal algorithm are discussed here.

4.5.1. Atmospheric Correction

A successful correction for atmospheric effects on satellite data and an accurate retrieval of surface reflectance are crucial to the success of the NIR/Red model. The slope and offset of the relationship between chl-*a* concentration and the NIR-red model values are affected by atmospheric effects on the satellite images. This is pronouncedly seen in multi-temporal datasets in which the atmospheric effects are not uniform on all the images. A reliable atmospheric correction procedure that is able to uniformly correct the non-uniform atmospheric effects across multi-temporal data from multiple geographic locations is necessary prior to applying the NIR-red algorithms universally.

The NIR Bands Procedure, even though it is an improvement over Gordon and Wang's (1994) atmospheric correction model, still overestimates the aerosol contribution, resulting in severe underestimation of water-leaving radiance (yielding negative values) in turbid waters. This results in lower number of retrievable pixels per image, which is a significant problem when attempting to calibrate the NIR-red models by comparing with *in situ* data. Procedures that rely on SWIR bands for aerosol model selection should, in theory, work reasonably well because even turbid waters are quite dark at the SWIR region. However, the higher level of detector noise at SWIR (and the consequent lower signal-to-noise ratio) significantly reduces the advantage gained by using the SWIR bands for aerosol model selection. The MUMM Correction, which was developed to prevent negative reflectances at the shorter wavelengths, often overestimated surface

reflectances. The assumption of a single aerosol type over the whole image may prove costly in narrow water bodies that are adjoined by urban and industrial developments.

Figure 4.17 shows reflectances retrieved through the NIR Bands Procedure from the same water body for very similar values of chl-*a* concentration on three different days. Granted that the variations in the concentration of suspended particles can result in differences in the magnitude of reflectance, a consistently effective atmospheric correction procedure should still yield reflectances that are similar in shape (especially, the spectral features due to chl-*a* absorption in the red and the reflectance peak in the NIR region). The significant differences in the shape and magnitude of the retrieved reflectances (especially, the chl-*a* absorption in the red and the reflectance peak in the NIR region) mean that the NIR-Red model values will be very different for these data points with very similar chl-*a* concentrations.

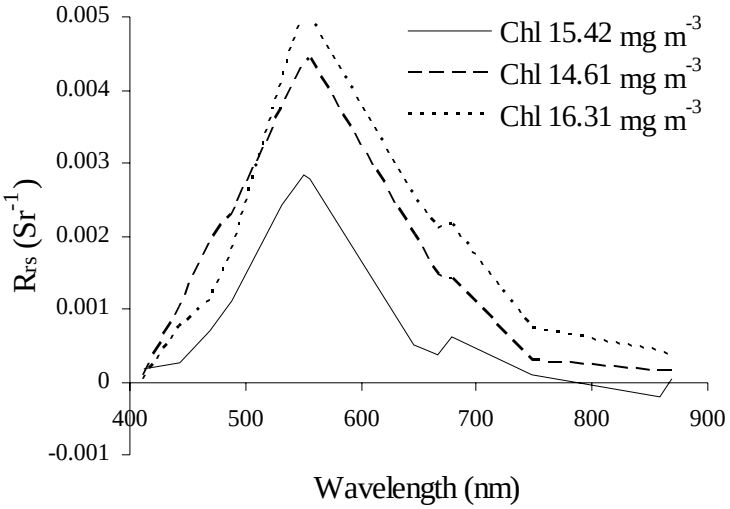

Figure 4. 17. Reflectance spectra retrieved through the NIR Bands Procedure from MODIS data from different dates for stations with similar chl-*a* concentrations.

Judging by the shape of the retrieved reflectance spectra, particularly the spectral features at the red and NIR wavebands caused by the presence of chl-*a* in water, the

Bright Pixel Atmospheric Correction procedure implemented in the standard processing of MERIS data looks good. However, inconsistencies still exist and the procedure often yields negative reflectances, especially for very turbid waters. The atmospheric correction procedure implemented in the Case 2 Regional Processing scheme does a better job of preventing negative reflectances. However, it was found in several instances that the chl-*a*-induced spectral features in the red and NIR wavebands were less pronounced in the output from the *Case 2 Regional Processing* compared to the output from the Bright Pixel Atmospheric Correction (Moses et al. 2009b).

For the purpose of developing a reliable universal NIR-red algorithm, the burden of effective atmospheric correction is not necessarily in yielding absolutely accurate surface reflectance values at all wavelengths, which can be validated by *in situ* measured reflectances. But the non-uniform atmospheric effects on images acquired on different dates from different geographic locations need to be uniformly corrected such that even if the atmospheric effects are not completely removed, their residual effects are uniform across multiple datasets. For the data analyzed for this research, the Bright Pixel Atmospheric Correction procedure has given the most consistent and reliable results. Nevertheless, the images used in this research were acquired over the Taganrog Bay and the Azov Sea, and the procedure needs to be tested for data from other geographic locations with variations in the type and quantity of aerosol loading. *In situ* reflectances measured at the time of satellite image acquisition will help analyze the consistency of atmospheric correction procedures and their effect on the performance of the NIR-red models.

4.5.2. Temporal Variation of Water Quality

A satellite captures its entire swath within a matter of a few seconds whereas it takes several hours to collect *in situ* data. With the inland, estuarine, and coastal waters being quite dynamic, it is conceivable that the water might have undergone appreciable changes in its biophysical and optical characteristics during these few hours. In our studies, differences in chl-*a* concentration of up to a factor of two have been observed within a matter of a few hours. Thus it is important that the temporal variations in the concentrations of optically active constituents such as chl-*a*, TSS, inorganic suspended matter and colored dissolved organic matter be accounted for. This problem is magnified when there is no cloud-free satellite image available for the date of *in situ* data collection and one has to use the image acquired a day or two before/after.

With the *in situ* stations spread quite far from each other, considering the satellite pixel dimension and the necessity to have stations separated by at least two pixel lengths, it has been rather difficult to collect *in situ* data using a single vessel at more than 10 – 12 stations within a time frame of a few hours surrounding the satellite overpass. As stated above, the biophysical and optical characteristics at some of these stations might be different at the time of measurement from what they were at the time of satellite overpass. Furthermore, some of these stations might happen to fall under cloud cover or haze. Thus the number of stations available for comparison with same-day images is quite few, thereby making it difficult to develop reliable calibration equations for the model.

The effect of temporal variability is not uniform for all water bodies but is rather case-specific. As such, as indicated in some of our results, there have been cases where a

temporal difference up to two days did not adversely effect the estimation of chl-*a* concentration due to the stable biophysical condition of the water body. Nevertheless, it is still essential to account for the temporal variations in water quality between the time of *in situ* data collection and the time of satellite image acquisition when attempting to calibrate or validate chl-*a* algorithms.

4.5.3. Within-Pixel Spatial Heterogeneity

Often, the spatial heterogeneity in the water body might be such that the point *in situ* station may not be truly representative of the satellite pixel area (260 m x 290 m for MERIS and 1 km x 1 km for MODIS) surrounding the station. In analyzing fluorescence measurements taken continuously along a transect on the Azov Sea in June 2005, significant variations were found in fluorescence values within every 300 m and 1 km lengths along the transect (figure 4.18). When the water within each satellite pixel is not truly homogeneous, it becomes difficult to confidently and reliably compare the satellite-derived values to point *in situ* observations.

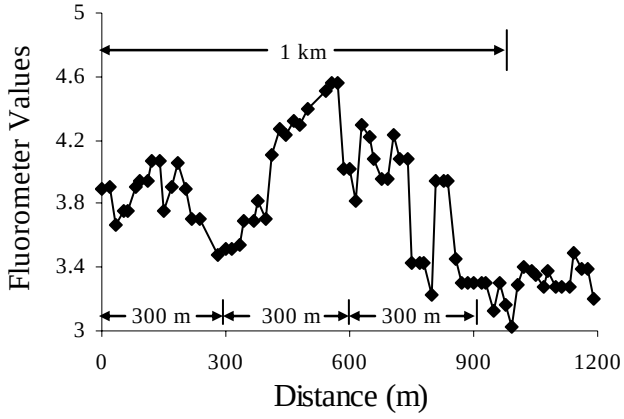

Figure 4. 18. Fluorescence measurements taken continuously along a transect on the Azov Sea plotted against the distance from the starting point.

4.5.4. Need for Modified *In situ* Data Collection Strategy

The significance of the effects of the factors mentioned above and the difficulty in isolating them necessitate the development of *in situ* data collection techniques that help understand and account for these factors. In order to reliably assess the accuracy of atmospheric correction procedures and its effect on the performance of the NIR-red models, it is necessary to have actual measurements of water-leaving radiance collected *in situ* at the time of satellite overpass. Within-pixel spatial heterogeneity and temporal variation have to be accounted for by taking multiple measurements around each station so as to characterize the spatial variation within the satellite pixel area around the station and repeated measurements (at least twice, covering the length of time elapsed between the satellite overpass and the *in situ* data collection) at each station to characterize the temporal variation. If these factors are not accounted for, they present inherent hurdles to the development of reliable regression equations to calibrate the NIR-Red models. Of course, the rigor and the extent to which the *in situ* data collection procedures need to be adapted depend on the particular conditions at the water body.

4.6. Conclusion

The NIR-red models were applied to MODIS and MERIS data acquired over different water bodies and processed through different atmospheric correction procedures. The NIR-red models were closely correlated to phytoplankton biophysical characteristics. The MERIS NIR-red models with the Bright Pixel Atmospheric Correction, especially the two-band MERIS NIR-red model, were more reliable and accurate than the MODIS NIR-red model. Three-band and two-band MERIS NIR-red algorithms were developed, tested, and shown to compare favorably with other standard

chl-*a* algorithms. Nevertheless, the MERIS NIR-red algorithms need to be tested using a larger dataset before being recommended for universal application. The limitations and challenges involved in developing such a universal algorithm have been described. The primary factors are: (i) atmospheric correction of satellite images, (ii) temporal variation of water quality, and (iii) within-pixel spatial heterogeneity. Provided that these limiting factors can be effectively accounted for, robustly calibrated algorithms can be developed for applying the NIR-Red models to satellite data for real-time quantitative measures of chl-*a* concentration, which will greatly benefit scientists and natural resource managers in making informed decisions on managing the inland, coastal, and estuarine ecosystems.

Chapter 5. Summary and Future Work

5.1. Summary of Results

The objective of this research was to explore the feasibility of developing a spectral algorithm based on reflectances in the red and NIR wavelengths for estimating chl-*a* concentration in turbid and productive inland, estuarine, and coastal waters using satellite data. Three-band and two-band NIR-red models were formulated with wavebands that matched the spectral channels of MERIS and MODIS satellites. When applied to multiple datasets from lakes in Nebraska, Chesapeake Bay, and Lake Kinneret in Israel, the NIR-red models had a close and steady correlation with chl-*a* concentration. For reasons described in chapter 2, the two-band MODIS NIR-red model was unreliable for estimating low-to-moderate chl-*a* concentrations and the two-band MERIS NIR-red model was more consistent, accurate, and reliable than the three-band MERIS NIR-red model. The results from the close-range data established the ability of the NIR-red models to account for biophysical variability in water and accurately estimate chl-*a* concentration, without the need to re-parameterize the algorithms for each different water body.

The two-band MERIS NIR-red model was applied to five images acquired by the airborne sensor AISA over lakes in Nebraska. The model had very close relationships with *in situ* chl-*a* concentration for each of the images. The slope and offset of the relationship varied from image to image due to non-uniform atmospheric effects on the five days of image acquisition. By judicious relative adjustment of input atmospheric parameters based on apparent atmospheric particulate scattering, the five AISA images were relatively adjusted for atmospheric effects using the atmospheric correction

program, FLAASH. The relative atmospheric adjustment resulted in conformity of the slope and offset of the relationships between the two-band MERIS NIR-red model values and chl-*a* concentrations. Nevertheless, since there were no actual measurements of atmospheric parameters on those five days to substantiate the absolute values of the parameters that were fed as input to the atmospheric correction program, the uniform slope and offset obtained could not be used to calibrate the two-band MERIS NIR-red model. With their high spatial resolution and adjustability of spectral characteristics, aircraft sensors offer tremendous flexibility. Aircraft missions can be planned to effectively overcome the issues of within-pixel spatial heterogeneity in water and temporal variation of water quality between the times of *in situ* data collection and image acquisition.

The non-uniform atmospheric effects in multi-temporal images pose the biggest hurdle to calibrating the model for aircraft data. *In situ* measurements of aerosol optical thickness need to be taken at the time of image acquisition using a sun photometer so that the input parameters for atmospheric correction could be correctly supplied. If the atmospheric correction program is reliable and consistent, feeding input parameters based on actual measurements of aerosol optical thickness should result in properly atmospherically corrected output that lend to uniform relationships between the model values and chl-*a* concentrations for multi-temporal data, provided other issues such as the quality and reliability of the spectral data from the airborne sensor are sufficiently dealt with. Such a uniform slope and offset of the relationship between model values and chl-*a* concentrations, derived from multi-temporal images taken in different atmospheric conditions, can be used to calibrate the two-band MERIS NIR-red model. However, such

an algorithm will be specific to the sensor (AISA) and the atmospheric correction program (e.g., FLAASH). An independent assessment of the spectral quality of AISA data and the quality of FLAASH atmospheric correction (by comparison with *in situ* measured radiance data) and their effect on the model values need to be done before an universal algorithm can be developed for estimating chl-*a* concentration using data from other airborne sensors.

When applied to data from MODIS and MERIS, the NIR-red models had close correlations with phytoplankton biophysical characteristics such as chlorophyll fluorescence, phytoplankton biomass and chl-*a* concentration. The problem of atmospheric correction remains a major hurdle to developing algorithms for routinely estimating chl-*a* concentration from satellite data. Three-band and two-band MERIS NIR-red algorithms were developed and successfully tested using MERIS images acquired over the Taganrog Bay and Azov Sea, Russia, and processed by the Bright Pixel Atmospheric Correction procedure. Both algorithms were able to explain more than 90% of variation in chl-*a* concentration, with the two-band MERIS NIR-red algorithm performing slightly better, for reasons described in chapters 2 and 4. The accuracy and reliability of the MERIS NIR-red algorithms, especially the two-band MERIS NIR-red algorithm, promise a great potential for universal application to satellite data routinely acquired over turbid and productive waters around the globe. Nevertheless, further needs to be done in order to establish such a universal algorithm. This will be the focus of future work.

5.2. Towards a Universal NIR-red Algorithm

The results shown in Chapter 2 illustrate that there is no need to re-parameterize the MERIS NIR-red algorithms for each different water body. The slopes and intercepts of the three-band and two-band MERIS NIR-red algorithms derived from MERIS satellite data (equations (4.4) and (4.5)) were similar to the corresponding figures for the two-band and three-band MERIS NIR-red algorithms derived from the 2008 Nebraska lakes data (see section 4.4.2(i)). When the two-band MERIS NIR-red algorithm developed using the 2008 Nebraska lakes data (reflectance spectra measured using field spectrometers) were applied to MERIS data acquired over the Azov Sea in 2008 and 2009, the estimated chl-*a* concentrations closely matched the *in situ* measured chl-*a* concentrations, with a very low RMSE of 3.64 mg m^{-3} (figure 5.1). This remarkable result illustrates the insensitivity of the algorithm to the differences in remote sensor and the type of processing and strongly presents the case for the universal applicability of the two-band MERIS NIR-red algorithm. This is further illustrated in figure 5.2, which shows plots of *in situ* measured chl-*a* concentration versus chl-*a* concentrations estimated by the two-band MERIS NIR-red algorithm developed using the 2008 Nebraska lakes data for Lake Kinneret, Chesapeake Bay, Azov Sea, and Nebraska lakes (see also table 5.1). The algorithm is remarkably consistent and highly accurate for data from different waters and different remote sensors (field spectrometers and satellite sensors).

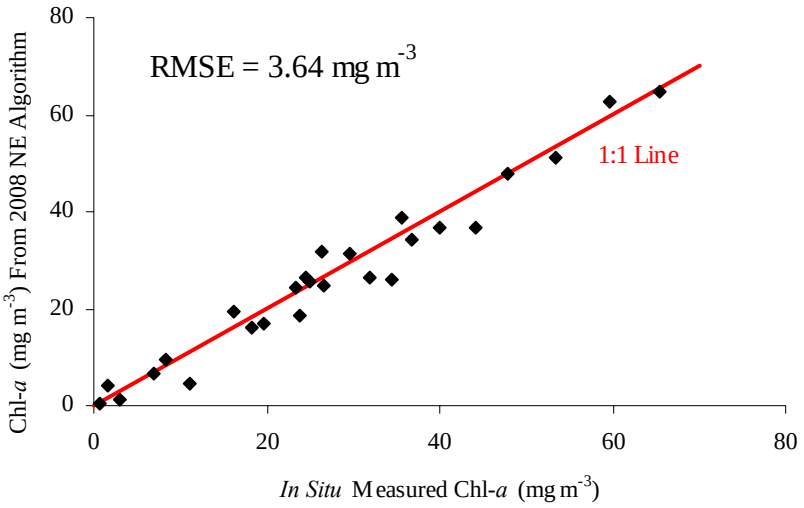

Figure 5. 1. Plot of *in situ* measured chl-*a* concentration in Azov Sea versus chl-*a* concentration estimated from MERIS data using the two-band MERIS NIR-red algorithm developed using the 2008 Nebraska lakes data.

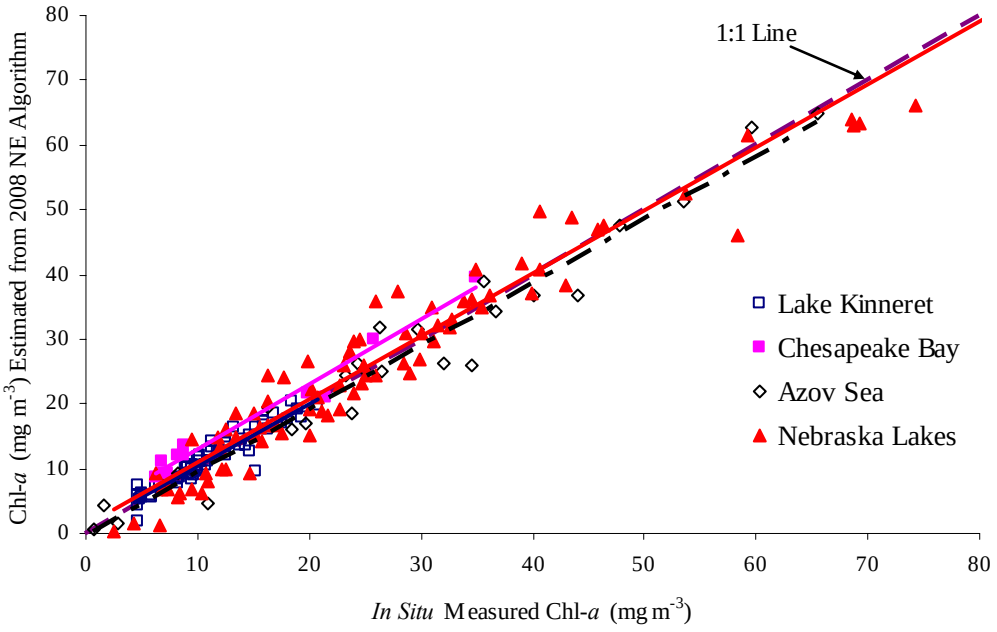

Figure 5. 2. Plots of *in situ* measured chl-a concentration versus chl-a concentration estimated by the two-band MERIS NIR-red algorithm developed using the 2008 Nebraska lakes data for Lake Kinneret, Chesapeake Bay, Azov Sea, and Nebraska lakes.

Water Body	Number of Stations	Chl-*a* Concentration (mg m^{-3})		RMSE (mg m^{-3})	Coefficient of Variation of RMSE
		Min.	Max.		
Lake Kinneret	58	4.6	20.75	1.46	0.13
Chesapeake Bay	11	6.2	34.89	3.42	0.24
Azov Sea	26	0.63	65.51	3.64	0.13
Nebraska lakes	83	2.56	103.4	4.08	0.15

Table 5. 1. Accuracy statistics for the estimation of chl-*a* concentration using the two-band MERIS NIR-red algorithm developed based on the 2008 Nebraska lakes data.

5.3. Suggestions for Future work

Work in the future towards further establishing a universal NIR-red algorithm will revolve around the following three issues:

5.3.1. A broader test of the sensitivity of the calibrated NIR-red algorithms to variations in biophysical characteristics of water

The results shown in chapter 2 demonstrate the ability of the NIR-red models, particularly the two-band MERIS NIR-red model, to account for biophysical variations in water, thereby establishing their potential for universal applicability. However, the NIR-red models need to be further tested for waters with higher concentrations of inorganic suspended solids, wider variation in composition of optically-active constituents and from different geographic locations. When applying the models to data from different campaigns, diligent care has to be taken to ensure that the techniques for measuring *in situ* reflectance data and chl-*a* concentrations remain consistent. The upwelling radiance measurements should be taken just below the water surface. Above-water measurements are very susceptible to the effects of random specular reflection from the water surface, especially in windy and choppy conditions.

5.3.2. Further tests of the sensitivity of the NIR-red algorithms to the type of sensor and the type and quality of atmospheric correction procedure

Uncertainties due to the quality of spectral data and the quality of atmospheric correction can affect the accuracy yielded by the NIR-red algorithms. The results obtained in applying the two-band MERIS NIR-red algorithm developed from the 2008 Nebraska lakes data to the data acquired by MERIS over the Azov Sea illustrated the insensitivity of the algorithm to the type of sensor and the effect of atmospheric correction. Nevertheless, it is essential to further test the sensitivity of the algorithms to these factors by applying the algorithms to data acquired by a few different sensors such as AISA, CASI (Compact Airborne Spectrographic Imager), and PHILLS (Portable Hyperspectral Imager for Low Light Spectroscopy), and corrected by different atmospheric correction procedures such as FLAASH and TAFKAA (The Algorithm Formerly Known As ATREM).

5.3.3. Tests to see if the NIR-red models can be tuned with different wavebands than the MERIS wavebands to yield better results

This research resulted in calibrated three-band and two-band MERIS NIR-red algorithms. Nevertheless, the MERIS spectral channels may not be the most optimal wavebands for the NIR-red models. For instance, for low-to-moderate chl-*a* concentrations, the reflectance peak occurs at a shorter wavelength than 708 nm (Gitelson 1992). Moreover, since the spectral channel centered at 753 nm is quite prone to uncertainties arising from very low magnitudes of water-reflectance (which magnifies the effect of detector noise and the effect on the three-band NIR-red model due to random variations in particulate scattering), a spectral channel in the 720 – 740 nm region might

be preferable for the three-band NIR-red model. The flexibility and continuous spectral coverage offered by aircraft sensors provide a platform to test and choose the most optimal wavebands for the NIR-red models. If the NIR-red models give consistently better results for a particular set of wavebands that are different from the MERIS wavebands, then these wavebands will be strongly recommended for consideration when designing the next space-borne ocean color sensor.

References

Abreu, L. W. and Anderson, G. P. (1996). The MODTRAN 2/3 Report and LOWTRAN 7 Model, ONTAR Corporation for PL/GPOS.

Acharya, P. K., Berk, A., Anderson, G. P., Larsen, N. F., Tsay, S. and Stamnes, K. H. (1999). MODTRAN4: Multiple Scattering and Bi-Directional Reflectance Distribution Function (BRDF) Upgrades to MODTRAN. In M. L. Allen, Ed. Proceedings of SPIE Proc., Optical Spectroscopic Techniques and Instrumentation for Atmospheric and Space Research III, **3756**, pp. 354-362.

Adler-Golden, S. M., Matthew, M. W., Bernstein, L. S., Levine, R. Y., Berk, A., Richtsmeier, S. C., Acharya, P. K., Anderson, G. P., Felde, G., Gardner, J., Hoke, M., Jeong, L. S., Pukall, B., Ratkowski, A. and Burke, H. H. (1999). Atmospheric Correction for Shortwave Spectral Imagery Based on MODTRAN4. In SPIE Proc. Imaging Spectrometry, **3753**, pp. 61 - 69.

Aiken, J. and Moore, G. (2000) ATBD Case 2 s bright pixel atmospheric correction. *PO-TN-MEL-GS-0005*, (14pp), Center for Coastal & Marine Sciences, Plymouth Marine Laboratory, U.K.

Andre, J. M. and Morel, A. (1991). "Atmospheric Corrections and Interpretation of Marine Radiances in CZCS Imagery, Revisited." *Oceanologica Acta*, **14**(1): 3-22.

Antoine, D. and Morel, A. (1998). "Relative importance of multiple scattering by air molecules and aerosols in forming the atmospheric path radiance in the visible and near-infrared parts of the spectrum." *Applied Optics*, **37**(12): 2245-2259.

Austin, R. W. (1976) Air-water radiance calibration factor. *Tech. Memo. ML-76-004T*, 8pp., Scripps Institution of Oceanography.

Berk, A., Acharya, P. K., Bernstein, L. S., Anderson, G. P., Chetwynd Jr., J. H. and Hoke, M. L. (2000). Reformulation of the MODTRAN band model for higher spectral resolution. In S. S. Shen and M. R. Descour, Eds, Proceedings of SPIE Proc., Algorithms for Multispectral, Hyperspectral, and Ultraspectral Imagery VI, **4049**, pp. 190-198.

Berk, A., Bernstein, L. S., Anderson, G. P., Acharya, P. K., Robertson, D. C., Chetwynd, J. H. and Adler-Golden, S. M. (1998). "MODTRAN cloud and multiple scattering upgrades with application to AVIRIS." *Remote Sensing of Environment*, **65**(3): 367-375.

Brivio, P. A., Giardino, C. and Zilioli, E. (2001). "Validation of satellite data for quality assurance in lake monitoring applications." *Science of the Total Environment*, **268**(1-3): 3-18.

Carder, K. L., Chen, F. R., Cannizzaro, J. P., Campbell, J. W. and Mitchell, B. G. (2004). "Performance of the MODIS semi-analytical ocean color algorithm for chlorophyll-a."

Climate Change Processes in the Stratosphere, Earth-Atmosphere-Ocean Systems, and Oceanographic Processes from Satellite Data, **33**(7): 1152-1159.

Carmichael, W. W. (1997). "The cyanotoxins." *Advances in Botanical Research, Vol 27*, **27**: 211-256.

Dall'Olmo, G. and Gitelson, A. A. (2005). "Effect of bio-optical parameter variability on the remote estimation of chlorophyll-a concentration in turbid productive waters: experimental results." *Applied Optics*, **44**(3): 412-422.

Dall'Olmo, G. and Gitelson, A. A. (2006). "Effect of bio-optical parameter variability and uncertainties in reflectance measurements on the remote estimation of chlorophyll-a concentration in turbid productive waters: modeling results." *Applied Optics*, **45**(15): 3577-3592.

Dall'Olmo, G., Gitelson, A. A., Rundquist, D. C., Leavitt, B., Barrow, T. and Holz, J. C. (2005). "Assessing the potential of SeaWiFS and MODIS for estimating chlorophyll concentration in turbid productive waters using red and near-infrared bands." *Remote Sensing of Environment*, **96**(2): 176-187.

Darecki, M. and Stramski, D. (2004). "An evaluation of MODIS and SeaWiFS bio-optical algorithms in the Baltic Sea." *Remote Sensing of Environment*, **89**(3): 326-350.

Dekker, A. G. (1993). Detection of Optical Water Quality Parameters for Eutrophic Waters by High Resolution Remote Sensing. Ph.D. Thesis. Amsterdam, Vrije Universiteit**:** 222.

Doerffer, R. and Schiller, H. (2007). "The MERIS case 2 water algorithm." *International Journal of Remote Sensing*, **28**(3-4): 517-535.

Doerffer, R. and Schiller, H. (2008) MERIS regional coastal and lake case 2 water project atmospheric correction ATBD. *GKSS-KOF-MERIS-ATBD01*, (42pp), Institute for Coastal Research, GKSS Research Center, Geesthacht.

FLAASH Module User's Guide (2008). FLAASH Module Version 4.5, ITT Visual Information Solutions.

Gao, B. C., Montes, M. J., Ahmad, Z. and Davis, C. O. (2000). "Atmospheric correction algorithm for hyperspectral remote sensing of ocean color from space." *Applied Optics*, **39**(6): 887-896.

Gitelson, A. (1992). "The Peak near 700 Nm on Radiance Spectra of Algae and Water - Relationships of Its Magnitude and Position with Chlorophyll Concentration." *International Journal of Remote Sensing*, **13**(17): 3367-3373.

Gitelson, A., Gurlin, D., Moses, W. and Barrow, T. (2009). "A bio-optical algorithm for the remote estimation of the chlorophyll-a concentration in case 2 waters." *Environmental Research Letters*, **4**(045003): 5pp.

Gitelson, A. A., Dall'Olmo, G., Moses, W., Rundquist, D. C., Barrow, T., Fisher, T. R., Gurlin, D. and Holz, J. (2008). "A simple semi-analytical model for remote estimation of chlorophyll-a in turbid waters: Validation." *Remote Sensing of Environment*, **112**(9): 3582-3593.

Gitelson, A. A. and Kondratyev, K. Y. (1991). "On the Mechanism of Formation of Maximum in the Reflectance Spectra Near 700 nm and its Application for Remote Monitoring of Water Quality." *Transactions Doklady of the USSR Academy of Sciences: Earth Science Sections*, **306**: 1-4.

Gitelson, A. A., Schalles, J. F. and Hladik, C. M. (2007). "Remote chlorophyll-a retrieval in turbid, productive estuaries: Chesapeake Bay case study." *Remote Sensing of Environment*, **109**(4): 464-472.

Gitelson, A. A., Yacobi, Y. Z., Schalles, J. F., Rundquist, D. C., Han, L., Stark, R. and Etzion, D. (2000). "Remote Estimation of Phytoplankton Density in Productive Waters." *Archives for Hydrobiology, Special Issues: Advances in Limnology*, **55**: 121-136.

Gons, H. J. (1999). "Optical teledetection of chlorophyll a in turbid inland waters." *Environmental Science & Technology*, **33**(7): 1127-1132.

Gons, H. J., Auer, M. T. and Effler, S. W. (2008). "MERIS satellite chlorophyll mapping of oligotrophic and eutrophic waters in the Laurentian Great Lakes." *Remote Sensing of Environment*, **112**(11): 4098-4106.

Gons, H. J., Rijkeboer, M. and Ruddick, K. G. (2002). "A chlorophyll-retrieval algorithm for satellite imagery (Medium Resolution Imaging Spectrometer) of inland and coastal waters." *Journal of Plankton Research*, **24**(9): 947-951.

Gons, H. J., Rijkeboer, M. and Ruddick, K. G. (2005). "Effect of a waveband shift on chlorophyll retrieval from MERIS imagery of inland and coastal waters." *Journal of Plankton Research*, **27**(1): 125-127.

Gordon, H. R., Brown, O. B., Evans, R. H., Brown, J. W., Smith, R. C., Baker, K. S. and Clark, D. K. (1988). "A Semianalytic Radiance Model of Ocean Color." *J. Geophys. Res.*, **93**: 10909-10924.

Gordon, H. R., Brown, O. B. and Jacobs, M. M. (1975). ""Computed Relationships Between the Inherent and Apparent Optical Properties of a Flat Homogeneous Ocean." *Applied Optics*, **14**: 417-427.

Gordon, H. R., Clark, D. K., Brown, J. W., Brown, O. B., Evans, R. H. and Broenkow, W. W. (1983). "Phytoplankton pigment concentrations in the Middle Atlantic bight: comparison between ship determinations and Coastal Zone Scanner estimates." *Applied Optics*, **22**(1): 20-26.

Gordon, H. R. and Morel, A. Y. (1983). Remote assessment of ocean color for interpretation of satellite visible imagery : a review. New York, Springer-Verlag.

Gordon, H. R. and Wang, M. H. (1994). "Retrieval of Water-Leaving Radiance and Aerosol Optical-Thickness over the Oceans with Seawifs - a Preliminary Algorithm." *Applied Optics*, **33**(3): 443-452.

Gould, R. W. and Arnone, R. A. (1994). Extending Coastal Zone Color Scanner estimates of the diffuse attenuation coefficient into Case II waters. In Ocean Optics XII, S. J. Jules (ed.), Ed. Proceedings of the SPIE, **2258**, pp. 342-356.

Gower, J., King, S., Borstad, G. and Brown, L. (2005). "Detection of intense plankton blooms using the 709 nm band of the MERIS imaging spectrometer." *International Journal of Remote Sensing*, **26**(9): 2005-2012.

Gower, J. F. R., Doerffer, R. and Borstad, G. A. (1999). "Interpretation of the 685 nm peak in water-leaving radiance spectra in terms of fluorescence, absorption and scattering, and its observation by MERIS." *International Journal of Remote Sensing*, **20**(9): 1771-1786.

Han, L., Rundquist, D. C., Liu, L. L., Fraser, R. N. and Schalles, J. F. (1994). "The Spectral Responses of Algal Chlorophyll in Water with Varying Levels of Suspended Sediment." *International Journal of Remote Sensing*, **15**(18): 3707-3718.

Han, L. H. and Rundquist, D. C. (1994). "The Response of Both Surface Reflectance and the Underwater Light-Field to Various Levels of Suspended Sediments - Preliminary-Results." *Photogrammetric Engineering and Remote Sensing*, **60**(12): 1463-1471.

Han, L. H. and Rundquist, D. C. (1996). "Spectral characterization of suspended sediments generated from two texture classes of clay soil." *International Journal of Remote Sensing*, **17**(3): 643-649.

Han, L. H. and Rundquist, D. C. (1997). "Comparison of NIR/RED ratio and first derivative of reflectance in estimating algal-chlorophyll concentration: A case study in a turbid reservoir." *Remote Sensing of Environment*, **62**(3): 253-261.

Honeywill, C., Paterson, D. M. and Hegerthey, S. E. (2002). "Determination of Microphytobenthic Biomass Using Pulse-Amplitude Modulated Minimum Fluorescence." *European Journal of Phycology*, **37**(4): 485-492.

Hu, C. M., Carder, K. L. and Muller-Karger, F. E. (2000). "Atmospheric correction of SeaWiFS imagery over turbid coastal waters: A practical method." *Remote Sensing of Environment*, **74**(2): 195-206.

Kruse, F. A., Kiereinyoung, K. S. and Boardman, J. W. (1990). "Mineral Mapping at Cuprite, Nevada with a 63-Channel Imaging Spectrometer." *Photogrammetric Engineering and Remote Sensing*, **56**(1): 83-92.

Lee, Z. P., Carder, K. L., Hawes, S. K., Steward, R. G., Peacock, T. G. and Davis, C. O. (1994). "Model for the Interpretation of Hyperspectral Remote-Sensing Reflectance." *Applied Optics*, **33**(24): 5721-5732.

Matthew, M. W., Adler-Golden, S. M., Berk, A., Felde, G., Anderson, G. P., Gorodetzky, D., Paswaters, S. and Shippert, M. (2002). Atmospheric Correction of Spectral Imagery: Evaluation of the FLAASH Algorithm with AVIRIS Data. In Proceedings of 31st Applied Imagery Pattern Recognition Workshop, Washington, D.C., IEEE Computer Society, pp. 157-163.

Montes, M. J., Gao, B. C. and Davis, C. O. (2001). A new algorithm for atmospheric correction of hyperspectral remote sensing data. In Geo-Spatial Image and Data Exploitation II, W. E. Roper, Ed. Proceedings of the SPIE, **4383**, pp. 23-30.

Moore, G. F., Aiken, J. and Lavender, S. J. (1999). "The atmospheric correction of water colour and the quantitative retrieval of suspended particulate matter in Case II waters: application to MERIS." *International Journal of Remote Sensing*, **20**(9): 1713-1733.

Moore, G. K. (1980). "Satellite remote sensing of water turbidity." *Hydrological Sciences Bulletin*, **25**: 407-421.

Morel, A. and Prieur, L. (1977). "Analysis of Variations in Ocean Color." *Limnology and Oceanography*, **22**(4): 709-722.

Moses, W. J., Gitelson, A. A., Berdnikov, S. and Povazhnyy, V. (2009a). "Estimation of chlorophyll-a concentration in case II waters using MODIS and MERIS data—successes and challenges." *Environmental Research Letters*, **4**(045005): 8pp.

Moses, W., Gitelson, A., Berdnikov, S. and Povazhnyy, V. (2009b). "Satellite estimation of chlorophyll-a concentration using the red and NIR bands of MERIS - the Azov Sea case study." *IEEE Geoscience and Remote Sensing Letters*, **4**(6): 845-849.

Mueller, J. L. (1984). Effects of water reflectance at 670 nm on Coastal Zone Color Scanner (CZCS) aerosol radiance estimates off the coast of central California. In Ocean Optics VII, Proceedings of the SPIE, Bellingham, WA, **489**, pp. 179-186.

Mueller, J. L. and Austin, R. W. (1995) Ocean Optics Protocols for SeaWiFS Validation, Revision 1. *SeaWiFS Technical Report Series, Vol. 25, NASA Tech. Memo. 104566*, NASA Goddard Space Flight Center, MD.

O'Reilly, J. E., Maritorena, S., Mitchell, B. G., Siegel, D. A., Carder, K. L., Garver, S. A., Kahru, M. and McClain, C. (1998). "Ocean color chlorophyll algorithms for SeaWiFS." *Journal of Geophysical Research-Oceans*, **103**(C11): 24937-24953.

O'Reilly, J. E., et al. (2000) SeaWiFS Postlaunch Calibration and Validation Analyses, Part 3. *NASA Tech. Memo. 2000-206892, Vol. 11*, 49 pp., NASA Goddard Space Flight Center, MD.

Ohde, T. and Siegel, H. (2003). "Derivation of immersion factors for the hyperspectral TriOS radiance sensor." *Journal of Optics a-Pure and Applied Optics*, **5**(3): L12-L14.

Palmer, K. F. and Williams, D. J. (1974). "Optical properties of water in the near infrared." *Journal of the Optical Society of America*, **64**(8): 1107-1110.

Revenga, C. and Kura, Y. (2003). *Status and trends of biodiversity of inland water ecosystems*. Montreal, Secretariat of the Convention on Biological Diversity.

Ruddick, K. G., Gons, H. J., Rijkeboer, M. and Tilstone, G. (2001). "Optical Remote Sensing of Chlorophyll-a in Case 2 Waters By Use of an Adaptive Two-band Algorithm With Optimal Error Properties." *Applied Optics*, **40**(21): 3575-3585.

Ruddick, K. G., Ovidio, F. and Rijkeboer, M. (2000). "Atmospheric correction of SeaWiFS imagery for turbid coastal and inland waters." *Applied Optics*, **39**(6): 897-912.

Schalles, J. F. (2006). Optical Remote Sensing techniques to estimate Phytoplankton Chlorophyll a concentrations in coastal waters with varying suspended matter and CDOM concentrations. *Remote Sensing of Aquatic Coastal Ecosystem Processes: Science and Management Applications*. L. L. Richardson and E. F. LeDrew, Springer**:** 27-79.

Schalles, J. F., Gitelson, A. A., Yacobi, Y. Z. and Kroenke, A. E. (1998). "Estimation of chlorophyll a from time series measurements of high spectral resolution reflectance in an eutrophic lake." *Journal of Phycology*, **34**(2): 383-390.

Siegel, D. A., Wang, M. H., Maritorena, S. and Robinson, W. (2000). "Atmospheric correction of satellite ocean color imagery: the black pixel assumption." *Applied Optics*, **39**(21): 3582-3591.

Smith, R. C. (1981). Ship and satellite biooptical research in the California bight. Oceanography from Space. J. F. R. Gower, Plenum Press**:** 281-194.

Stumpf, R. P., Arnone, R. A., Gould, R. W., Martinolich, P. M. and Ransibrahmanakul, V. (2003) A Partially Coupled Ocean-Atmosphere Model for Retrieval of Water-Leaving Radiance from SeaWiFS in Coastal Waters. *NASA Tech. Memo. 2003-206892, Vol. 22,* 51-59, NASA Goddard Space Flight Center, MD.

Stumpf, R. P. and Pennock, J. R. (1989). "Calibration of a general optical equation for remote sensing of suspended sediment in a moderately turbid estuary." *Journel of Geophysical Research*, **94**: 14363-14371.

Stumpf, R. P. and Tyler, M. A. (1988). "Satellite detection of bloom and pigment distributions in estuaries." *Remote Sensing of Environment,* **24**(385-404).

Vasilkov, A. and Kopelevich, O. (1982). "Reasons for the Appearance of the Maximum near 700 nm in the Radiance Spectrum Emitted by the Ocean Layer." *Oceanology,* **22**(6): 697-701.

Wang, M. H. and Shi, W. (2005). "Estimation of ocean contribution at the MODIS near-infrared wavelengths along the east coast of the US: Two case studies." *Geophysical Research Letters*, **32**(13): L13606.

Welschmeyer, N. A. (1994). "Fluorometric analysis of chlorophyll a in the presence of chlorophyll b and pheopigments." *Limnology and Oceanography,* **39**(8): 1985-1992.

Zibordi, G. (2006). "Immersion factor of in-water radiance sensors: Assessment for a class of radiometers." *Journal of Atmospheric and Oceanic Technology*, **23**(2): 302-313.